

MICRON-SCALE THERMISTORS FOR RAPID TRANSIENTS IN INTERFACIAL TEMPERATURE

by
Michael Liu

B.S., Mechanical Engineering (1996), University of California at Berkeley
B.S., Nuclear Engineering (1996), University of California at Berkeley

Submitted to the Department of Mechanical Engineering in Partial Fulfillment
of the Requirements for the Degree of Master of Science in Mechanical Engineering

at the

Massachusetts Institute of Technology

September 1998

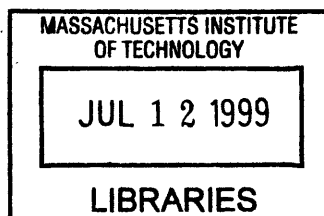
©1998 Massachusetts Institute of Technology; All Rights Reserved

Signature of Author
Department of Mechanical Engineering
20 August 1998

Certified by
Ain A. Sonin
Professor of Mechanical Engineering
Thesis Supervisor

Certified by
Taiqing Qiu
Assistant Professor of Mechanical Engineering
Thesis Supervisor

Accepted by
Ain A. Sonin
Chairman, Department Committee on Graduate Students



ENG

MICRON-SCALE THERMISTORS FOR RAPID TRANSIENTS IN INTERFACIAL TEMPERATURE

by

Michael Liu

Submitted to the Department of Mechanical Engineering
On 20 August 1998 in Partial Fulfillment of the
Requirements of the Degree of Master of Science in
Mechanical Engineering

Abstract

The shape of freezing droplets is controlled by the motion of the molten interface, or contact line, between the liquid droplet and the solid target. The solution for the heat transfer between the liquid and solid has an analytical singularity at the contact line. We therefore wish to closely examine the temperature history of the contact line as it spreads across a target. In order to achieve high spatial and temporal resolution in our temperature sensors, we use microsensors (specifically, thin-film thermistors), which are built using standard integrated-circuit techniques. A complete data acquisition system was built around the sensors, including various signal-conditioning hardware and software. The integrated-circuit processes to build our microsensors limit our choices of target materials. Previous analyses of droplet spreading in our group have focussed on the spreading of molten materials on targets of the same kind or of similar thermal characteristics. In contrast, the microsensor targets will have thermal conductivities and diffusivities at least an order of magnitude greater than that of the molten materials in use. Thus, we also characterized the spreading of a molten droplet on a substrate of a different type. Finally, we characterized the sensors' resistance response to temperature changes, during both spreading and calibration experiments.

Thesis Supervisor: Dr. Ain A. Sonin

Title: Professor of Mechanical Engineering

Thesis Supervisor: Dr. Taiqing Qiu

Title: Assistant Professor of Mechanical Engineering

TABLE OF CONTENTS

Abstract.....	2
Table of Contents.....	3
List of Figures.....	5
Acknowledgements.....	8
Chapter 1 Introduction and Motivation	9
Motivation	9
Chapter 2 Sensor Chips	12
Design.....	12
Construction	17
Packaging	20
Conclusions	25
Chapter 3 Support Hardware	26
Package Holder.....	27
Circuitry Boxes.....	29
DAQ Card and Miscellaneous Items	34
Conclusions	34
Chapter 4 Data Acquisition Software	35
Single-Point Calibration	36
Continuous Acquisition	40
Data Reduction and Graphing	43
Conclusions	47
Chapter 5 Smooth Silicon Deposition	48
Nonequilibrium Post-Solidification Angle of Wax on Silicon	49
Apparent Dynamic Contact Angle.....	54
Conclusions	55
Chapter 6 Grooved Silicon Deposition.....	56
Effect on Spreading	57
Conclusions	60
Chapter 7 One-Dimensional Heat Transfer Model.....	61
Analysis	62
Limitations.....	70
Chapter 8 Sensor Calibration.....	72
Resistance-Temperature Characteristic	72

Temperature Measurement Issues	76
Conclusions	79
Chapter 9 Sensor Response in Drop Deposition.....	80
Noise Issues	80
Results	83
Conclusions	86
Chapter 10 Conclusions and Further Work	88
Further Work	89
Nomenclature and Abbreviations	90
References	93
Appendix A: The MTL and its Machines	95
Appendix B: Material Properties	98
Appendix C: Data for Selected Figures	99

LIST OF FIGURES

Figure 1.1 Overview of sensor data acquisition system.	10
Figure 2.1 Early sensor chip design, with forty-four Cu-Ni thermocouples and two Cu RTDs.	13
Figure 2.2 Ground and valence band populations of (a) conductors, (b) nonconductors, and (c) semiconductors; depicted (a; b; c, i) before and (a; b; c, ii) after applied energy.	14
Figure 2.3 (a) Top and (b) cross-section view of a single fine linear array sensor.	16
Figure 2.4 Photographs of (a) a plain silicon wafer, already sawed into individual chips and (b) a single chip.	17
Figure 2.5 Steps in the photolithography process: (a) oxide growth, (b) photoresist coat, (c) photoresist development, (d) mask removal, (e) photoresist etch, (f) oxide etch, (g) developed photoresist etch, (h) ion implantation, and (i) finished doped part. Adapted from Schwarz and Oldham (1993).	18
Figure 2.6 Construction of an individual (fine) sensor, top view: (a) initial blank wafer, (b) deposition of n-doped silicon, (c) first mask for etching, (d) second mask for more doping, (e) third mask for protective layer, and (f) fourth mask for circuit traces. Adapted from Qiu (1996).	20
Figure 2.7 Schematic of a forty-pin DIP; (a) with chip and wirebonds, (b) showing pin and pad assignments.	21
Figure 2.8 Coarse cross (CC) array chip-pad assignments.	22
Figure 2.9 Coarse linear (CL) array chip-pad assignments.	23
Figure 2.10 Fine linear (FL) array chip-pad assignments.	24
Figure 2.11 Proposed alternative chip circuit trace layout.	25
Figure 3.1 Sensor-Circuit-Card connections for the first two sensors in the (a) coarse arrays and (b) fine linear array.	27
Figure 3.2 Package holder, showing the package socket and the side-mounted sensor array ports.	28
Figure 3.3 Fine Linear circuit box (facing top panel).	30
Figure 3.4 Bridge circuit for coarse sensor arrays (CC, CL).	31
Figure 3.5 Divider circuit for fine linear (FL) sensor array.	32
Figure 4.1 Software used to process voltage information from sensor chip.	35
Figure 4.2 “My Calibration AI” (MCAI) reads, converts, and averages a series of sensor resistance measurements.	37
Figure 4.3 Typical “My Calibration AI” output.	38
Figure 4.4 “Grab Save Analyze (cal)” (GSA) sorts and analyzes MCAI output files.	39
Figure 4.5 Typical “Grab Save Analyze (cal)” (GSA) output file.	40

Figure 4.6 “My Cts Acq to File” (MCAF) scans specified input channels for a set time and saves directly to disk.	41
Figure 4.7 The “automan” subroutine selects the channels to be used during data acquisition.....	42
Figure 4.8 “My Newer Disp Acq’d File” (MDAF) converts binary voltage data into ASCII-text resistance data.	43
Figure 4.9 “Array Subsetter” (ASub) scans a single column of a MDAF output file for certain values, cuts out a subset of the MDAF file, and appends time information to it.	44
Figure 4.10 Typical “Array Subsetter” (ASub) output file.....	45
Figure 4.11 “Array Slicer” (ASli) manually cuts out a subset of a MDAF output file.....	46
Figure 4.12 “Sliced Array Plotter” charts temperature as a function of time, from ASli or ASub output files.	47
Figure 5.1 Profile views of solidified droplets, where (a) $\theta < 90^\circ$ and (b) $\theta > 90^\circ$	49
Figure 5.2 Post-solidification contact angle (in degrees) versus (a) Stefan number [$S = c_p(T_f - T_i)/L$] and versus (b) number of droplets. Microcrystalline wax (Reed 6882) on monocrystalline silicon.	50
Figure 5.3 Constant post-solidification contact angle (in degrees) versus Stefan number. Microcrystalline wax (Reed 6882) on monocrystalline silicon.	51
Figure 5.4 Contact angle (in degrees) versus total deposition time (in seconds) for a target temperature of 78°C. Microcrystalline wax (Reed 6882) on silicon.....	52
Figure 5.5 Contact angle (in degrees) versus total deposition time (in seconds) for a target temperature of 85°C. Microcrystalline wax (Reed 6882) on silicon.....	53
Figure 5.6 Contact line radius (in meters) versus time (in seconds), experiment and theory. Microcrystalline wax (Reed 6882) on silicon; $f=2.5\text{kHz}$ and $T_f=79^\circ\text{C}$	54
Figure 6.1 Schematics of the (a) top part and (b) cross-section close-up of the grooved silicon chips.	57
Figure 6.2 Typical microcrystalline wax macrodrops deposited on patterned silicon. Rectangle shown is 1/3 mm long.....	58
Figure 6.3 Aspect ratio (length/width) of macrodrops versus (a) target temperature (in °C) and (b) total deposition time, N/f (in seconds). Microcrystalline wax (Reed 6882) on silicon.	59
Figure 6.4 Close-up view of a macrodrop on a grooved chip, showing a component spreading ahead of the contact line. 16 drops at 5 kHz, target temperature of 85°C; microcrystalline wax (Reed 6882) on silicon.	60
Figure 7.1 Alternative models of variable specific heat with melting range $\Delta T = 50^\circ\text{C}$	62
Figure 7.2 One-dimensional solidification of a material with a phase transition region on a target of a different material.	63
Figure 7.3 Motion of solidification front at temperature T_f (pure substance).....	64

Figure 8.1 Sensor chip resistance versus temperature for chip number QU-11, coarse linear (CL) array, with NTC thermistor behavior illustrated.....	74
Figure 8.2 Temperature response of CL2 sensor on chip QU-11 versus exponential fits (“NTC fit” from eqn. 8-2, “NTCexpT fit” from eqn. 8-3).....	75
Figure 8.3 Normalized resistance versus temperature difference for CL array on QU-11 chip.	76
Figure 8.4 Resistance versus temperature for CL2 sensor on QU-11 chip, measured with package heaters only and oven heating.....	77
Figure 8.5 Actual (chip surface) temperature (in °C) versus indicated (package surface) temperature (in °C). CL2 sensor in QU-11 package.	78
Figure 9.1 Indicated temperature (in °C, deviation from 30°C) versus time (in seconds) with unshielded heaters and cabling. CC array in QU-3 package; 300Hz sampling rate.....	80
Figure 9.2 Indicated temperature (in °C, deviation from 30°C) versus time (in seconds) with shielded heaters and cabling. CC array in QU-3 package; 300Hz sampling rate.....	81
Figure 9.3 Indicated temperature (in °C, deviation from 30°C) versus time (in seconds), during a deposition experiment with the adapted thermal ink-jet print head. Microcrystalline wax (Reed 6882) on silicon dioxide; FL2 array in QU-3 package; 20kHz sampling rate.....	82
Figure 9.4 Indicated temperature (in °C, deviation from 30°C) versus time (in seconds), during a deposition experiment, showing spurious signal from back heaters. Octacosane on silicon dioxide; CL6 sensor in QU-7 package; 333kHz sampling rate.....	83
Figure 9.5 Temperature (in °C) versus time (in seconds) for three adjacent sensors. Octacosane on silicon dioxide; CL3, CL6, and CL8 sensors in QU-11 package; 111kHz sampling rate.	84
Figure 9.6 Temperature (in °C) versus time (in seconds) for one sensor, showing instantaneous rise as contact line passes. Octacosane on silicon dioxide; CL3 sensor in QU-11 package; 111kHz sampling rate.....	85

ACKNOWLEDGEMENTS

I owe many thanks to my thesis supervisors, Professors Ain Sonin and Taiqing Qiu. Their help and guidance through my degree program were invaluable; their teachings much more than paint-by-numbers. I thank them for challenging me on a daily basis and helping me to grow beyond my complacency.

I thank my parents and brother, whose ballooning telephone bills, frequent support, and love proved to me that moving across the country doesn't have to mean falling out of touch.

My colleagues in the microdrop deposition group have been universally encouraging and excellent sources of knowledge. Gregg, Javier, Marcelo, and Pirouz all make me hope that I've contributed as much to their work as they have to mine. Countless falafels later and we're still alive, eh, Javi? Then again, there's always schtuff to discuss ...

I've been against the business end of too many wee hours to miss thanking the red-eye crew: Carlos, Cuiling, Freddie, Jeff, Jon, and countless other FML souls kept me sane through the nights (and days blurred unhappily). The people and faces I will keep with me.

Hey, Bean, let's walk again sometime soon, all right?

And Allegra:

my joy you bring
my dreams and every
morning glows your eyes
hold strength back home

Chapter 1 INTRODUCTION AND MOTIVATION

Gao and Sonin (1994) have constructed a novel drop-on-demand microfabrication system. By depositing molten droplets fifty microns in diameter on a cooled target, part prototypes may be made quickly relative to current methods, such as stereolithography or machining. The heart of the device is a modified ink-jet printer head; molten wax droplets are ejected in a regular, repeatable manner towards a cooled substrate, where they spread and freeze to form detailed features.

This system is controlled by a pulse generator, which provides the impulse to a piezoelectric piston in the ink-jet head. This piston pushes wax through a small orifice and retracts, ejecting a droplet. In order to study the spreading of the droplets, we deposit larger drops, which we call macrodrops, using the modified ink-jet head. To deposit a macrodrop, a given number of droplets are fed at a known rate into a growing puddle of molten wax. The feature size is then large enough to discern the motion of the molten contact line, the point of arrest, and the apparent contact angle during deposition. Alternatively, we may use a pendant drop apparatus, constructed by Duthaler (1998). A small amount of solid material is melted in a temperature-controlled crucible, forming a liquid drop at the end of a precisely machined nozzle. This drop grows as material is added until, under the influence of gravity, it breaks free from the nozzle and impacts the substrate.

Several factors affect the final shape of a spreading drop: the degree of target subcooling (the amount that the target is cooled below the molten material's melting temperature), the thermal conductivities of the target and melt materials, and the surface energy at the melt-substrate interface. When a drop is deposited on a subcooled target, this drop will hit, spread under the influence of inertia and surface tension, and apparently freeze in a spherical cap shape. Thus, the point at which the contact line arrests is governed by both fluid mechanics (rate of spreading) and heat transfer (rate of solidification). When growing macrodrops through continuous feeding, the frequency of deposition and the number of droplets deposited also affect the final shape. Depending on the frequency of deposition, successive droplets may arrive after the previously deposited droplets have solidified, and thus create pillars, assuming that the deposition head and target do not move relative to each other.

MOTIVATION

We wish to examine the heat transfer that occurs at the contact line between the melt and the solid. Schiaffino (1996) has demonstrated the existence of an analytical singularity in the heat transfer equations at the contact line. He modeled the heat flux with standard continuum heat-flow equations in all regions except for one close to the contact line. Within this region, defined by a dimension called the cut-off length, the heat flux is assumed constant and continuous from the continuum region. The cut-off length was on the order of 0.1 to 1 micron for microcrystalline wax (Reed 6882).

Qiu (1996) has designed micron-scale temperature sensors using the same methods that integrated circuits on silicon wafers. Because these sensors are small, they offer extremely fine temporal and spatial resolution. Compared to standard thermocouples, which use a sphere approximately one millimeter in diameter to sense temperature, these new sensors are nearly a thousand times smaller, with corresponding gains in temporal and spatial resolution. Although they are still larger than the cut-off length proposed by Schiaffino, they offer a detailed look at the temperature history of the contact line.

Because the design is implemented using standard silicon microfabrication techniques, we have a limited choice of substrates. Previous analyses have assumed the thermal properties of the melt and target to be well-matched (if they were not the same material). We used silicon and silicon dioxide-based sensors, both of which have much higher thermal conductivities than the melts we used, microcrystalline wax and octacosane. Thus, we expect a thermal precursor in the substrate to lead the temperature response very near the contact line.

A complete system, shown in Figure 1.1, was built to accommodate data acquisition from our sensors. The chips were first packaged into standard integrated circuit packages. Several pieces of hardware were then built to heat the chip and carry electrical signals. A data acquisition card was obtained, installed in a standard Windows NT personal computer, and software was written to acquire and convert data.

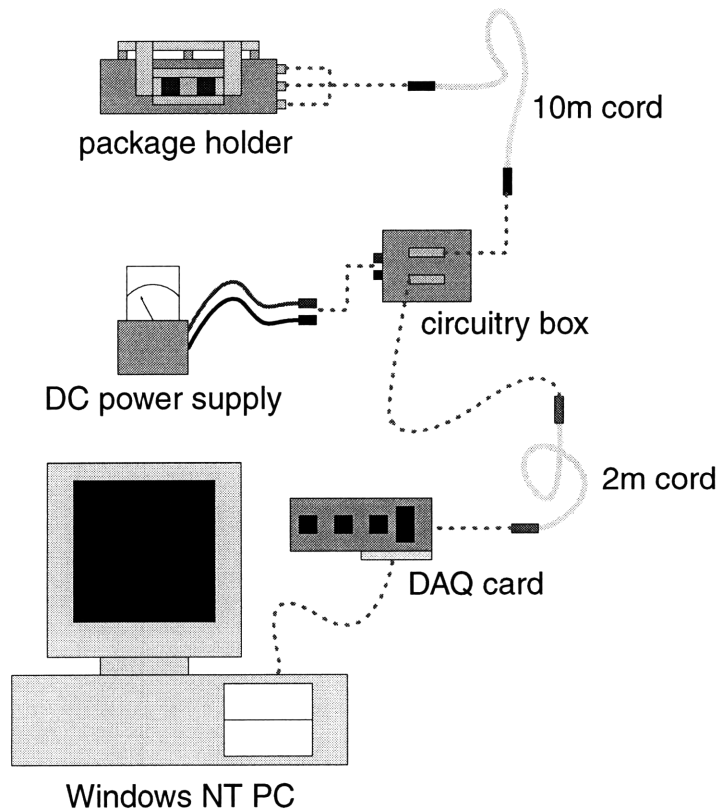


Figure 1.1 Overview of sensor data acquisition system.

In order to predict the performance of our sensors, we conducted two preliminary tests. The first one determined how a target with a higher thermal conductivity would affect the spreading of a melt. The other one gauged the effect of the physical features on the motion of the contact line. We also modeled the solidification process, in one dimension, for a melt on a target with different thermal properties.

Chapter 2 SENSOR CHIPS

Micron-scale transducers are not new. In the past fifteen years, various designs for pressure, shear, chemical, and thermal sensors have been proposed and realized. Korites (1986) provides a general overview of microsensor design and construction; microsensor fabrication uses techniques developed for integrated circuit (IC) manufacture. Microsensors offer many advantages when compared with conventional sensors, such as increased sensitivity, precision manufacturing, and ruggedness (*ibid.*). However, they have not proven to be a commercial success – the typical microsensor project is a small-volume production destined for the research laboratory. Wolffenbuttel, et. al. (1996) point out that while microsensors and ICs use the same manufacturing processes, the yield criteria (i.e. what constitutes an acceptable part) are different. Because microsensors are characterized by a specific numeric value, rather than a specific function, each part requires more testing and characterization than ICs. For example, in an IC, a useable diode allows current in only one direction. On the other hand, if that diode were a temperature sensor, we would want to know the specific thermal dependence of current passed.

Thermal microsensors are governed by the same physics as conventional thermal sensors; thermocouple and thermistor designs appear to be the most popular types (e.g. Baltes (1993) and van Herwaarden (1986)). These designs have many applications, usually as gas conductivity and radiation sensors; however, Kiewra and Wayner (1989) have applied thermal microsensors to moving contact lines. Their study outlined the circuitry and offered recommendations to future thermistor users.

DESIGN

Prof. T. Q. Qiu designed the sensors to detect temperature quickly and accurately. Because the heat flux at the melt-solid interface is unsteady and localized, small sensors are best able to resolve the temperature history of a spreading macrodrop. Their small size ensures greater spatial precision than conventional (i.e. off-the-shelf) thermocouples and better temporal resolution because of the small thermal mass. With these goals in mind, he drew up a novel design for temperature sensors on a silicon chip. They would be constructed using conventional microfabrication technology, which is used today to produce integrated circuits and microprocessors.

The initial design called for micron-scale thermocouples. Two dissimilar would make a micron-scale contact, forming a junction whose voltage potential would vary with temperature, according to the Seebeck effect. This early design is illustrated in Figure 2.1; it uses copper and nickel at its junctions, and two resistance temperature detectors (RTDs) to give a reference temperature reading. However, each individual thermocouple actually contains two nickel-copper junctions: one where intended (in the linear array) and another where the circuit trace joins the pad. In fact, standard packaging procedure calls for either gold or aluminum connectors between the chip and package, as well as gold or aluminum pins on the

package itself, leading to another set of dissimilar-metal junctions. All of these junctions will exhibit the Seebeck effect, adding to the voltage generated at the junction of interest.

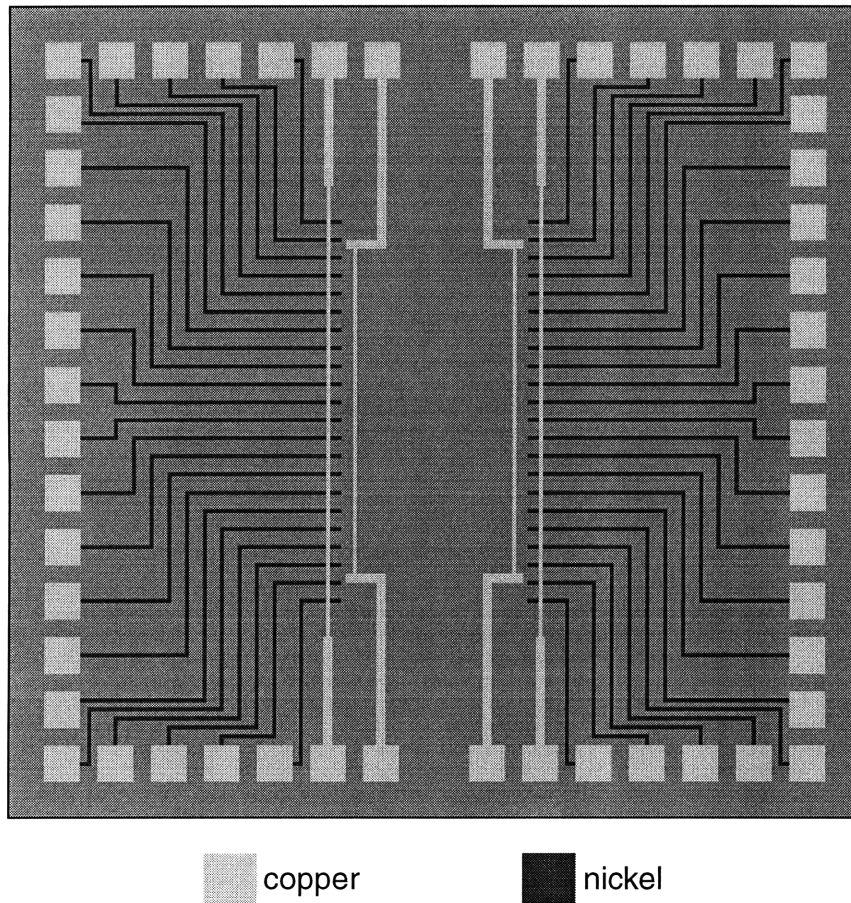


Figure 2.1 Early sensor chip design, with forty-four Cu-Ni thermocouples and two Cu RTDs.

In order to avoid this plague of dissimilar metals, the sensors were changed to thermistors, as detailed in Qiu (1996). Semiconductor-based thermistors, whose electrical resistance changes with temperature, have been present for many years. In general, the resistance of a semiconductor varies with temperature due to several competing factors, including lattice vibrations and charge carrier (electron) density. Lattice vibrations (phonons) impede the motion of electrons through the semiconductor. Thus, increasing the temperature increase resistance by increasing the number and amplitude of phonons.

However, this effect competes with decreasing electron density with temperature. Solid materials may be classified according to their electrical conductivity into conductors, nonconductors, and semiconductors; this in turn depends on the population of the ground and valence electron bands, which is illustrated in Figure 2.2. Conductors generally have one large, sparsely populated band, which allows electrons to move freely with relatively little driving energy. Nonconductors have completely filled ground bands and empty valence bands. In addition, the energy gap between the ground and valence bands is quite

large, which prevents electron motion without a significant driving potential. Semiconductors are similar to nonconductors in that the ground band is filled and the valence band is empty. However, the energy gap between the two bands is relatively small, so a modest increase in energy will excite some electrons into the empty valence band. This provides a relatively easy path for electrons, lowering the semiconductor's resistance. Adding impurity ions to the lattice in a process known as doping enhances this effect. Because these impurities have a different charge than the semiconductor ions, either vacancies will appear in the ground band or electrons will sparsely populate the valence band. Thus, the resistance of a semiconductor may also decrease with increasing temperature in semiconductors, but the effects are subject to constraint by the lattice vibrations.

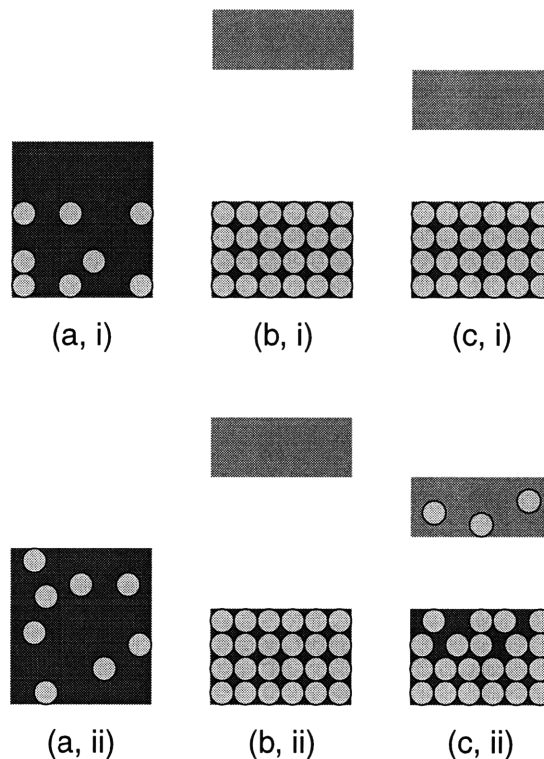
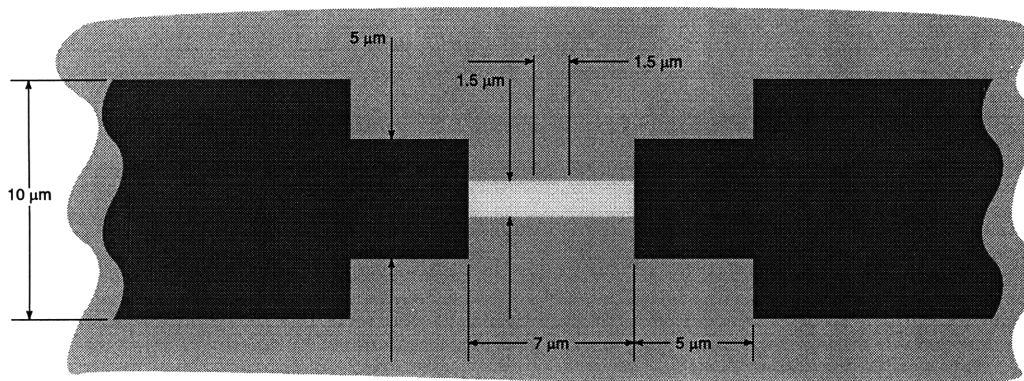


Figure 2.2 Ground and valence band populations of (a) conductors, (b) nonconductors, and (c) semiconductors; depicted (a; b; c, i) before and (a; b; c, ii) after applied energy.

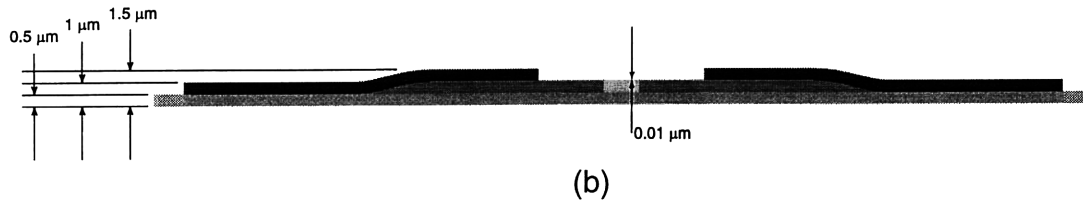
Doping a semiconductor changes its resistance and charge; the magnitude depends on the species of implanted ions. Plain silicon has a valence of +4, which means that there are four electrons in its outer electron shell. The implanted ions have different valences: boron, with a valence of +3, and phosphorous, with a valence of +5. Implanting boron ions is also known as positive-type doping. Since each boron atom has one fewer electron than a silicon atom, the net charge becomes more positive. More importantly, electron vacancies appear in the ground band. Similarly, since phosphorous atoms each contain one more electron than a silicon atom does, phosphorous doping is known as negative-type doping; the extra electrons go into the valence band. Boron and phosphorous doping result in p-doped and n-doped silicon,

respectively. Both p-doped and n-doped silicon are more electrically conductive than plain silicon, because the charge carriers can move more easily. Two adjacent n-doped and p-doped regions, also known as a bipolar junction, form a diode. It passes or stops current depending on the polarity of the applied voltage (i.e. if the voltage at the n-doped end is higher, then this junction will conduct freely). Similarly, the bipolar junction transistor consists of three adjoining regions, either p-n-p-doped or n-p-n-doped.

The sensors are made of lightly doped polycrystalline silicon (poly-Si). As outlined above, their resistance changes predictably with temperature. The structure of a single sensor is illustrated in Figure 2.3. Note that the actual sensing element, the lightly p-doped poly-Si region in the center, is only 1.5 by 1.5 by 0.5 μm . This gives each sensor a thermal mass (defined as the product of mass and specific heat) of $2.8\text{e-}18 \text{ J/K}$, so they should be extraordinarily sensitive to rapid changes in temperature. Unfortunately, plain (monocrystalline) silicon has an extremely high thermal conductivity – approximately 148 W/m-K – compared to that of microcrystalline wax, which is approximately 0.07 W/m-K . Therefore, the thermal precursor in the substrate will significantly lead the contact line and may also affect the spreading of a macrodrop. Thus, the sensors were built on two different wafer materials, plain silicon and amorphous silicon dioxide (i.e. fused silica, which has a much lower thermal conductivity of 1.38 W/m-K). A $0.1 \mu\text{m}$ -thick layer of silicon dioxide was applied over the top of the sensing element to protect it from mechanical stresses.



(a)



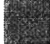




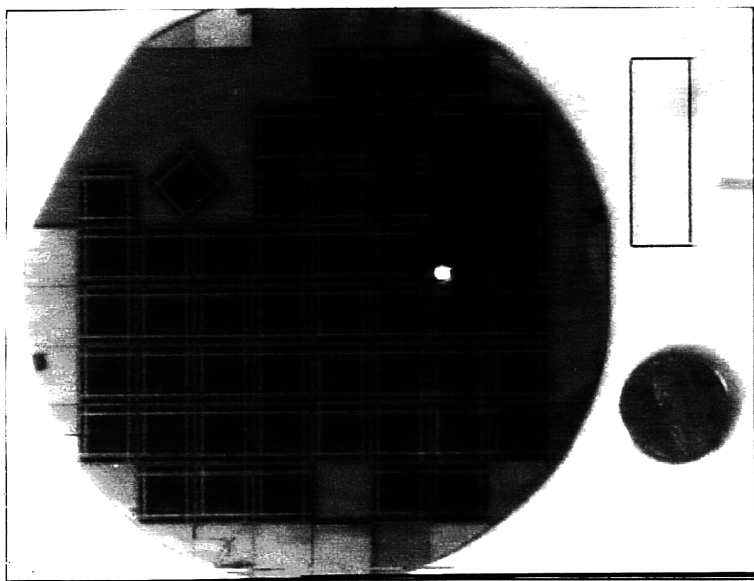
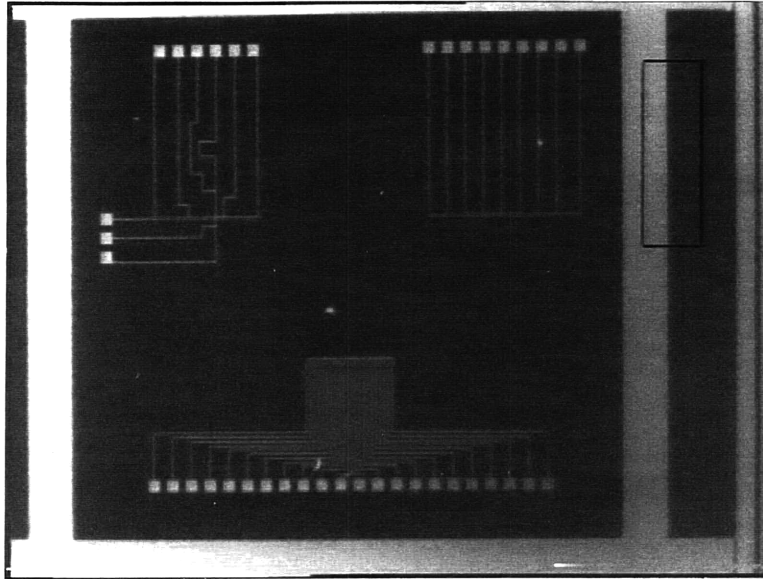
-  silicon dioxide (substrate)
-  lightly p-doped polycrystalline silicon (sensing element)
-  heavily p-doped polycrystalline silicon (sensor lead)
-  silicon dioxide (protective layer)
-  aluminum (circuit trace)

Figure 2.3 (a) Top and (b) cross-section view of a single fine linear array sensor.

A single wafer, depicted in Figure 2.4 (a), holds sixty chips; an single chip is shown in Figure 2.4 (b). Each chip contains thirty-six sensors, which are grouped into three different arrays: the coarse cross (CC) array (containing eight sensors, in the upper left corner), the coarse linear (CL) array (which also has eight sensors, in the upper right corner), and the fine linear (FL) array (which holds the remaining twenty sensors, at the bottom). The CC array sensors are spaced $400\ \mu\text{m}$ apart, while the CL array sensors are spaced $200\ \mu\text{m}$ apart; the sensing elements both arrays are slightly larger than shown in Figure 2.3 at $2.5\ \mu\text{m}$ square. The FL array sensors are spaced $50\ \mu\text{m}$ apart and, as depicted above in Figure 2.3, are $1.5\ \mu\text{m}$ square. In comparison, the sensors of Kiewra and Wayner (1989) are $10\ \mu\text{m}$ square. The CC, CL, and FL arrays are shown schematically in Figure 2.8, Figure 2.9, and Figure 2.10, respectively.



(a)



(b)

Figure 2.4 Photographs of (a) a plain silicon wafer, already sawed into individual chips and (b) a single chip.

CONSTRUCTION

The sensor chips were constructed on four-inch wafers of both monocrystalline silicon and amorphous silicon dioxide. Bernard Alamariu supervised their fabrication, which was carried out on the MIT campus, at the Microsystems Technology Laboratory (MTL, building 39). He used standard photolithography methods to process the wafers.

Virtually all microfabrication work today is done with photolithography, which is illustrated stepwise in Figure 2.5. A clean wafer is first inserted into an oven and (a) an oxide film is grown at high temperature on the surface of the wafer. Then (b) a layer of photoresist is spread evenly across the wafer. Photoresist is a resin that changes properties upon exposure to light. (c) and (d) A mask is used to selectively expose portions of the photoresist, and then (e) the unexposed photoresist is chemically dissolved in a process called the photoresist etch. This, in turn, exposes the underlying oxide layer, which is then (f) also selectively dissolved where not covered by the hardened photoresist. Then (g) the hardened photoresist is removed and the wafer placed in a vacuum oven. Here, (h) ions are implanted into the exposed portions of the wafer.

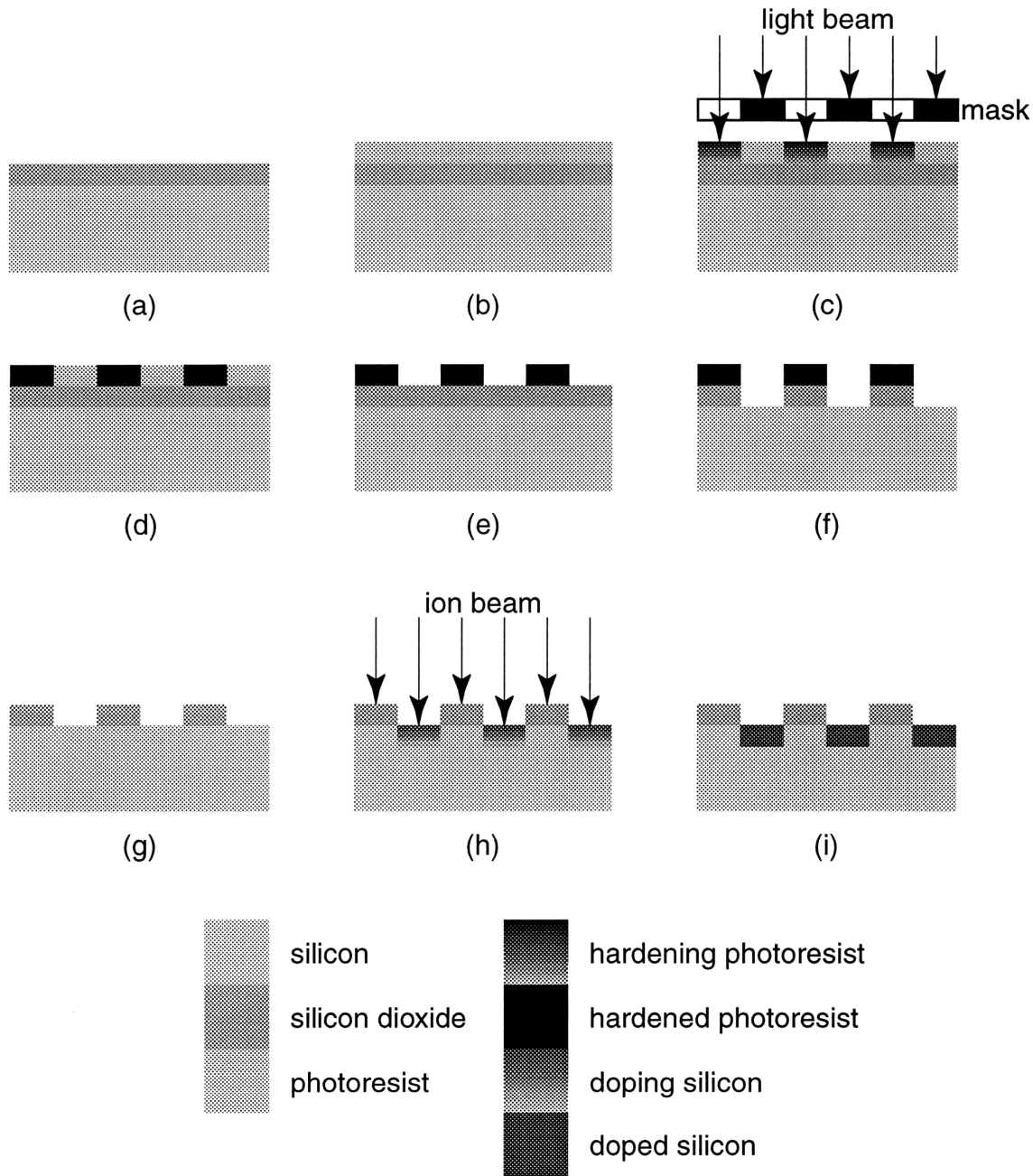
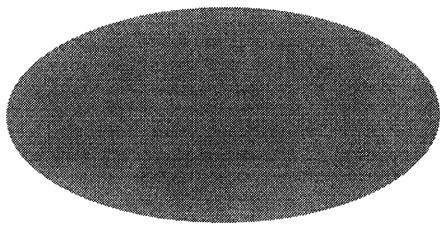


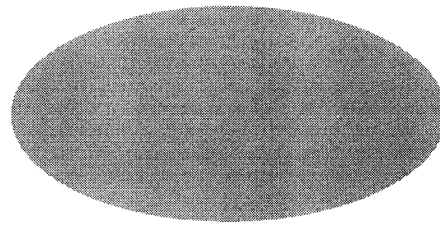
Figure 2.5 Steps in the photolithography process: (a) oxide growth, (b) photoresist coat, (c) photoresist development, (d) mask removal, (e) photoresist etch, (f) oxide etch, (g) developed photoresist etch, (h) ion implantation, and (i) finished doped part. Adapted from Schwarz and Oldham (1993).

As designed, our chip requires four masking processes like those outlined in Figure 2.5. The construction of an actual sensor is detailed in Figure 2.6. Starting with a wafer which has already been oxidized (refer to Figure 2.5 (a)), (a) a layer of polycrystalline silicon (poly-Si) is deposited and (b) boron ions are implanted. Then this poly-Si layer is (c) masked and etched, leaving a “dumb-bell”-shaped region. Most of the poly-Si layer is then (d) bombarded with more boron atoms, leaving the majority heavily n-

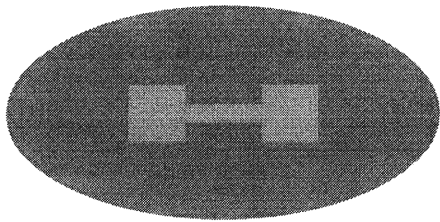
doped, except for a small region in the center, which was protected by photoresist. This center region is the actual sensing element, while the more heavily n-doped regions are electrical contacts. At this point, the wafer is annealed to relieve atomic-scale stresses; these stresses stem from forcing boron atoms into the silicon lattice. After annealing, (e) a very thin layer of silicon dioxide is placed over the sensing element for mechanical protection. Finally, (f) aluminum circuit traces are laid down to connect the sensors with pads at the edge of the chip. These pads must be bonded to the package-well pads in a process known as chip packaging.



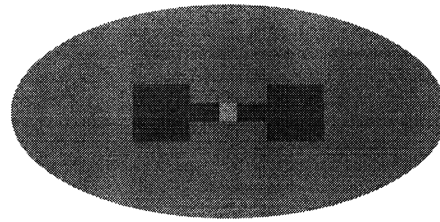
(a)



(b)



(c)



(d)

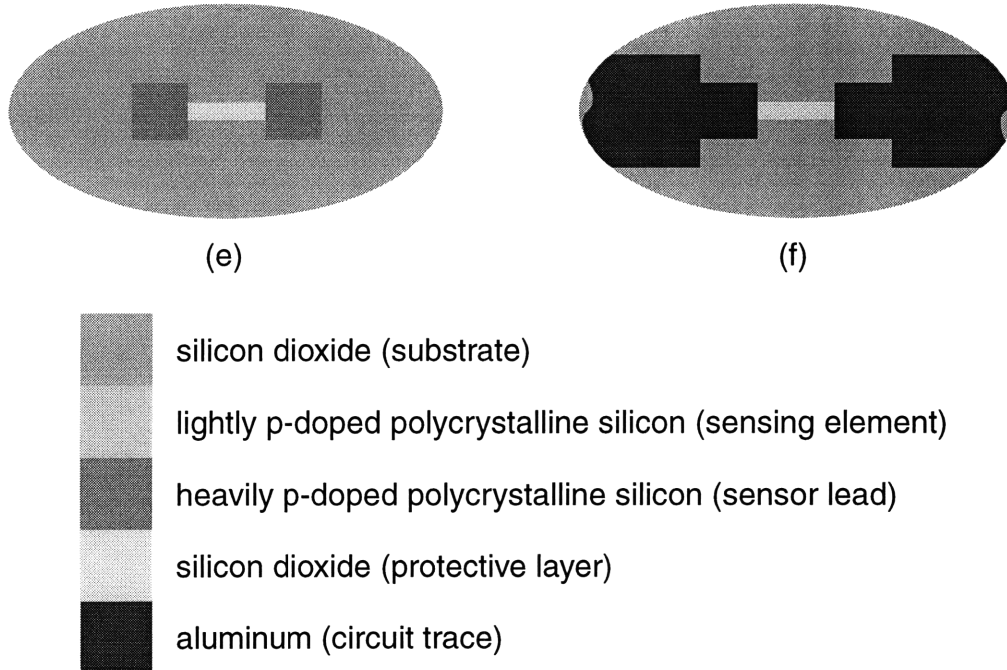


Figure 2.6 Construction of an individual (fine) sensor, top view: (a) initial blank wafer, (b) deposition of n-doped silicon, (c) first mask for etching, (d) second mask for more doping, (e) third mask for protective layer, and (f) fourth mask for circuit traces. Adapted from Qiu (1996).

The actual resistance of any given sensor may vary widely between different chips and wafers. The ion implantation process is closer to a machine-specific recipe, rather than a precise art. Thus, the implanted density depends strongly on operator familiarity with the machine. In addition, during the annealing step to relieve atomic-scale stresses, ions in the doped regions diffuse into surrounding areas. In particular, at the borders between the heavily and lightly p-doped regions, additional boron ions will migrate into the sensing element and reduce the sensor's resistance. Since the fine sensors are smaller than the coarse sensors, this effect will be more dramatic in the fine sensors. Each sensor on each chip must therefore be calibrated before it can be used.

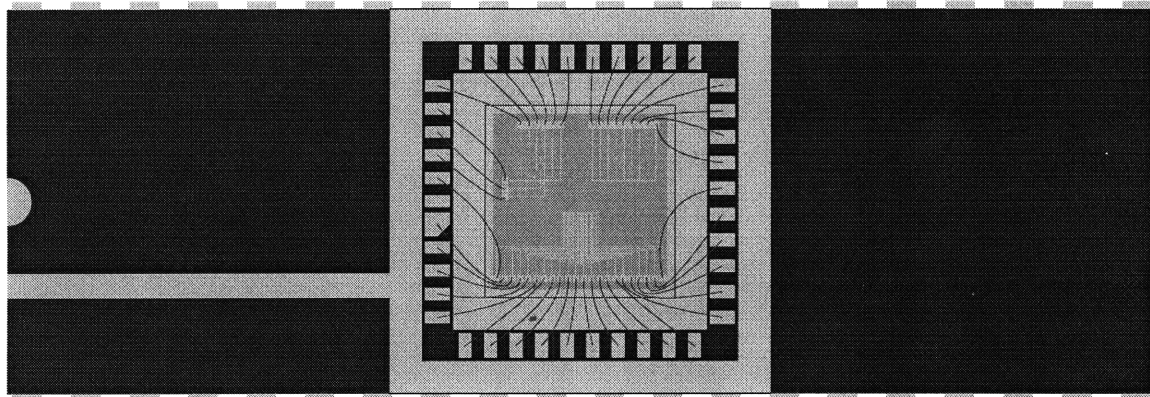
PACKAGING

After wafer processing, the chips are separated and placed in packages. The chip packaging was also carried out at the MTL, under the supervision of Joseph Walsh. Packaging involves three steps: separating the wafer into individual chips, bonding a chip into a package, and electrically connecting the chip to the package leads.

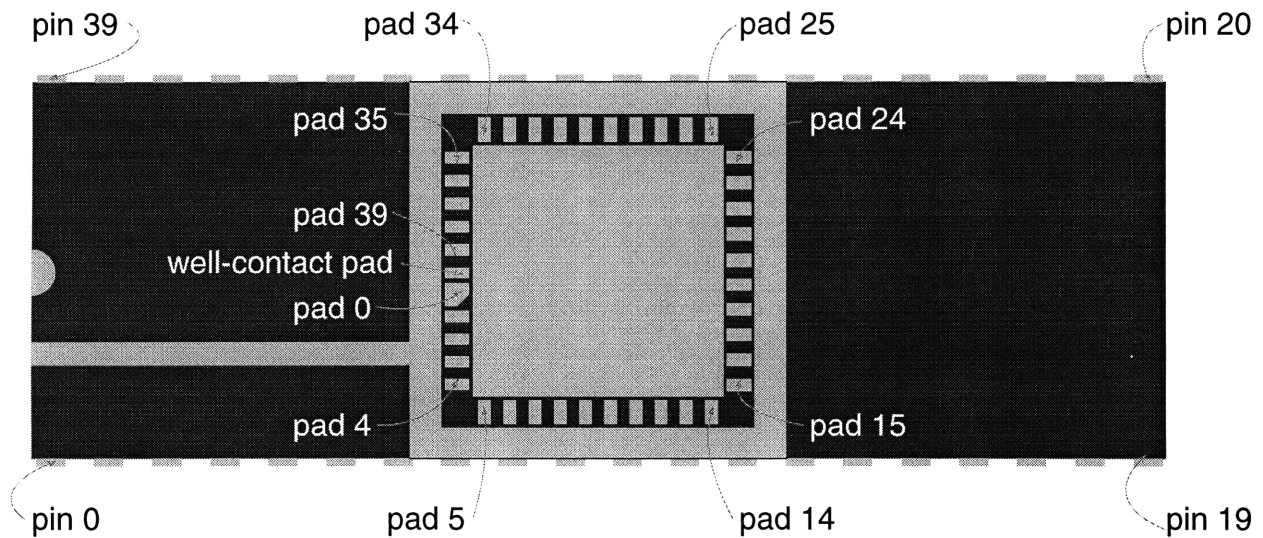
The diesaw is an automated, high-precision saw that separates wafers into chips. It uses a blade that rotates at high speeds and produces a thin cut (typically 2.5 microns wide). The wafer is placed on a piece of single-sided tape (to keep the chips from separating during cutting), which in turn is held onto the

cutting platform by a vacuum. During cutting, cooling water sprays onto the blade. Cuts may be visually verified with the naked eye or through a long-base split-image microscope built into the diesaw.

Electrically conductive epoxy is then used to bond chips into the well of the package. We used standard forty-pin dual in-line packages (DIPs) to use with our sensor chips. Packages are generally made from either ceramic or plastic; we chose to use ceramic packages, as they offer better thermal conductivity than plastic packages. A typical package is shown in Figure 2.7 (b); note the forty-one pads surrounding the well of the package, and the correspondingly numbered pins. The one marked “well-contact pad” is electrically connected to the gold-plated package well rather than an external package pin.



(a)



(b)

Figure 2.7 Schematic of a forty-pin DIP; (a) with chip and wirebonds, (b) showing pin and pad assignments.

Finally, the pads on the chip are linked to the pads in the package well using a wirebonding machine. For our sensor chips, we used a gold-ball bonder, which allows greater flexibility in wire direction than an aluminum-wedge bonder. The wires used are approximately ten microns in diameter. As shown above in Figure 2.7 (a), all of the package well pads are used. The CC, CL, and FL chip-pad assignments are depicted in Figure 2.8, Figure 2.9, and Figure 2.10, respectively. The chip-to package connections are summarized in Table 2.1.

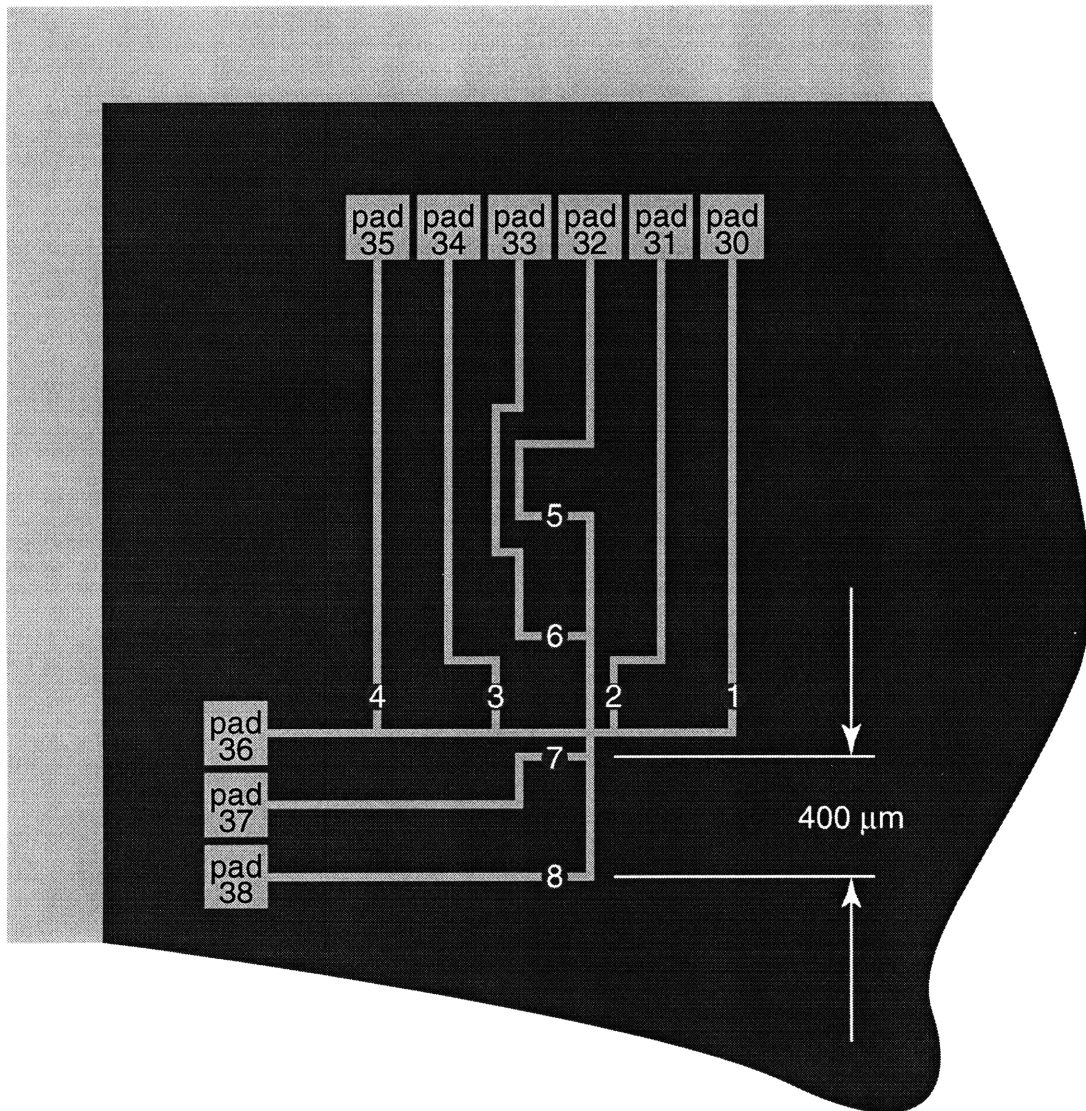


Figure 2.8 Coarse cross (CC) array chip-pad assignments.

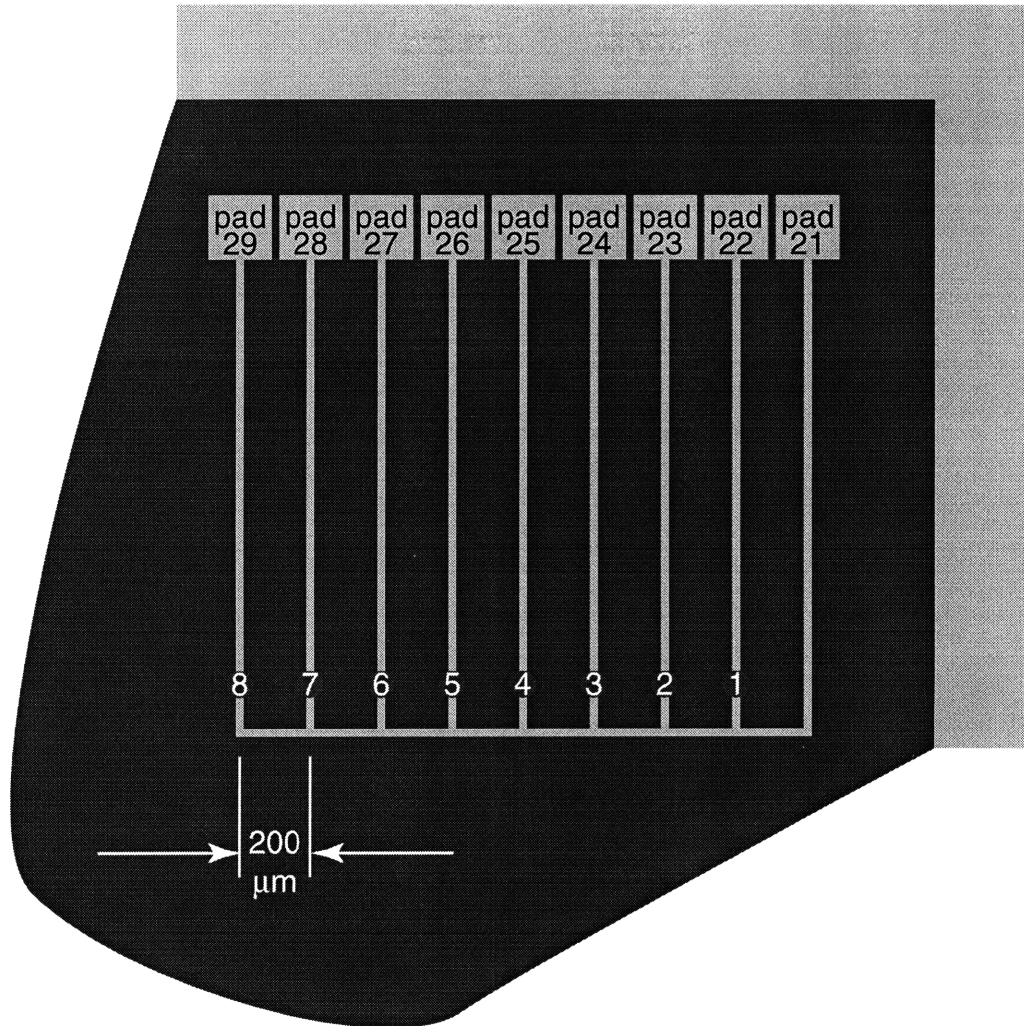


Figure 2.9 Coarse linear (CL) array chip-pad assignments.

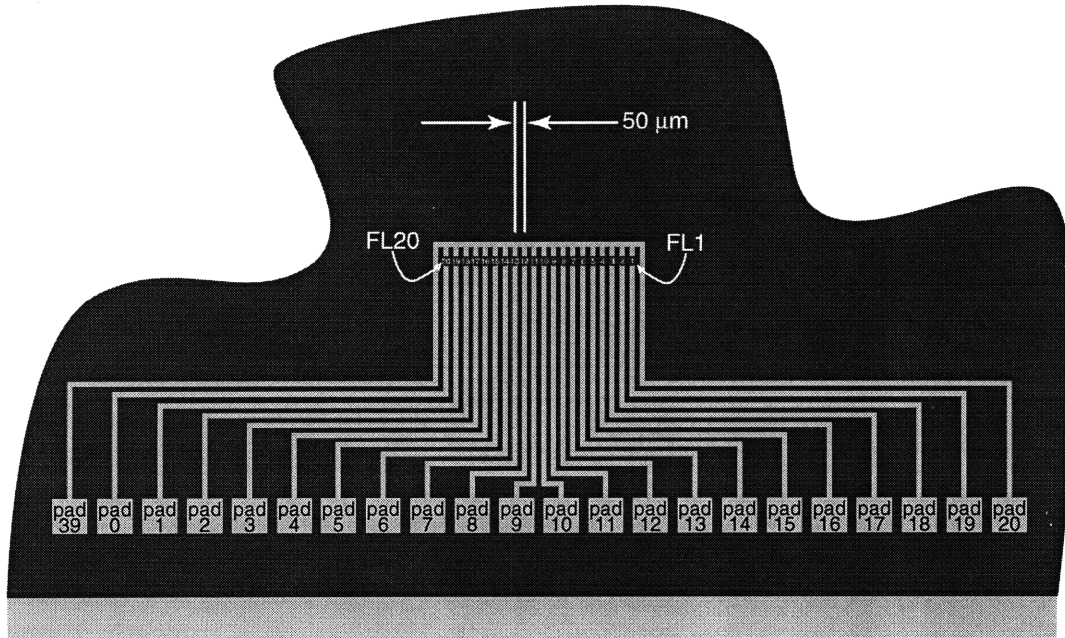


Figure 2.10 Fine linear (FL) array chip-pad assignments.

<i>PACKAGE WELL PAD/PIN ASSIGNMENTS TO SENSOR LEADS</i>							
<i>Left Edge</i>		<i>Bottom Edge</i>		<i>Right Edge</i>		<i>Top Edge</i>	
<i>Pad</i>	<i>Sensor</i>	<i>Pad</i>	<i>Sensor</i>	<i>Pad</i>	<i>Sensor</i>	<i>Pad</i>	<i>Sensor</i>
35	CC4	5	FL15	15	FL5	25	CL4
36	CCCOM	6	FL14	16	FL4	26	CL5
37	CC7	7	FL13	17	FL3	27	CL6
38	CC8	8	FL12	18	FL2	28	CL7
39	FLCOM	9	FL11	19	FL1	29	CL8
0	FL20	10	FL10	20	FLCOM	30	CC1
1	FL19	11	FL9	21	CLCOM	31	CC2
2	FL18	12	FL8	22	CL1	32	CC5
3	FL17	13	FL7	23	CL2	33	CC6
4	FL16	14	FL6	24	CL3	34	CC3

Table 2.1 Sensor chip to package well/pin connections.

In general, the packaging process is straightforward. However, the layout of the chip makes it inconvenient to wirebond to a standard forty-pin DIP easily. Comparing Figure 2.4 (b) with Figure 2.7 (b) shows that the package well and the chip have mismatched numbers of pads per side, leading to circuitous chip-to-well wiring. In addition, the pads on the chip itself are fairly small and difficult to bond precisely. To alleviate these problems, the layout of the circuit traces may be modified as shown in Figure 2.11. The

position, spacing, and number of the sensors remain unchanged, but the chip pad and well pad assignments are now equally distributed per side. However, since the masks have already been made for the current sensor chips, any redesign requires making new masks for the circuit traces, which is an expensive and time-consuming process.

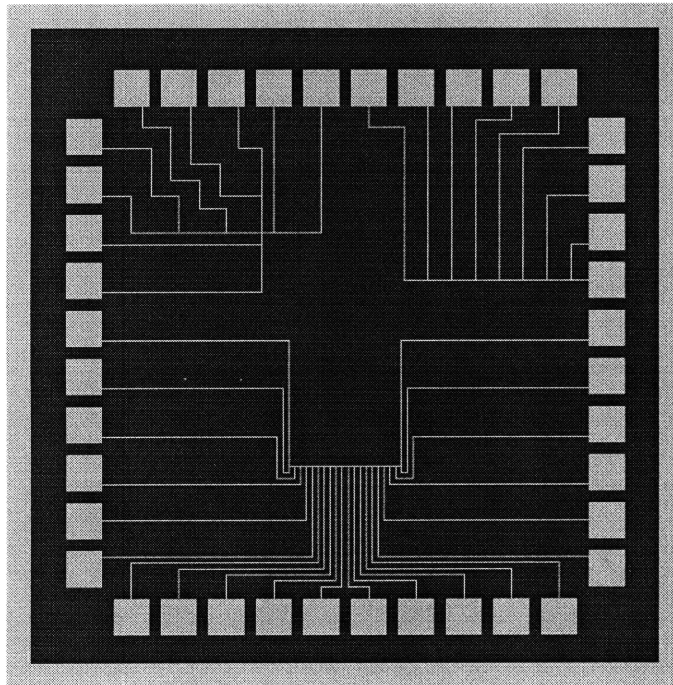


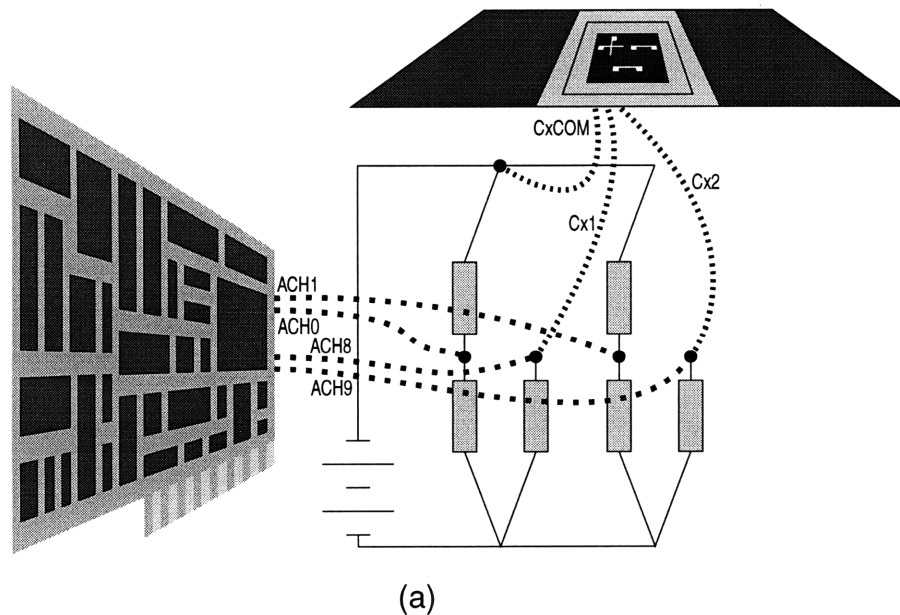
Figure 2.11 Proposed alternative chip circuit trace layout.

CONCLUSIONS

A thin-film thermistor chip has been designed, built, and packaged. Although the concept of small thermistors is not new, the sensors designed by Qiu have unprecedented size and, consequently, thermal response. Because our microsensor chip is not of the “smart” variety, with integrated circuitry for analog-to-digital conversion and signal conditioning, we still need to assemble those components of the system.

Chapter 3 SUPPORT HARDWARE

While our microsensors sense temperature and return resistance information, typical data acquisition systems read voltage signals. Thus, we need conditioning circuitry to change the resistance into something more meaningful (for the data acquisition board) as well as additional software to change the sampled voltage back into resistance data. The hookups between sensor chip package, conditioning circuit, and data acquisition card are shown schematically in Figure 3.1. We also need to heat our packaged sensor chips to a controlled temperature. Since our data acquisition card has a limited number of input channels available, we would like to be able to select the array in use without rewiring the system. This chapter details the circuitry and associated required hardware; Chapter 4 deals with the software.



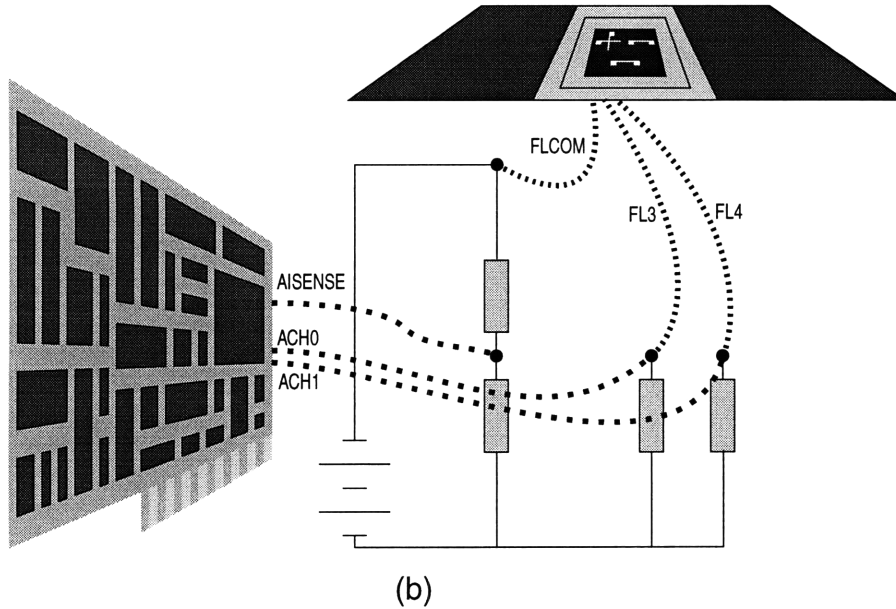


Figure 3.1 Sensor-Circuit-Card connections for the first two sensors in the (a) coarse arrays and (b) fine linear array.

PACKAGE HOLDER

The package holder is shown in Figure 3.2. It has two main functions: bring the chip up to a specific temperature and take signals from the package pins. To heat the chip above the ambient temperature, we installed heaters surrounding the package. Initially, we thought that we could conduct enough heat to the package from a large, controlled thermal reservoir, but when this proved inadequate, we directly attached heaters to the back of the package. Five heaters now control the package's temperature: three cartridge heaters for the thermal reservoir and two cable heaters for the package's back.

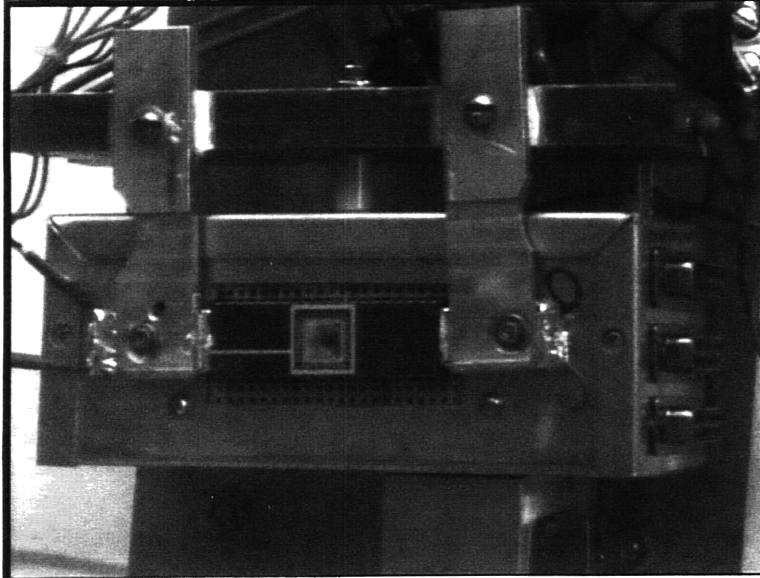


Figure 3.2 Package holder, showing the package socket and the side-mounted sensor array ports.

The side of the package holder has three twenty-five-pin female sockets. From the top of the holder, the connectors correspond to the coarse cross (CC), coarse linear (CL) and fine linear (FL) arrays. Each pin on each socket is attached to a different sensor; the pin assignments are shown in Table 3.1. The strange assignments of the FL connector arise from the numbering scheme of the data acquisition card's input channels. In order to use a common cable for all three connectors, the same input channels must be assigned to the same connector pins.

<i>CONNECTOR PIN ASSIGNMENTS: SENSOR CHIP BOX</i>					
<i>CC Connector (Top)</i>		<i>CL Connector (Middle)</i>		<i>FL Connector (Bottom)</i>	
<i>Pin</i>	<i>Sensor</i>	<i>Pin</i>	<i>Sensor</i>	<i>Pin</i>	<i>Sensor</i>
SCCP1	N/C	SCLP1	N/C	SFLP1	FL3
SCCP2	CC1	SCLP2	CL1	SFLP2	FL11
SCCP3	N/C	SCLP3	N/C	SFLP3	FL4
SCCP4	CC2	SCLP4	CL2	SFLP4	FL12
SCCP5	N/C	SCLP5	N/C	SFLP5	FL5
SCCP6	CC3	SCLP6	CL3	SFLP6	FL13
SCCP7	N/C	SCLP7	N/C	SFLP7	FL6
SCCP8	CC4	SCLP8	CL4	SFLP8	FL14
SCCP9	N/C	SCLP9	N/C	SFLP9	FL7
SCCP10	CC5	SCLP10	CL5	SFLP10	FL15
SCCP11	N/C	SCLP11	N/C	SFLP11	FL8

SCCP12	CC6	SCLP12	CL6	SFLP12	FL16
SCCP13	N/C	SCLP13	N/C	SFLP13	FL9
SCCP14	CC7	SCLP14	CL7	SFLP14	FL17
SCCP15	N/C	SCLP15	N/C	SFLP15	FL10
SCCP16	CC8	SCLP16	CL8	SFLP16	FL18
SCCP17	CC COM	SCLP17	CL COM	SFLP17	FL COM
SCCP18	GROUND	SCLP18	GROUND	SFLP18	GROUND
SCCP19	N/C	SCLP19	N/C	SFLP19	FL1
SCCP20	N/C	SCLP20	N/C	SFLP20	FL2
SCCP21	N/C	SCLP21	N/C	SFLP21	FL19
SCCP22	N/C	SCLP22	N/C	SFLP22	FL20

Table 3.1 Pin assignments for sensor package holder output sockets.

CIRCUITRY BOXES

We have built two circuitry boxes, one for the FL array and another for the CC and CL arrays (the coarse arrays are collectively referred to the Cx arrays). They may be distinguished by a marking in the bottom right corner of the top panel; the FL box is shown in Figure 3.3. The box has two twenty-five pin female sockets on the top panel and two binding posts on the left side. The two sockets are, from top to bottom, the input from the sensor package holder and the output to the data acquisition card. The circuit excitation voltage is applied to the two side-mounted binding posts. Each fine sensor forms one half of a voltage divider, and each coarse sensor forms one half of one leg of a resistance bridge. In the coarse arrays, we wished to minimize the interference between signals, so we used a well-calibrated resistance bridge circuit. For the fine array, we wished to maximize the number of signals available, so we used a simple voltage divider circuit.

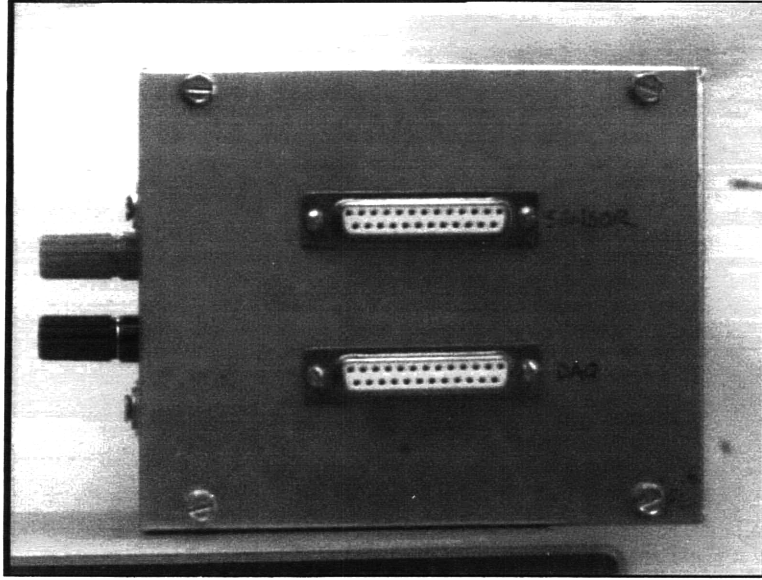


Figure 3.3 Fine Linear circuit box (facing top panel).

The Cx arrays' circuit is shown in Figure 3.4. An excitation voltage is applied across the “EV” terminals, and a large capacitor smoothes out voltage fluctuations from the power supply. The input connections from the sensor package holder are shown at the top of the circuit, and the output connections to the data acquisition card are shown at the bottom. The labels of the give both connector pin and sensor information; the first term refers to the circuit box socket, while the term in parentheses refers to the external connection. For example, the input labeled “SCxP4 (Cx2)” implies that this input is connected to pin number four of the twenty-five pin sensor connector (refer to Table 3.2), which receives sensor number Cx2's input from the sensor chip. Similarly, the output labeled “DCxP4 (ACH9)” is connected to pin number four of the twenty-five pin DAQ connector (refer to Table 3.3), which in turn is connected to analog input channel number ten (ACH9) of the data acquisition board. For coarse sensors, the data acquisition card measures the difference in voltages across the two legs of the bridge. For example, the first differential input is the difference in voltages between the top of “1RFR₁” and the top of “1LFR₁”, or the reading from ACH0 subtracted from the reading for ACH8. Knowing the three fixed resistances in bridge number y, $yLFR_1$, $yLFR_2$, and $yRFR_1$, the resistance of the sensor is

$$SRCx_y = \left[\left(\frac{yLFR_1}{yLFR_1 + yLFR_2} - \frac{DV}{EV} \right)^{-1} - 1 \right] \cdot xRFR_1 \quad \text{eqn. 3-1}$$

where $SRCx_y$ is the sensor resistance, DV is the measured differential voltage between the two legs of the bridge, and EV is the excitation voltage applied to the circuit. For reference, capacitor C1 has a capacitance of approximately 150 μ F, while each fixed resistor is approximately 150k Ω .

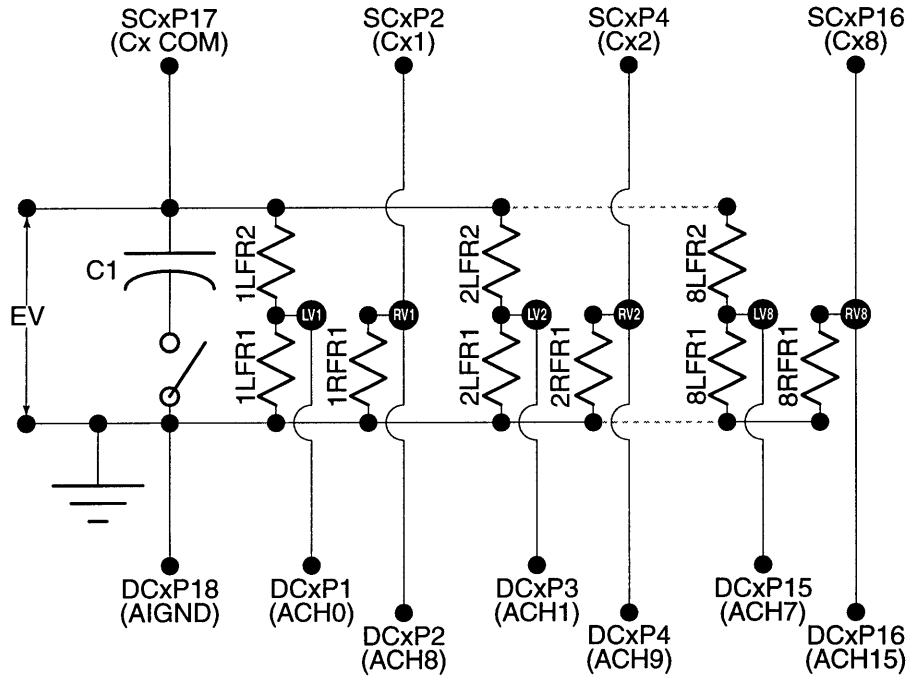


Figure 3.4 Bridge circuit for coarse sensor arrays (CC, CL).

The FL array's circuit is depicted in Figure 3.5. Note the similarities to the Cx arrays' circuit. The "EV" terminals and C1 capacitor act identically to their Cx circuit counterparts. Similarly, the inputs from the sensor package holder are at the top of the diagram and the outputs to the data acquisition card are at the bottom. In the FL array circuit, however, the data acquisition (DAQ) card measures the difference in voltage between an individual voltage divider and a common (reference) voltage divider. For example, the reading taken by the first analog input channel of the card would be the difference in voltages between the top of "3DFR₁" and "1RFR₁" (i.e. the difference between the DAQ card inputs ACH0 and AISENSE). A simple calculation reveals the relation between the sensor's resistance and the measured differential voltage for the yth fine sensor circuit.

$$SRFL_y = \left[\left(\frac{1RFR_2}{1RFR_1 + 1RFR_2} + \frac{DV}{EV} \right)^{-1} - 1 \right] \cdot yDFR_1 \quad \text{eqn. 3-2}$$

Here, $SRFL_y$ is sensor number y 's resistance, DV is the measured differential voltage, EV is the applied excitation voltage, $1RFR_1$ and $1RFR_2$ are the reference circuit's fixed resistances, and $yDFR_1$ is the fixed resistance of divider circuit number y . The value of $C1$ is again, approximately $150\mu\text{F}$, while each fixed resistance is approximately $5.1\text{k}\Omega$.

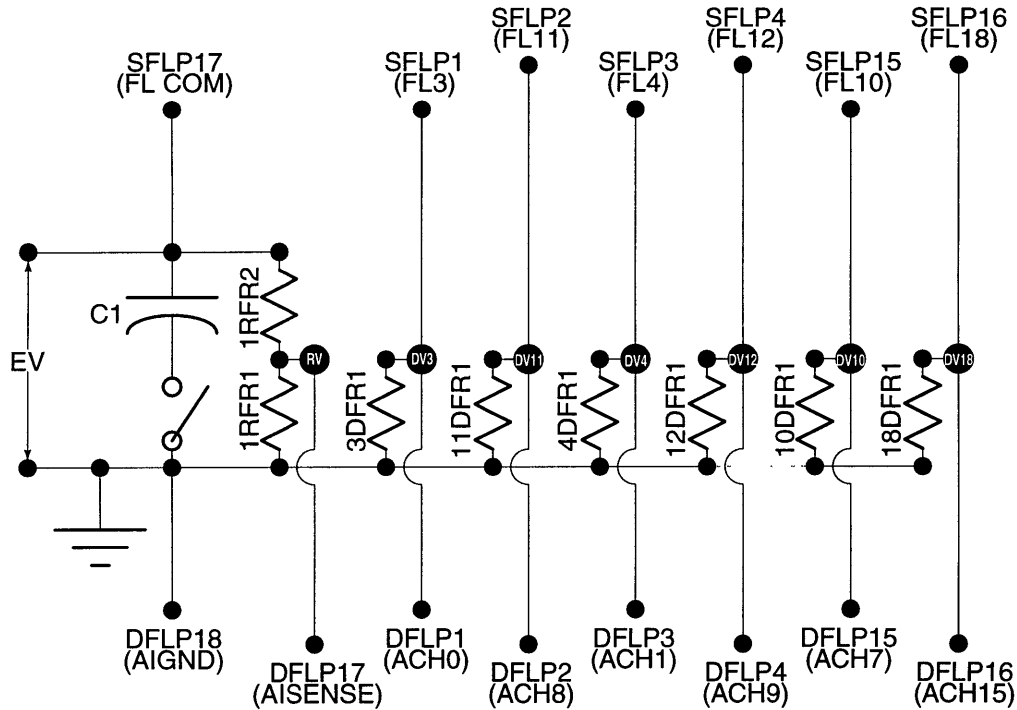


Figure 3.5 Divider circuit for fine linear (FL) sensor array.

The complete pinouts of the two circuit boxes' twenty-five pin connectors are tabulated in Table 3.2 (sensor plug – input) and Table 3.3 (DAQ plug – output). N/C denotes no connection. RV_y, DV_y, and LV_y are connections to the appropriate locations in sensor circuit number *y* of the diagrams in figure 3.4 and Figure 3.5.

CONNECTOR PIN ASSIGNMENTS: CIRCUIT BOX, SENSOR PLUG INPUT			
Coarse Sensor Circuit Box		Fine Sensor Circuit Box	
<i>Sensor Plug Pin</i>	<i>Sensor Circuit</i>	<i>Sensor Plug Pin</i>	<i>Sensor Circuit</i>
SCxP1	N/C	SFLP1	DV3
SCxP2	RV1	SFLP2	DV11
SCxP3	N/C	SFLP3	DV4
SCxP4	RV2	SFLP4	DV12
SCxP5	N/C	SFLP5	DV5
SCxP6	RV3	SFLP6	DV13
SCxP7	N/C	SFLP7	DV6
SCxP8	RV4	SFLP8	DV14
SCxP9	N/C	SFLP9	DV7
SCxP10	RV5	SFLP10	DV15

SCxP11	N/C	SFLP11	DV8
SCxP12	RV6	SFLP12	DV16
SCxP13	N/C	SFLP13	DV9
SCxP14	RV7	SFLP14	DV17
SCxP15	N/C	SFLP15	DV10
SCxP16	RV8	SFLP16	DV18
SCxP17	+EV	SFLP17	+EV
SCxP18	GROUND	SFLP18	GROUND

Table 3.2 Circuit box (sensor connector plug) input pin assignments.

In general, to avoid sensor self-heating, the excitation voltage (EV) should be kept low; one volt is usually enough. At this voltage, the current going through each coarse sensor is on the order of thirty microamps. With a typical voltage drop (across the sensor) of at most 0.5V, the total power dissipation from the sensor into the chip is very small (especially when compared to the heater output power) – on the order of 15 μ W.

CONNECTOR PIN ASSIGNMENTS: CIRCUIT BOX, DAQ PLUG OUTPUT					
Coarse Sensor Circuit Box			Fine Sensor Circuit Box		
<i>Pin</i>	<i>Sensor Circuit</i>	<i>DAQ</i>	<i>Pin</i>	<i>Sensor Circuit</i>	<i>DAQ</i>
DCxP1	LV1	ACH0 (68)	DFLP1	DV3	ACH0 (68)
DCxP2	RV1	ACH8 (34)	DFLP2	DV11	ACH8 (34)
DCxP3	LV2	ACH1 (33)	DFLP3	DV4	ACH1 (33)
DCxP4	RV2	ACH9 (66)	DFLP4	DV12	ACH9 (66)
DCxP5	LV3	ACH2 (65)	DFLP5	DV5	ACH2 (65)
DCxP6	RV3	ACH10 (31)	DFLP6	DV13	ACH10 (31)
DCxP7	LV4	ACH3 (30)	DFLP7	DV6	ACH3 (30)
DCxP8	RV4	ACH11 (63)	DFLP8	DV14	ACH11 (63)
DCxP9	LV5	ACH4 (28)	DFLP9	DV7	ACH4 (28)
DCxP10	RV5	ACH12 (61)	DFLP10	DV15	ACH12 (61)
DCxP11	LV6	ACH5 (60)	DFLP11	DV8	ACH5 (60)
DCxP12	RV6	ACH13 (26)	DFLP12	DV16	ACH13 (26)
DCxP13	LV7	ACH6 (25)	DFLP13	DV9	ACH6 (25)
DCxP14	RV7	ACH14 (58)	DFLP14	DV17	ACH14 (58)
DCxP15	LV8	ACH7 (57)	DFLP15	DV10	ACH7 (57)
DCxP16	RV8	ACH15 (23)	DFLP16	DV18	ACH15 (23)

DCxP17	N/C	AISENSE (62)	DFLP17	RV	AISENSE (62)
DCxP18	GROUND	AIGND (67)	DFLP18	GROUND	AIGND (67)

Table 3.3 Circuit box (data acquisition plug) output pin assignments.

DAQ CARD AND MISCELLANEOUS ITEMS

The data acquisition card is National Instruments' model number AT-MIO-16E-1. Although it can nominally sample 1.25 million samples per second for one channel, the board can only acquire 700 000 samples/second for one channel reliably, because of the card-to-computer interface. This interface is the bottleneck for retrieving scans from the on-board temporary storage buffers.

Up to sixteen channels may be sampled simultaneously. The board reads from these channels in differential or single-ended mode. In differential mode, two channels are used per input; one channel's input is subtracted from the other's to form a single input. In single-ended mode, each channel is measured separately, either with respect to a common reference or to electrical ground. Thus, both eight differential and sixteen single-ended inputs employ all sixteen channels. When multiple channels are in use, the maximum sampling rate will decrease. The absolute maximum product of sampling rate (samples/sec) and number of channels in use is 700 000.

The board has a resolution of twelve bits. That is, it divides its selectable input range into 4 096 (2^{12}) discrete points. Although higher-resolution boards do exist (up to sixteen bits, or 65 536 discrete points), none of them offer similar speed. The input range is nominally $\pm 10V$, but on-board amplification may be employed to change this range as needed. We have found that an input range of $\pm 0.5V$ works well for our sensors; it provides an ideal compromise between noise level and resolution.

A CCD camera and a S-VHS videotape recorder were used to acquire video of the deposition process simultaneously with the thermal sampling. A fiber-optic light guide was used to illuminate the chip. Two deposition apparatus were used to put drops on our chips: the adapted ink-jet head used in previous experiments (Gao (1994), Schiaffino (1996), and Torresola (1998)) and the pendant drop apparatus constructed by Duthaler (1998). We used a standard temperature controller with thermocouple input to keep the package temperature steady.

CONCLUSIONS

A holder was constructed to provide external interfaces for signals from individual arrays on the (swappable) sensor chip package. This holder also has integrated heaters which control the chip's temperature. We used resistance bridges and voltage dividers to convert our micro-thermistors' resistance into readable voltages. These are used with the coarse and fine arrays, respectively, to provide for signal quality (isolation) or number of signals supported. Finally, a data acquisition card takes the voltage data from the circuits and saves the data to disk; those signals are then converted back to resistance and temperature data by software described in Chapter 4.

Chapter 4 DATA ACQUISITION SOFTWARE

We need to translate the voltage data acquired by the computer back into resistance measurements. National Instruments supplied an application-building program, LabVIEW, with the data acquisition card. The overall interdependence of programs written in LabVIEW for data acquisition and conversion is depicted in Figure 4.1. Voltage data are taken from the sensor chip at different temperatures and associated circuitry (see Chapter 3) by a set of calibration programs – “My Calibration AI” and “Grab Save Analyze”. Then, when an actual droplet is deposited on the chip, a set of continuous data are taken with “My Cont Acq to File (binary)”. Using the calibration data, “My Disp Acq'd File (binary)” translates the raw voltage data into resistance data. The data are then reduced by two programs – “Array Subsetter” and “Array Slicer” – and subsequently plotted versus time by “Sliced Array Plotter”.

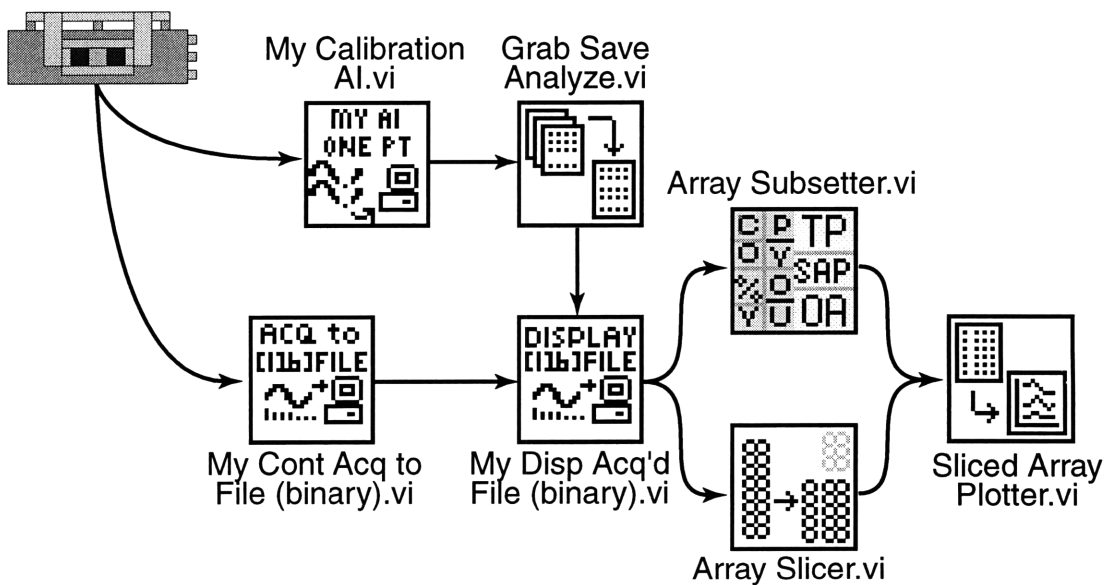


Figure 4.1 Software used to process voltage information from sensor chip.

The core code of the data acquisition programs are borrowed and modified from National Instruments’ example programs. “My Calibration AI” comes from the built-in program “AI Sample Channels”. Similarly, “My Cts Acq to File” is a modification of “Cont Acq to File (binary)” and “My Disp Cts Acq’d File” comes from “Display Acq’d File (binary)”. Modifications were made to improve performance and to customize the programs’ capabilities.

The two data acquisition programs (MCAI and MCAF for calibration and continuous acquisition, respectively) both create data files. These programs will suggest filenames based upon various user-set

parameters. It is generally advisable to keep data files segregated by array type (CC, CL, FL) and type of acquisition (calibration, continuous).

SINGLE-POINT CALIBRATION

Single-point calibration is carried out through two programs, “My Calibration AI” (MCAI) and “Grab Save Analyze (cal)” (GSA). MCAI takes a series of voltage readings at a specific temperature over a set amount of time, converts the voltages to resistance measurements, averages these resistance measurements, and saves the results in a tab-delimited text file. GSA scans a specified set of MCAI output files, grabs the average readings, performs a limited analysis with the data, and saves the results in another tab-delimited text file. Together, these programs provide a simple and convenient way to read and average many results over a wide range of temperatures.

The front screen for MCAI is shown in Figure 4.2. The important user controls are, from top to bottom, the Excitation Voltage (EV) Control, the Temperature Control, the Circuit Box Selectors, and the Sampling Controls. The EV Control tells the program what the voltage applied to the circuit box is, and must be filled in by the user in order for MCAI to convert voltage into resistance properly. The excitation voltage may be read with a standard hand-held multimeter or estimated from the analog meter on the front panel of the power supply. The Temperature Control affects the output filename; it should be changed for each successive temperature measurement to reflect the temperature controller display. Furthermore, changing each measurement by a consistent amount (e.g. five degrees per successive file) ensures that GSA will find the correct MCAI output files. The Circuit Box Selectors tell MCAI which circuit box is being used. Click on the top slider to change between the fine sensor box (with voltage dividers) or the coarse sensor box (with resistance bridges). Click on the lower slider to change between the new-style boxes (small, silver boxes without potentiometers) or the old-style boxes (old, white boxes with potentiometer shafts). The Sampling Controls govern the number and frequency of sampled points; the top control sets the number of samples to take, and the bottom control sets how much time to take in sampling them.

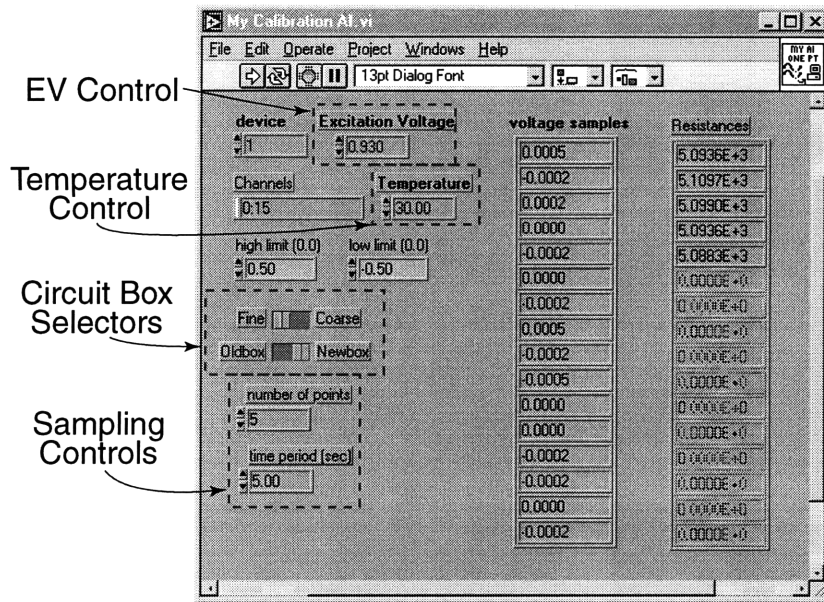


Figure 4.2 “My Calibration AI” (MCAI) reads, converts, and averages a series of sensor resistance measurements.

When the operator runs MCAI, after setting the controls appropriately, the program simultaneously reads voltage samples from each sensor. These samples are converted to a resistance, based on the theory outlined in Chapter 3. MCAI continues to read and convert more samples until it reaches the limit set by the Sampling Controls. Then the program performs a basic statistical analysis on each sensor, returning the standard deviation and average of the readings for each sensor. Once the calculations are complete, the file is saved as a tab-delimited text file, in which a two-dimensional array of numbers is written with tab characters separating columns and carriage returns separating rows.

A typical MCAI output file is depicted in Figure 4.3; in this file, ten samples were taken and saved. Each column corresponds to a different sensor. The first set of rows before the row of separator zeroes (in this case, ten rows) are the successive sensor readings. The rows immediately following the separator zeroes are, respectively: the standard deviation of the resistance measurements for a single sensor, the standard deviation as a percentage of the average, and the average of the readings. Note that the output filename – in this case, *CC-40.0-0.889V-cal.ss* – contains information about the sensor array, temperature, and excitation voltage. In general, MCAI writes files with the name *XX-yy.z-zzzV-cal.ss*. *XX* is the sensor array in use; it defaults to either *FL* or *Cx*, depending on the Circuit Box Selector position. *yy.y* is the temperature in degrees Celsius, and is controlled by the Temperature Control. *z.zzz* is the excitation voltage set by the EV Control.

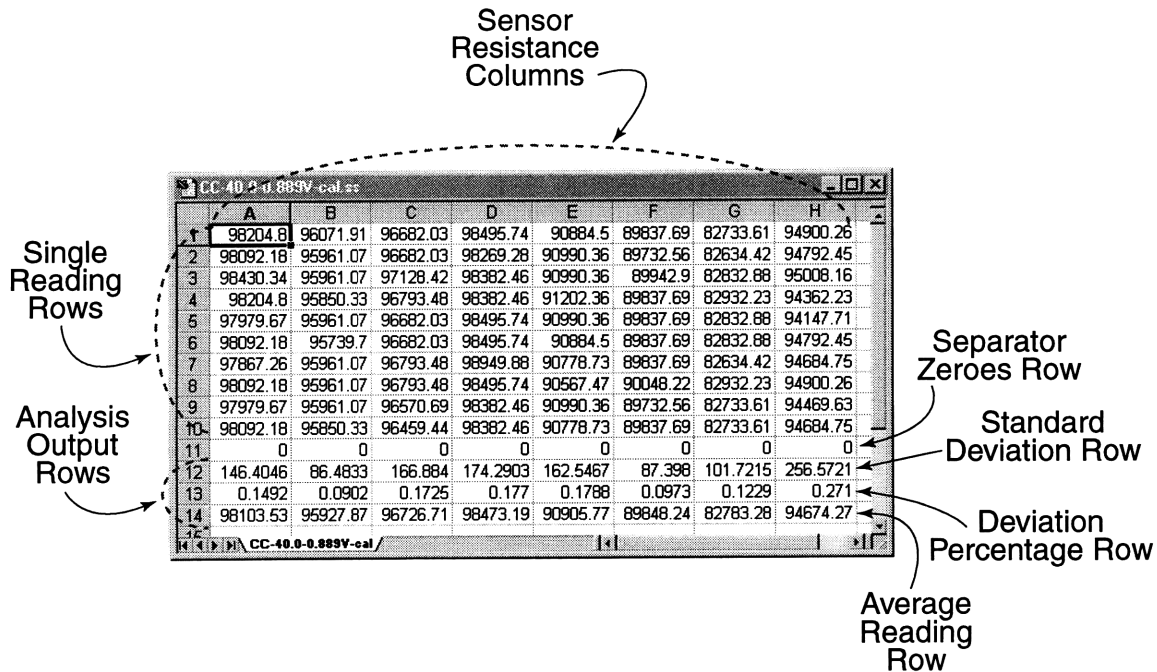


Figure 4.3 Typical “My Calibration AI” output.

The GSA front panel is shown in Figure 4.4. Its main controls are, from the top, the Initial Temperature Control, the Final Temperature Control, the Temperature Step Control, the Array Selector, and the Correlation Selector. The Initial Temperature Control tells GSA which temperature is the reference temperature for the data. The Final Temperature Control tells GSA which temperature is the last one in the series taken with MCAI. The Temperature Step Control tells the program how many degrees to skip between files when seeking for names. The Array Selector has the same function as the top Circuit Box Selector in MCAI, and is set according to which array is in use. The Correlation Selector chooses which type of additional curve fit is returned: a NTC or a NTCexpT thermistor fit (these curves are detailed in Chapter 8).

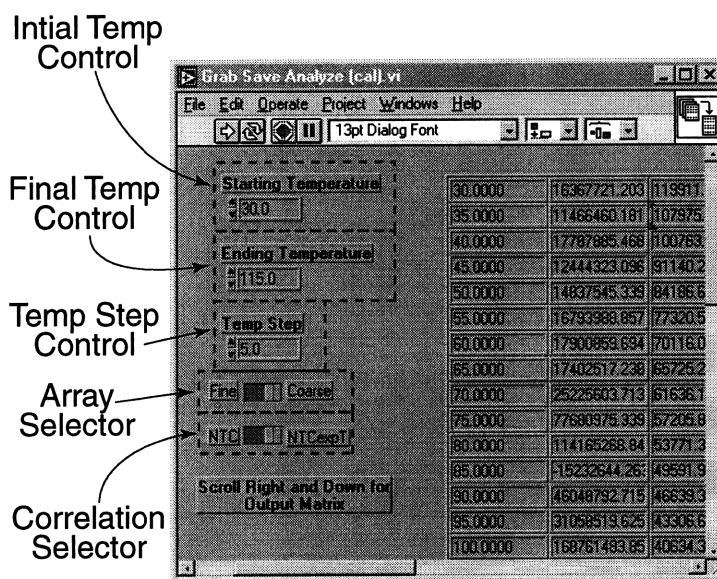


Figure 4.4 “Grab Save Analyze (cal)” (GSA) sorts and analyzes MCAI output files.

According to the current settings, the program will ask you to open a MCAI output file with the name *Cx-30.0-z.zzzV-cal.ss*. It then reads the last line of that file, which contains the average reading from each sensor, as outlined above, and saves that line in a temporary array. Then it proceeds to open *Cx-35.0-z.zzzV-cal.ss*, read its last line, and appends that line after the first in the temporary array. GSA continues to open and read more MCAI output files (in five degree increments, according to the Temp Step Control in Figure 4.4) until it reaches the last file to read, which is *Cx-115.0-z.zzzV-cal.ss*, according to the settings shown. After all of the readings have been taken, GSA performs a limited analysis by normalizing each column with the initial resistance reading (i.e. the one corresponding to the temperature set in the Initial Temperature Control). It then fits each sensor’s normalized temperature-resistance response to an exponential curve. Depending on which correlation is selected, it performs another exponential fit on the averaged resistance readings (i.e. non-normalized). The program appends these normalized values and the exponential fit coefficients to the end of the temporary array. Finally, it saves the array in another tab-delimited text file, which is depicted in Figure 4.5.

The GSA output file is named *XX-yy.y_ww.w-tn-z.zzzV-cal.ss*, where *XX* and *z.zzz* are the same as for each MCAI output file, and *yy.y_ww.w* are the temperatures set by the Initial Temperature Control and the Final Temperature Control, respectively. *tn* denotes the type of additional correlation selected; *t1* means that the NTC fit was used, while a *t2* file uses the NTCexpT fit. Again, each column of the GSA output file corresponds to a different sensor, except for the first column, which contains temperature data. The rows before the first row of separator zeroes are the averaged resistance readings from each MCAI output file (i.e. for each temperature). The very first row (of this group) comes from the MCAI output file

whose temperature is specified by the Initial Temperature Control; the last row comes from the MCAI output file for the temperature specified in the Final Temperature Control. The rows preceding the second row of separator zeroes are the normalized average resistance readings for each MCAI output file. In this group of rows, the temperature is expressed as a temperature difference (i.e. the difference between the actual temperature and an arbitrarily chosen reference temperature). By default, the temperature selected by the Initial Temperature Control is the reference temperature. The resistance readings are normalized by dividing individual readings by the resistance of the same sensor at the reference temperature. The next row after another row of zeroes separated from the normalized average resistance readings by a row of zeroes contains the argument for the exponential curve fitted to the normalized readings. The last two rows are reserved for coefficients in either the NTC or the NTCexpT fit; in this case, the NTCexpT fit was used. For more details on using these coefficients to obtain a numerical fit, please refer to Chapter 8.

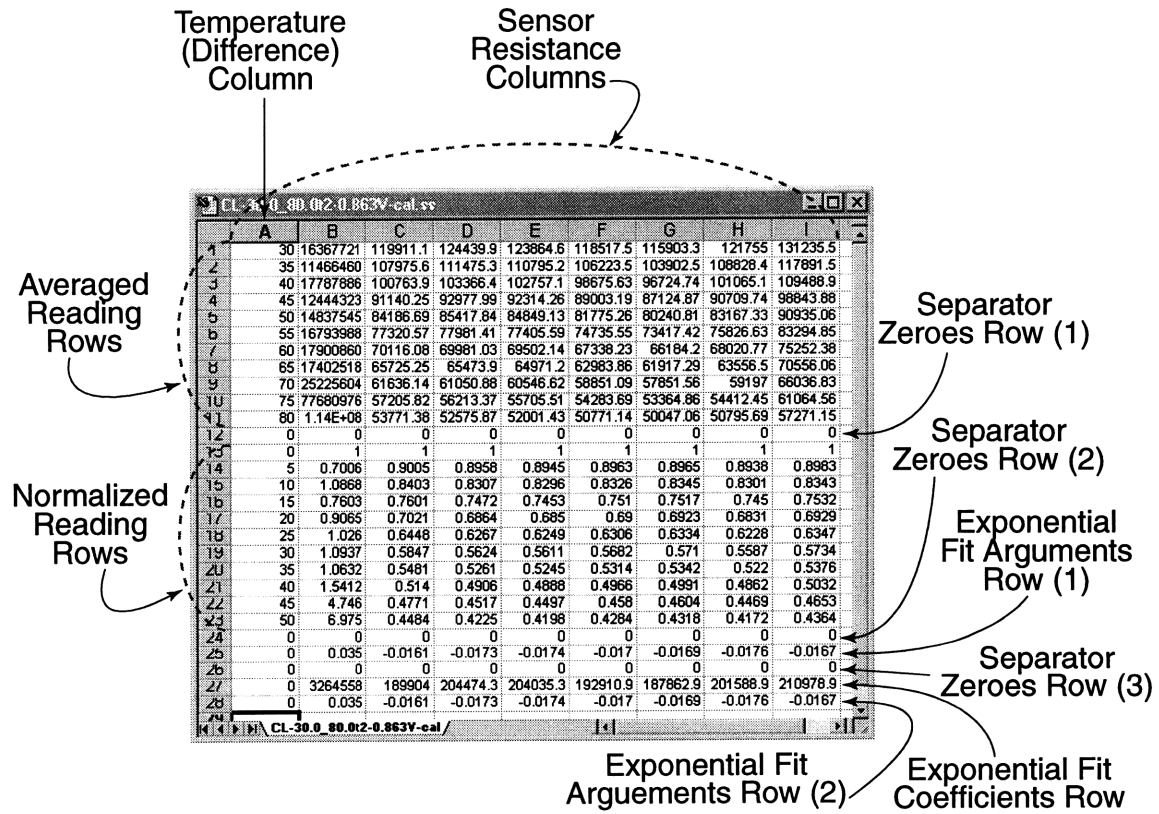


Figure 4.5 Typical “Grab Save Analyze (cal)” (GSA) output file.

CONTINUOUS ACQUISITION

Continuous data acquisition is similarly handled through two separate programs, “My Cts Acq to File” (MCAF) and “My Disp Cts Acq’d File” (MDAF). MCAF continuously samples each channel’s voltage at a preset scanning rate for a set amount of time. The results are directly saved into a binary file,

for compactness and speed. MDAF reads the voltage data from the MCAF binary output file, converts it into either a temperature or resistance change, and saves the results in a tab-delimited text file.

The front panel and major controls of MCAF are shown in Figure 4.6. The main controls, from top to bottom, are the Excitation Voltage (EV) Control, the Temperature Control, the Auto/Manual Channel (AMC) Selector, the Acquisition Rate Control, the Array Selector, and the Acquisition Time Control. The EV Control, Array Selector, and Temperature Control all serve the same functions as they do in MCAI, except for the EV Control. Since MCAF does not convert the voltage readings into resistance or temperature measurements, the EV control serves to name the file; however, this value is passed on to MDAF, which does use the value in converting voltage to temperature. In the interest of maximum temporal performance, MCAF directly saves voltage readings into a binary file.

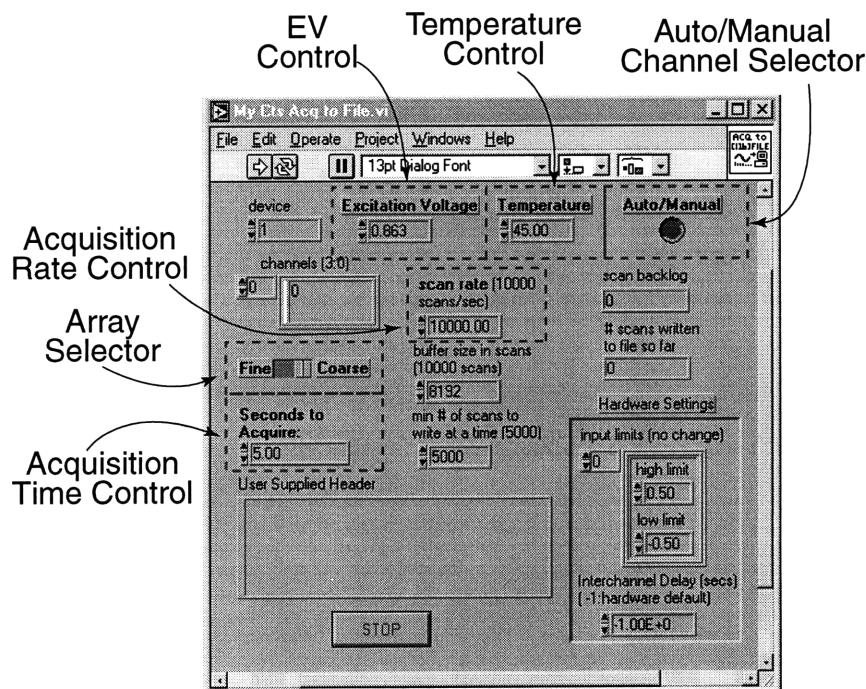


Figure 4.6 “My Cts Acq to File” (MCAF) scans specified input channels for a set time and saves directly to disk.

The Acquisition Rate Control and Acquisition Time Control govern the speed and period of acquisition. The maximum scanning rate is controlled by the Industry Standard Architecture (ISA) Bus interface used by the data acquisition card and the number of channels in use, as described in Chapter 3. Experimentation with different settings leads us to recommend setting the Buffer Size to approximately 200% of the sampling rate, and the Minimum Number of Scans to Write to approximately 70% of the sampling rate.

We wrote a subroutine to sample data from a specified set of channels. This is controlled through the AMC Selector. When it is engaged, as shown in Figure 4.6, the “automan” subroutine, illustrated in

Figure 4.7, pops up when MCAF is started. This subroutine’s two main controls are the Channel Selectors and the Dialog Dismissal Controls. The Channel Selectors choose which analog input channels will be active for the data acquisition period. Note that the channel numbering system reflects National Instruments’ system of 16 channels numbered 0 through 15. When in differential acquisition mode (i.e. working with a coarse array), only the first 8 channel selectors (0 through 7) will be active. After selecting the desired channels, click on the “OK” Dialog Dismissal Control to begin acquisition. “Cancel” is the last chance to abort the acquisition.

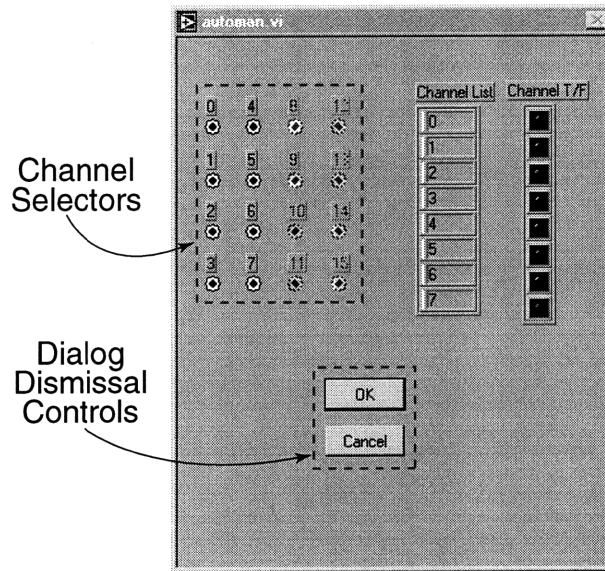


Figure 4.7 The “automan” subroutine selects the channels to be used during data acquisition.

Once the voltage data have been acquired with MCAF, MDAF converts this raw binary data into a tab-delimited text file suitable for export into standard spreadsheet and statistical applications. The front panel of MDAF is shown in Figure 4.8. Its major controls are the Temperature Control, the Circuit Box Selectors and the Output Selector, from top to bottom. The Temperature Control and Circuit Box Selectors are the same as their counterparts in MCAI. The Output Selector switches the written data output between normalized sensor resistance and temperature. Since MDAF does not overwrite the raw voltage data, it is possible to generate separate normalized resistance and temperature deviation files, which may be useful for checking the accuracy of the voltage-to-resistance conversion. Temperature data is generally more useful.

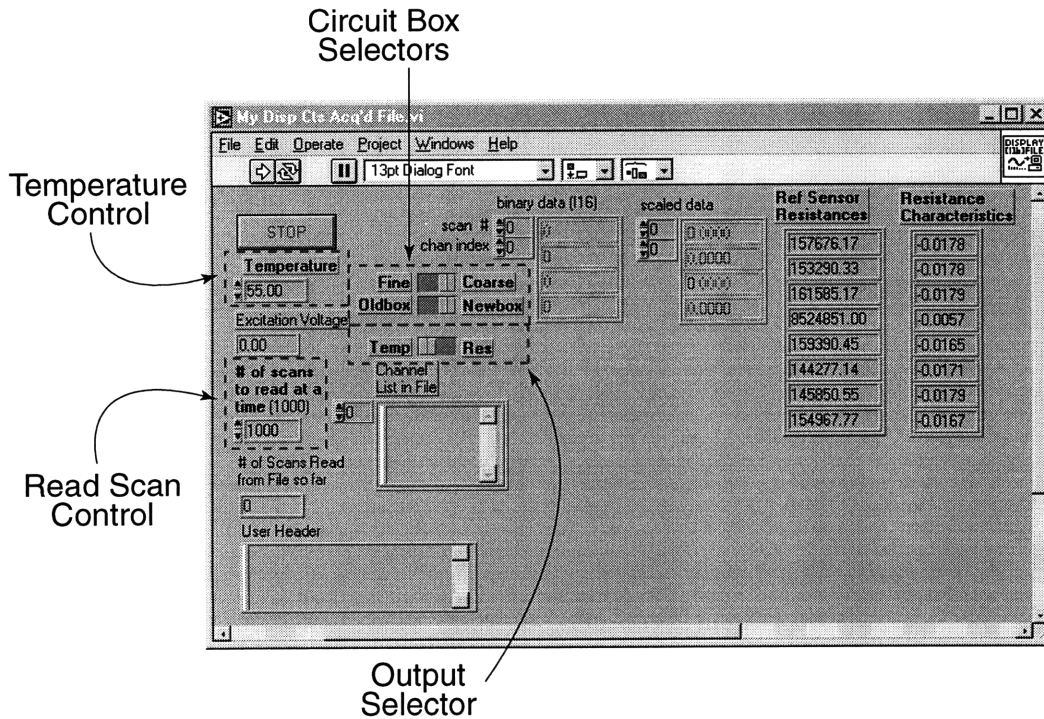


Figure 4.8 “My Disp Acq’d File” (MDAF) converts binary voltage data into ASCII-text resistance data.

MDAF prompts the user to select a GSA output file to load into the Reference Sensor Resistance and Sensor Resistance Characteristics displays. These numbers tell MDAF how to model the sensors’ behavior. Depending on the additional correlation type selected by the Correlation Selector in GSA (Figure 4.4), MDAF will load either the NTCexpT correlation data (for GSA files with “t2” in the name) or the normalized exponential correlation data. MDAF knows which channels were used to acquire data and will use the appropriate correlation data. Using the normalized exponential correlation yields a temperature deviation, i.e. the difference between the actual temperature and a reference temperature, while the NTCexpT correlation yields the actual temperature.

DATA REDUCTION AND GRAPHING

This system can sample data at a prodigious rate – five seconds of data sampled from one differential channel at 333 kHz translates to more than 1.5 million data pairs (time and resistance). The resulting tab-delimited text file from MDAF turns out to be close to thirteen megabytes in size. This file must be sifted to extract useable data, so we wrote three more programs: “Array Subsetter” (ASub), “Array Slicer” (ASli), and “Sliced Array Plotter” (SAP). ASub automatically searches through the MDAF output file for significant deviations from the average value, cuts out a subset of data surrounding that deviation, and appends time information to the subset. ASli performs the same job, but the subset selection is manually controlled. Finally, ASli and/or ASub output files are sent to SAP for plotting.

The ASub front panel is shown in Figure 4.9. Its main controls are the Sensor Info Control, the File Position Controls, the Search Parameter Controls, the Search Type Sliders, and the Time Step Control. ASub searches one column (i.e. one sensor's output) of a MDAF output file for a deviation from the average value. The Sensor Info Control tells ASub the total number of sensors that data were acquired from, which corresponds to the number of columns in the file. The File Position Controls tell ASub which column to search and at which row to begin the search. Note that LabVIEW counts from zero (i.e. its column number zero is the first column of the file) for both row and column. The Search Parameter Controls determine the deviation value to search for. Either a percentage of the average or a specific value may be used for the deviation value; the top Search Type Slider determines whether the percentage or specific value is used. The bottom one specifies whether the deviation is above or below the average value. Finally, the Time Step Control tells ASub the amount of time elapsed between successive steps. This information is used to append a time scale to the output file. Because ASub reads the entire file (in order to obtain an average value) before performing its search, it runs very slowly on large files. MDAF output files that are larger than fifteen megabytes should be chopped up into useable chunks with ASli and manually searched (using SAP) instead of relying on ASub.

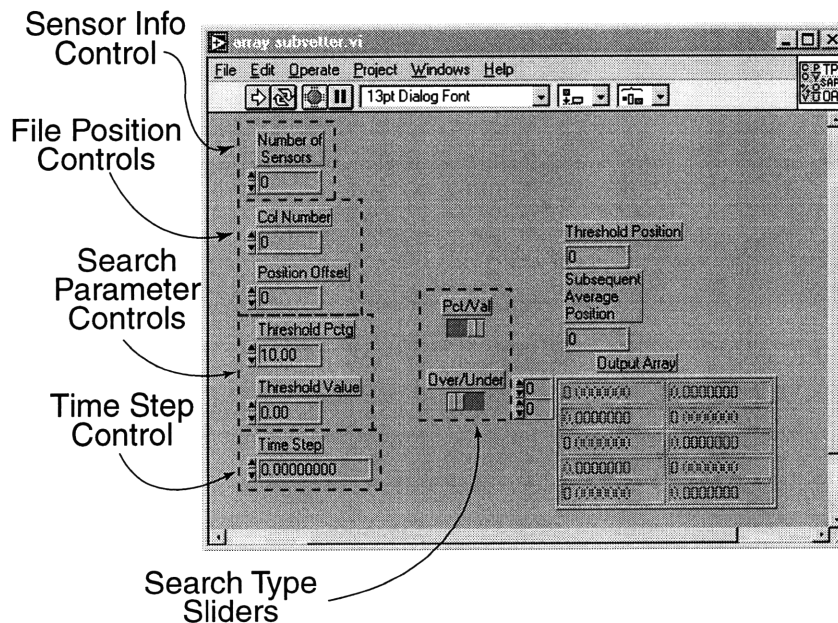


Figure 4.9 “Array Subsetter” (ASub) scans a single column of a MDAF output file for certain values, cuts out a subset of the MDAF file, and appends time information to it.

A typical ASub output is shown in Figure 4.10. The main feature of this file is the five-row header. The first row contains the time step specified in ASub's Time Step Control and the average value of the column specified. Note that the average is taken from the row of the MDAF output file specified in the File Position Controls to the end of the file. A row of separator zeroes follows this row. The next two rows contain information about the ASub output file. The first of these rows gives the initial position, in

both time and row number, of the ASub output file relative to the first row of the MDAF output file. The second row gives the final position of the ASub output file, in both time and position. The actual time-temperature information follows after another row of separator zeroes. ASub-generated files are named *XX-yy.y-z.zzzV-cts-colm-l.sset*. *XX*, *yy.y*, and *z.zzz* the same as in an MCAI output file; *colm* refers to the column number searched, and *l* is the starting row position of the search; both are numbered starting from one, instead of the LabVIEW convention.

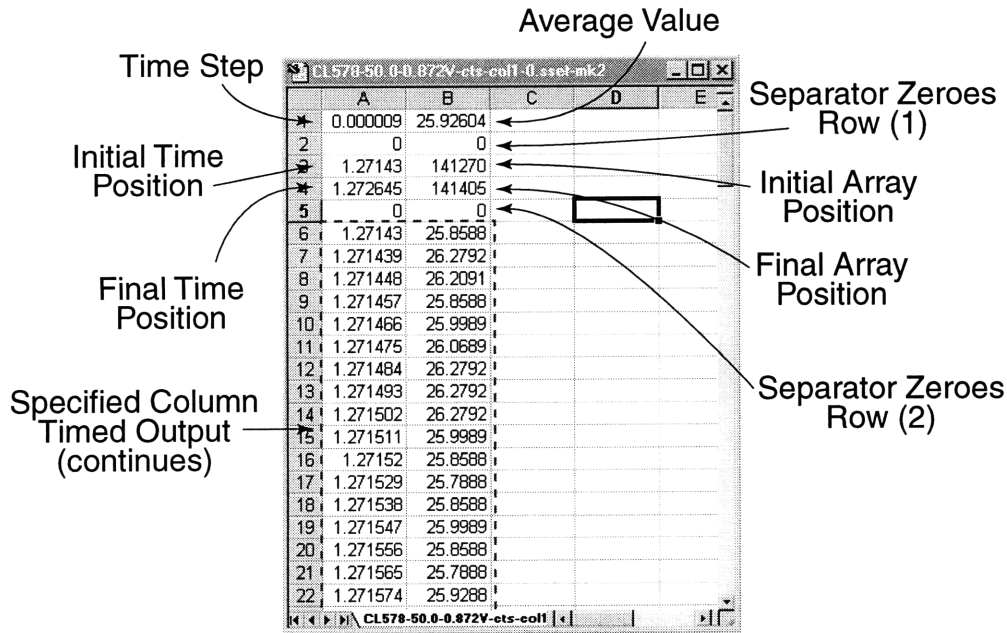


Figure 4.10 Typical “Array Subsetter” (ASub) output file.

ASli, as illustrated in Figure 4.11, has the Sensor Info Control, the File Position Controls, the All/Single Slider, the File Length Control, and the Time Step Control as its main controls. ASli cuts out a manually-specified subset of a MDAF output file and appends time information to it. The Sensor Info Control, File Position Controls, and Time Step Control all work the same way as in ASub. ASli can slice out either a single column or take all of the columns. This option is controlled by the All/Single Slider. Note that the specified column number of the File Position Controls is active only when the All/Single Slider is set to “single” (i.e. to the right). The File Length Control specifies how many samples are taken from the MDAF output file; as before, the samples start at the row specified in the File Position Controls. The ASli output file resembles the time-temperature data of an ASub output file, without the five-row header. ASli-generated files have a filename similar to ASub files – *XX-yy.y-z.zzzV-cts-colm-l.slice*; since ASli can generate files from all of the columns, *colm* (referring to the column number) becomes *colAll* when all columns are used.

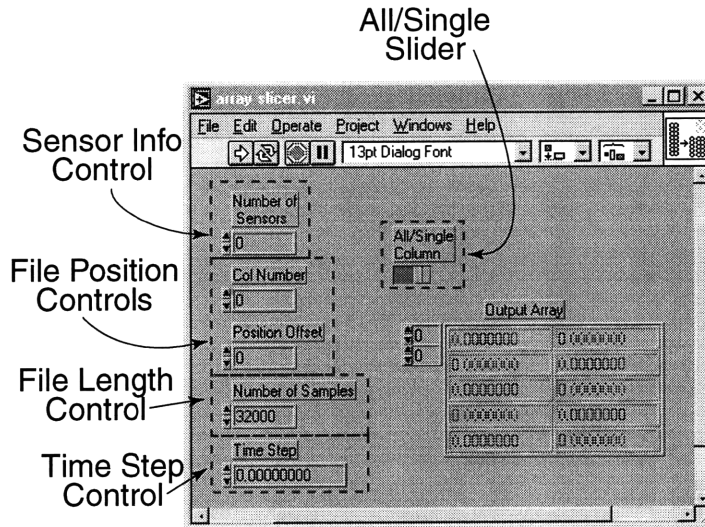


Figure 4.11 “Array Slicer” (ASli) manually cuts out a subset of a MDAF output file.

Despite its name, Sliced Array Plotter (SAP) can plot output files from both ASub and ASli. When running, it asks for an output file from one of the above programs. As shown in Figure 4.12, there is only one set of controls, the Plot Range Controls. After plotting the file, the name of the file will appear in the filename display. The Plot Range Controls specify the x and y ranges shown in the plot window; the two controls on the far left are the auto-scaling controls. When the operator clicks on one of them, the appropriate axis will have its limits set so that the entire range will be shown. The magnifying glass zooms in to certain portions of the chart, and the hand scrolls the plot display around the plot range.

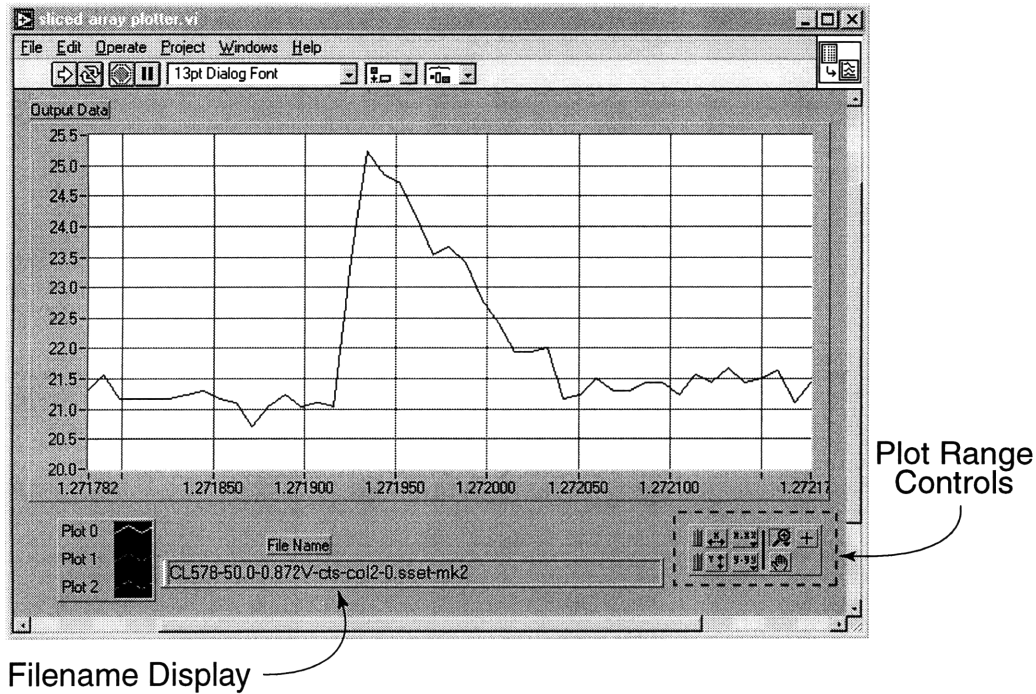


Figure 4.12 “Sliced Array Plotter” charts temperature as a function of time, from ASli or ASub output files.

CONCLUSIONS

Software was written to cover most aspects of data acquisition (calibration, continuous scanning, and data reduction/visualization) with our sensor chips. The core data acquisition code was modified from National Instruments example programs. Each program has been tested and extensively debugged to ensure proper operation and provide new features. Many tedious functions, such as sorting and averaging data, have been automated.

Chapter 5 SMOOTH SILICON DEPOSITION

Previous experiments (Gao (1994), Schiaffino (1996), Duthaler (1998), Torresola (1998)) in our group have studied the deposition of molten material on targets of the same (solidified) material or with similar thermal properties. However, both silicon and amorphous silicon dioxide, the two substrates used in our sensor chips, have much larger thermal conductivity than that of microcrystalline wax (Reed 6882) or octacosane ($C_{28}H_{58}$), the molten materials we used. Thus, we wanted to determine the behavior of these melts while spreading on a silicon target. We obtained blank, polished silicon wafers and used an adapted thermal ink-jet print head to spread macrodrops on them.

The first experiments determined the apparent post-solidification contact angle. We assumed that the contact line does not recede as the target is cooled and that the droplet forms a spherical cap shape. By measuring the diameter of the contact radius, the apparent contact angle follows from

$$\frac{r_b}{a} = \left(\frac{4N \sin^3 \theta}{(1 - \cos \theta)^2 (2 + \cos \theta)} \right)^{1/3} \quad \text{eqn. 5-1}$$

where r_b is the contact radius, a is the radius of individual droplets in the stream, N is the total number of droplets deposited, and θ is the apparent contact angle, as shown in Figure 5.1 (a). Similarly, for droplets where $\theta > \pi/2$, the apparent contact angle may be calculated from

$$\frac{R_c}{a} = \left(\frac{4N}{(1 - \cos \theta)^2 (2 + \cos \theta)} \right)^{1/3} \quad \text{eqn. 5-2}$$

R_c , the radius of curvature, is the visible radius, rather than r_b . Such a drop is depicted in Figure 5.1 (b).

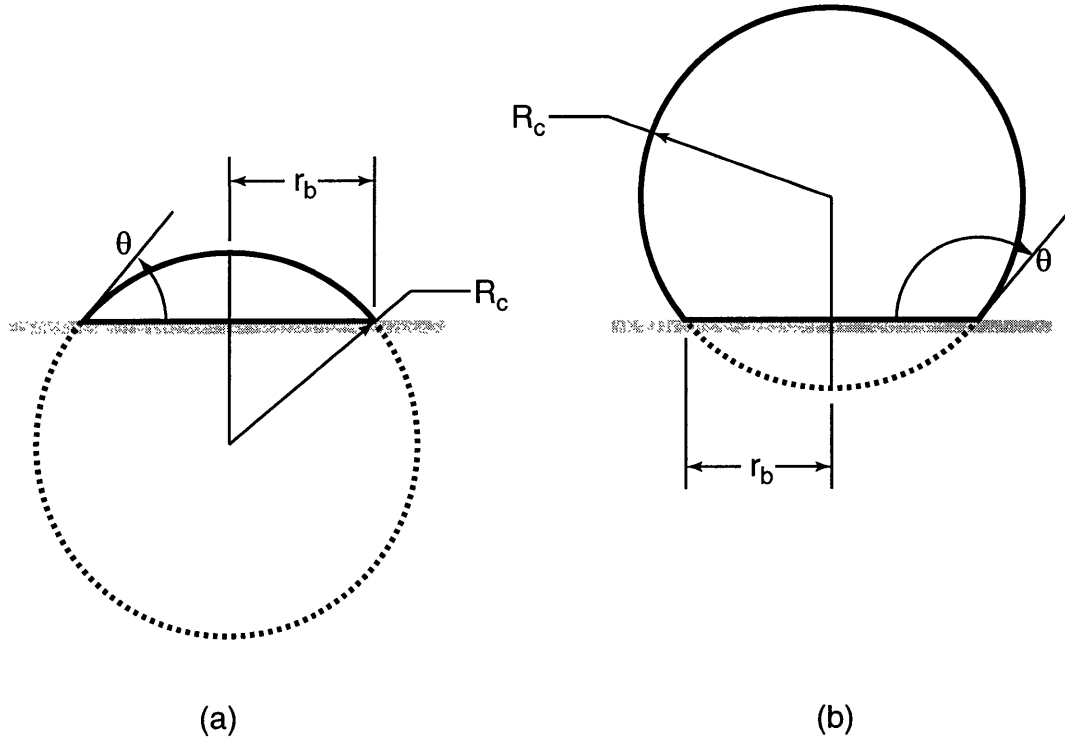


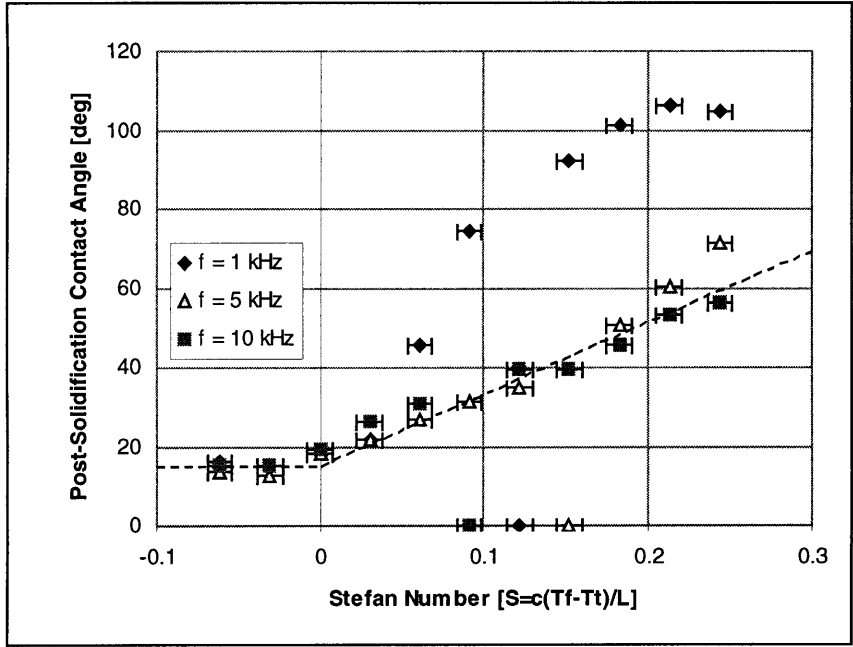
Figure 5.1 Profile views of solidified droplets, where (a) $\theta < 90^\circ$ and (b) $\theta > 90^\circ$.

NONEQUILIBRIUM POST-SOLIDIFICATION ANGLE OF WAX ON SILICON

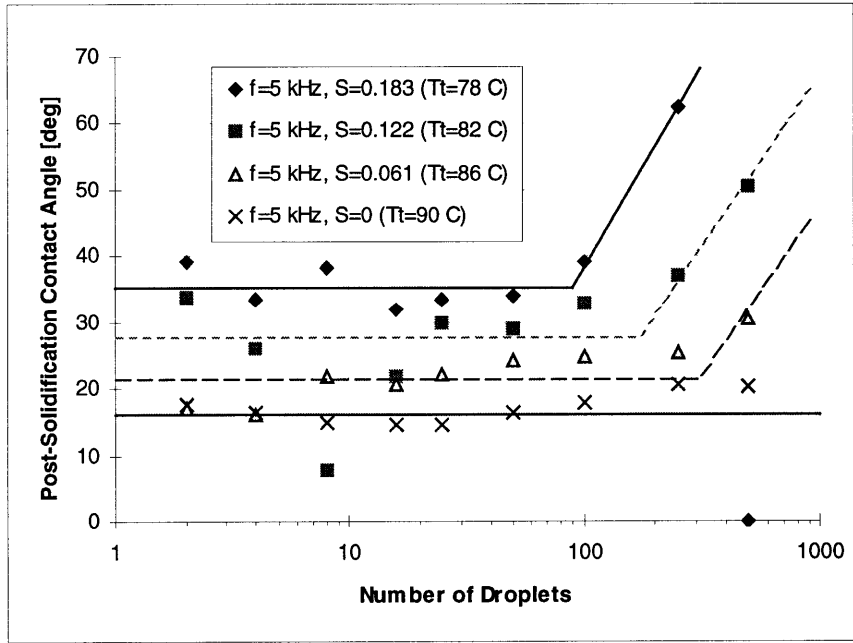
We studied the contact angle of a macrodrop formed by depositing a stream of droplets from the ink-jet head onto the target. Based on results from Schiaffino and Sonin (1997a), we varied three parameters to determine their effect on the equilibrium contact angle: the target temperature (T_t), the frequency of deposition (f), and the number of droplets deposited (N). The target temperature was controlled with a heater system, while the frequency and number of droplets were both controlled with a digital pulse generator. Measurement of each macrodrop was done after deposition and solidification; the contact angle was determined by eqn. 5-1 or eqn. 5-2, as appropriate.

We ran an experiment to determine the effect of these three parameters by holding two of the three constant while varying the other over a preset range. In all experiments, the nozzle temperature was held constant at approximately 120°C , 29°C above microcrystalline wax's (Reed 6882) melting point of 91°C . The results follow the behavior observed by Schiaffino and Sonin. When the target temperature decreases (increasing Stefan number), the post-solidification contact angle increases (shown in Figure 5.2 (a)). Similarly, when the number of droplets increases, as illustrated in Figure 5.2 (b), the post-solidification contact angle, θ_∞ , is nearly constant at a value θ_* until a threshold value for N , N^* , is reached. N^* itself varies depending on the target temperature, ranging from approximately 80 at $S = 0.183$ ($T_t = 78^\circ\text{C}$) to ~

300 at $S = 0.061$ ($T_i = 86^\circ\text{C}$). This sharp dependence on Stefan number is probably due to the high thermal conductivity of the silicon target.



(a)



(b)

Figure 5.2 Post-solidification contact angle (in degrees) versus (a) Stefan number [$S = c_p(T_f - T_i)/L$] and versus (b) number of droplets. Microcrystalline wax (Reed 6882) at $\sim 115^\circ\text{C}$ on monocrystalline silicon.

125 droplets were deposited at varying frequencies and target temperatures to make a macrodrop. Schiaffino and Sonin discovered that the plot of θ_∞ versus S does not depend on the deposition frequency, but deposition on a silicon substrate seems to contradict that result, as seen in Figure 5.2 (a). The silicon target's thermal conductivity is so large that the contact line arrests due to solidification. At smaller deposition frequencies, the contact line arrests early in the deposition, especially at higher Stefan numbers. Thus, the large apparent contact angle is actually caused by drop swelling above the frozen contact line.

Based upon the results presented in Figure 5.2 (b), we fitted a line through the region $N < N^*$ for each value of the Stefan number. The fitted θ^* values were plotted against S in Figure 5.3. For these four temperatures, the data exhibit a clear linear trend, which is similar to the behavior described by Schiaffino and Sonin.

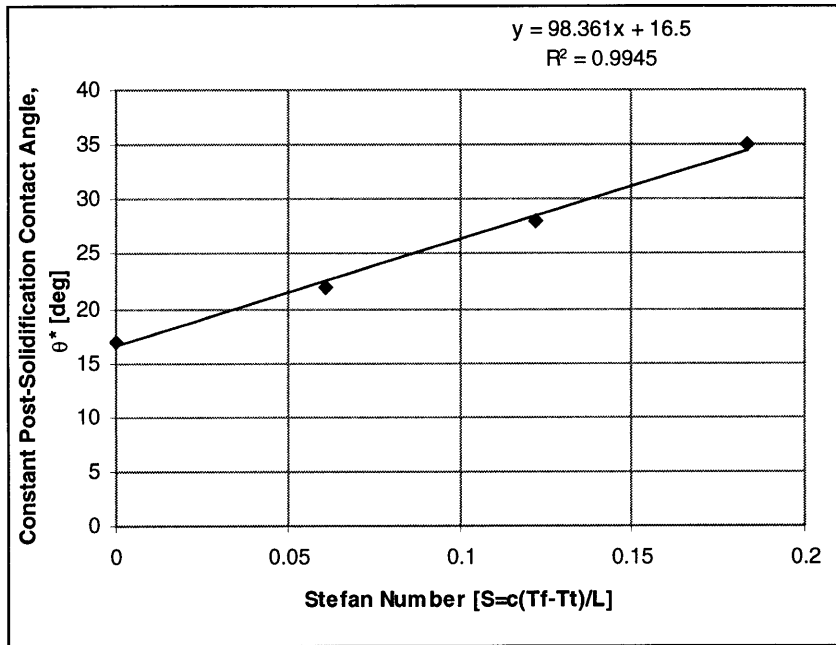


Figure 5.3 Constant post-solidification contact angle (in degrees) versus Stefan number. Microcrystalline wax (Reed 6882) at $\sim 115^\circ\text{C}$ on monocrystalline silicon.

When the contact angle was plotted against the total deposition time, $t_d \equiv N/f$, the frequency-controlled and number-controlled experimental results appear to coincide. This behavior is shown for $T_t = 78^\circ\text{C}$ in Figure 5.4; other target temperatures appear similar. The series labeled “f ctrl” are the frequency-controlled data, where the number of droplets was held constant at 125 droplets while the frequency was varied between 0.5 and 25 kHz. Similarly, the series labeled “N ctrl” are the number-controlled data; the frequency was held constant at 5 kHz while between 2 and 500 droplets were deposited.

Figure 5.4 suggests that the contact line arrests on a silicon target after a certain time in the deposition, independent of deposition frequency or number. After a certain time has elapsed, and a given amount of wax has been deposited on the target, additional droplets will not be able to keep the contact line

molten. For the two points located at $t_d = 0.05$ sec, the filled point represents a macrodrop formed by 125 droplets deposited at 2.5 kHz, while the hollow point is 250 droplets deposited at 5 kHz. Although the hollow point represents twice as much volume as the filled point, the contact angles are virtually the same. The heat transfer from the wax is probably not limited by the time it takes for thermal information to travel across the thickness of the silicon target. This characteristic time, t_{char} , is defined by

$$t_{char} = \frac{l^2}{\alpha} \tag{eqn. 5-3}$$

where l is a characteristic length (in this case, the wafer thickness) and α is the thermal diffusivity of the silicon. For a wafer thickness of approximately 0.6 mm, and a thermal diffusivity of $8.92 \times 10^{-5} \text{ m}^2/\text{s}$, the characteristic time is approximately 4 msec. From Figure 5.4, we see that the contact line arrests when the deposition takes longer than 20 to 40 msec for the given target temperature of 78°C. Perhaps since the silicon target is much more thermally massive and conductive than the wax, the heat transfer from the wax on the target is not limited by the amount of wax already on the target.

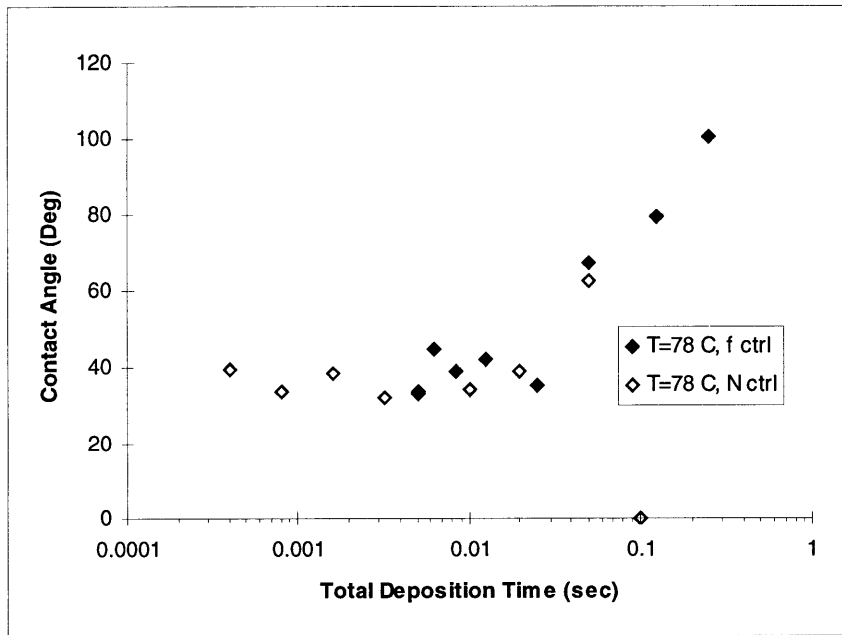


Figure 5.4 Contact angle (in degrees) versus total deposition time (in seconds) for a target temperature of 78°C. Microcrystalline wax (Reed 6882) at ~115°C on silicon.

At very large contact angles, (i.e. $\theta_\infty > 115^\circ$), the shape of the frozen macrodrop deviates significantly from a spherical cap shape, becoming almost an “ice-cream cone”, with a frustum base and hemispherical top. Thus, it is nearly impossible to accurately predict the contact angle from eqn. 5–2. The

post-solidification contact angle before the threshold N^* , θ_* , appears to be a function of Stefan number; for a given S , any $\theta_o > \theta_*(S)$ results from macrodrop swelling caused by deposition continuing after the contact line froze.

The total deposition time, t_d , proved to be an unreliable parameter. In a separate experiment, even at moderate target subcooling, the data exhibit tremendous scatter, as shown in Figure 5.5. Several combinations of frequency and number were used for each value of t_d . The scatter is partially attributable to measurement uncertainty, as the data for r_b were scaled directly from a video monitor. This monitor exhibited severe distortion (e.g., circles near the edges would be stretched out into ellipses). In addition, at very short deposition times, the contact line was not circular. Within a stream, individual droplets are not precisely located on the target, due to convection currents affecting their trajectory. Macrodrops made of a few droplets (i.e. at small t_d) have ragged shapes because the scatter in the droplets' impact position is comparable to the final contact line radius. Dynamic macrodrop collapse could have also contributed to data scatter. This phenomenon was noticed by Gao (1994), Schiaffino (1996), and Torresola (1998); after apparently freezing, the contact line suddenly jumps to a new position. It generally causes macrodrops whose contact angles would exceed 90° to jump to smaller angles. Physical surface features may also have affected the data. Although each silicon target was cleaned with alcohol before deposition, surface scratches and/or pits may have affected the spreading.

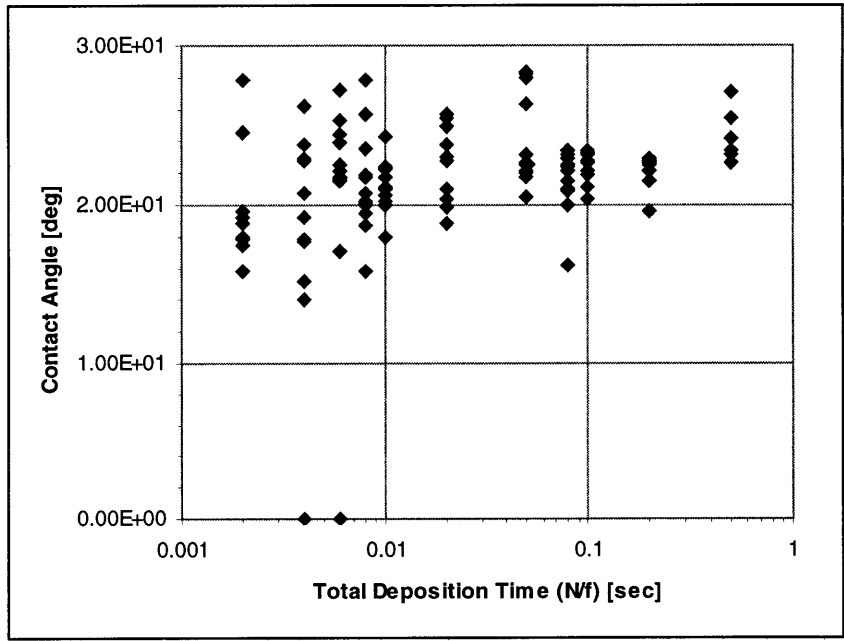


Figure 5.5 Contact angle (in degrees) versus total deposition time (in seconds) for a target temperature of 85°C . Microcrystalline wax (Reed 6882) at $\sim 115^\circ\text{C}$ on silicon.

APPARENT DYNAMIC CONTACT ANGLE

We later captured the spreading process of microcrystalline wax on a smooth silicon surface with a video camera, which captured sixty frames per second. The contact line radius was measured in each frame until the contact line froze. We modeled spreading on an isothermal surface as a spherical cap growing at a constant contact angle. Given the frequency of deposition, f , the number of droplets deposited at any time, t , into the deposition is $N = t \cdot f$. Thus, we can substitute for N in eqn. 5-1 to get the contact line radius as a function of time, deposition frequency, and contact angle:

$$\frac{r_b}{a} = \left(\frac{4tf \cdot \sin^3 \theta}{(1 - \cos \theta)^2 (2 + \cos \theta)} \right)^{1/3} \quad \text{eqn. 5-4}$$

With a constant contact angle equal to the appropriate θ_* , eqn. 5-4 reduces to a simple $1/3^{\text{rd}}$ power law; it is plotted in Figure 5.6 against data obtained from the video-captured frames. The data are taken from three separate experiments; “x sec data” is from an experiment whose total deposition time is equal to x. The data were sampled until the contact line appeared to freeze.

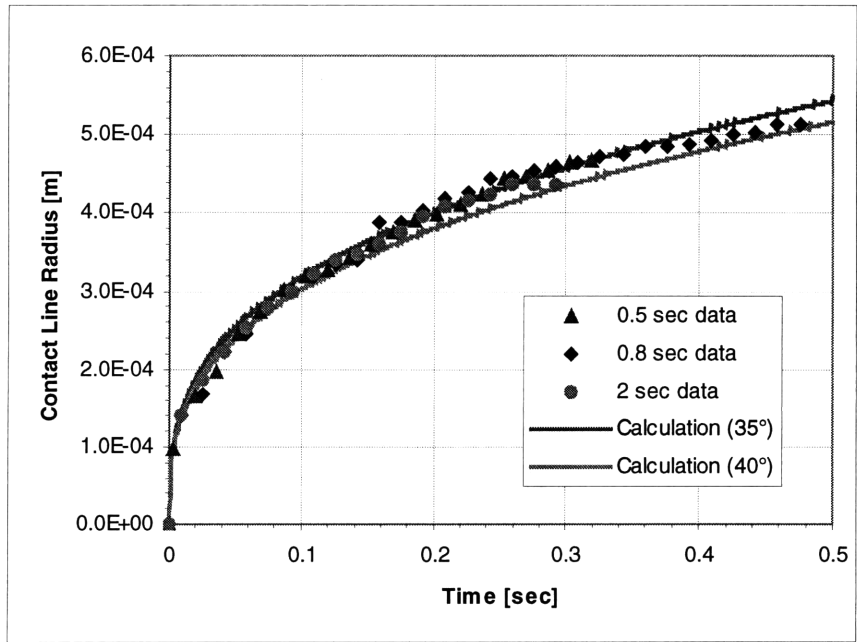


Figure 5.6 Contact line radius (in meters) versus time (in seconds), experiment and theory. Microcrystalline wax (Reed 6882) at $\sim 120^\circ\text{C}$ on silicon; $f=2.5\text{kHz}$ and $T_i=79^\circ\text{C}$.

Because the video acquisition was not synchronized with the droplet stream, we did not know the time position of the first frame showing droplets hitting the substrate. At a target temperature of 78°C , we

estimated that θ_* was 35° , according to Figure 5.2 (b). We thus assumed that the video-measured radius was reached at the same time that the constant $\theta = 35^\circ$ model reached the same radius. The remaining points were measured from successive frames, so the time step between each was $1/60^{\text{th}}$ of a second. We estimate the accuracy of radius measurements at $\pm 16 \mu\text{m}$.

Figure 5.4 suggests that the contact line arrests after $N^* = 80$ droplets ($t_d \sim 20$ msec) have been deposited at 5 kHz on an $S = 0.183$ ($T_i = 78^\circ\text{C}$) silicon target. In contrast, Figure 5.6 shows spreading continuing for $N > 800$ droplets ($t > 0.32$ sec) at 2.5 kHz on an $S = 0.168$ ($T_i = 79^\circ\text{C}$) silicon target. At the latter frequency, a single video frame of $1/60^{\text{th}}$ sec will capture the effects of adding approximately 42 droplets to the macrodrop. Thus, we would expect the contact line to arrest after two frames, but it somehow stays molten, as it appears to spread over a longer series of frames. The discrepancy in N^* is puzzling and unresolved; it may depend on the specific surface chemistry or thermal properties of the target used.

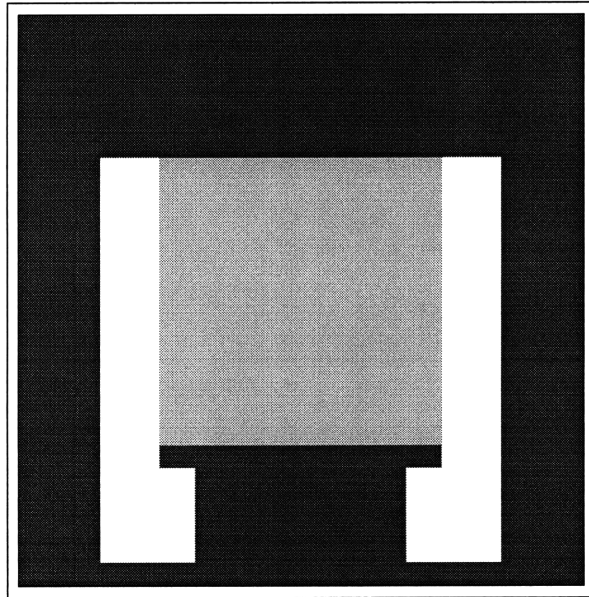
Except at the very beginning of the deposition, the data fit the theory remarkably well. Due to limited optical resolution, we are not able to determine the actual contact angle, so the spherical cap contact angle is an apparent contact angle. These data suggest that surface tension is remarkably successful at keeping the molten macrodrop in a spherical cap shape as it spreads.

CONCLUSIONS

We wanted to characterize the spreading of wax on silicon, to determine if the different thermal properties of silicon affected the spreading process. The data in general agree with the conclusions reached by Schiaffino and Sonin (1997a) – the post-solidification contact angle, θ_∞ , is controlled by the number of droplets, N , and the Stefan number, S , a nondimensional representation of the target subcooling. θ_∞ was constant, θ_* , for $N < N^*$, a threshold value which in turn depended on S . The silicon target's high conductivity made the value of N^* somewhat sensitive to the deposition frequency, f , which was not noted in Schiaffino and Sonin's work (1997a). While investigating the equilibrium contact angle of wax on silicon, we discovered that its dependence on deposition frequency and number seems to collapse upon a single curve. When the contact angle was plotted against the total deposition time, defined as the number of droplets divided by the frequency, the data agreed closely. However, when we investigated this pseudovisible more thoroughly, we discovered that the spherical cap model could not describe the shape of certain macrodrops formed under extreme conditions (i.e. very short or long t_d , large S , etc.). Video measurements of a spreading macrodrop were compared to the size of a spherical cap growing at a constant contact angle. The data and theory in this case closely agreed, despite our macrodrop's contact line remaining molten more than ten times as long as predicted.

Chapter 6 GROOVED SILICON DEPOSITION

We were not sure what effect micron-sized obstacles would have on the motion of a spreading droplet. Professor Qiu provided us with micropatterned silicon chips, shown in Figure 6.1 (a). The middle portion of the chip is grooved with square-edged trenches; each trench is two microns wide and half a micron deep. The trenches are spaced four microns apart, center-to-center, so that the profile looks like a periodic square wave. This region and the profile pattern are shown in Figure 6.1 (b). The pattern sizes are of the same scale as our finished sensor chips; as stated in Chapter 2, the sensors stand approximately half a micron above the chip surface, and the sensor circuit traces are approximately ten microns wide.



(a)

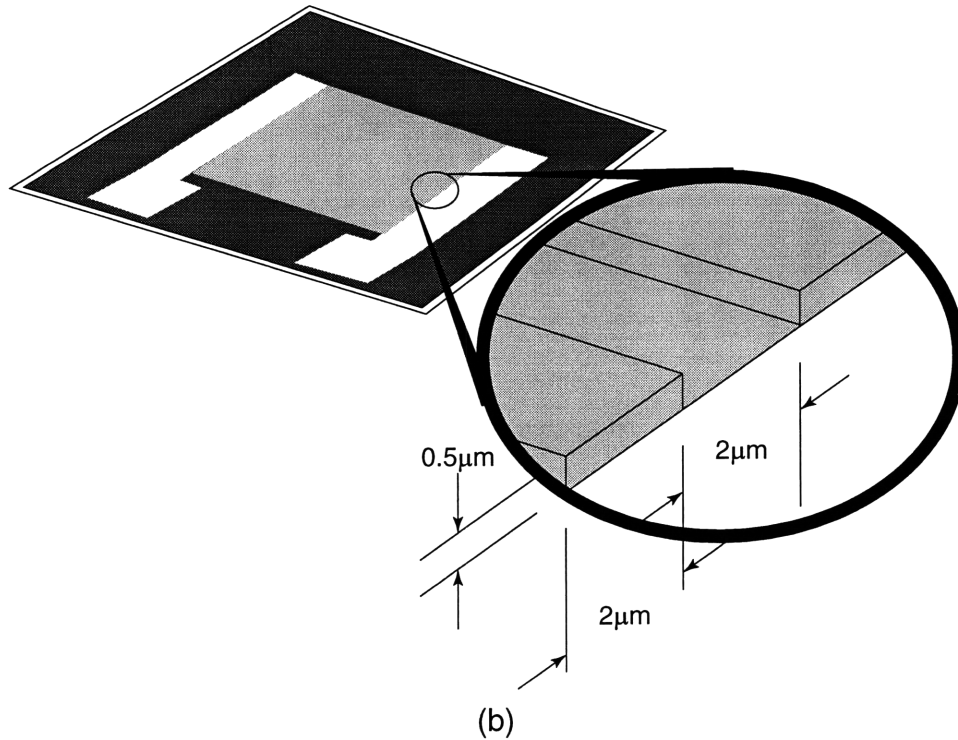
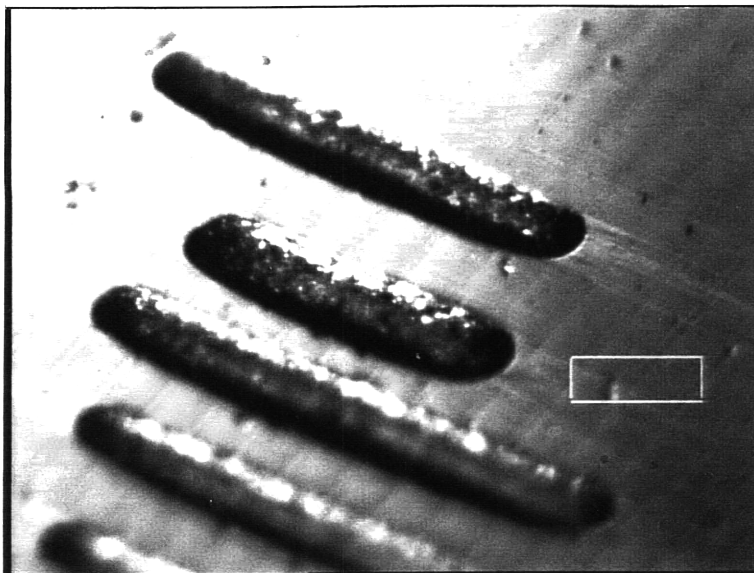


Figure 6.1 Schematics of the (a) top part and (b) cross-section close-up of the grooved silicon chips.

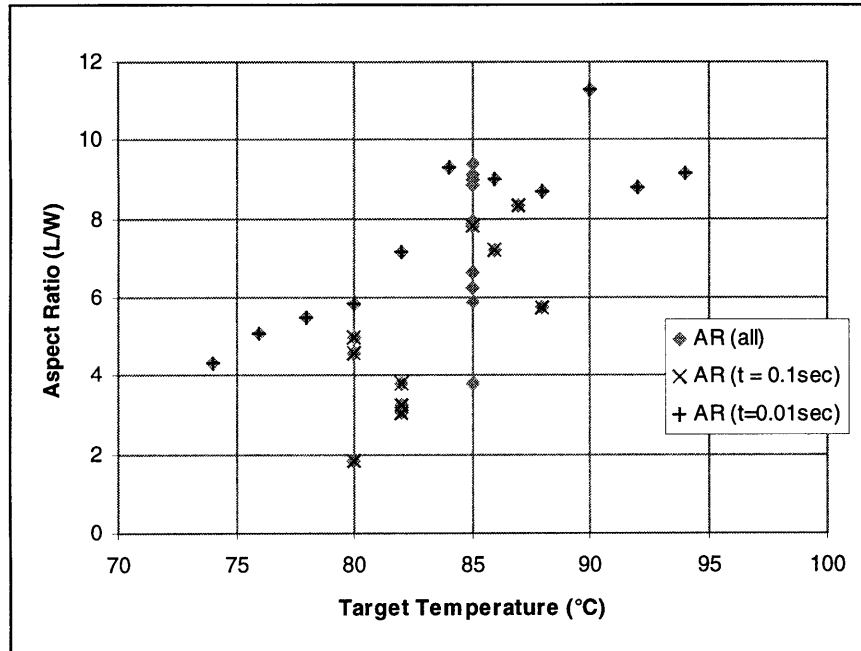
EFFECT ON SPREADING

We ran several experiments to determine the equilibrium contact angle of microcrystalline wax (Reed 6882) on these patterned silicon chips. We used the adapted ink-jet head to deposit microcrystalline wax on the patterns. In addition to the effect of the silicon on the thermal aspects of contact line arrest, the regular patterns presented mechanical obstacles to contact line motion. Just as in Chapter 5, we varied the target temperature, number of droplets, and deposition frequency. Although the macrodrops spread as predicted (we had forecast that the microstructure would affect the spreading), the shapes produced defy generalization. While macrodrops deposited on unpatterned silicon generally take the form of spherical caps, macrodrops on grooved silicon take on approximately cylindrical cap shapes shown in Figure 6.2. The long sides of the macrodrops are straight and follow the grooves, the shape being similar to a Quonset hut with hemispherical end caps and an “arched” back. Even the end-cap shape is not consistent; some macrodrops have rounded ends, other have squared-off ends.

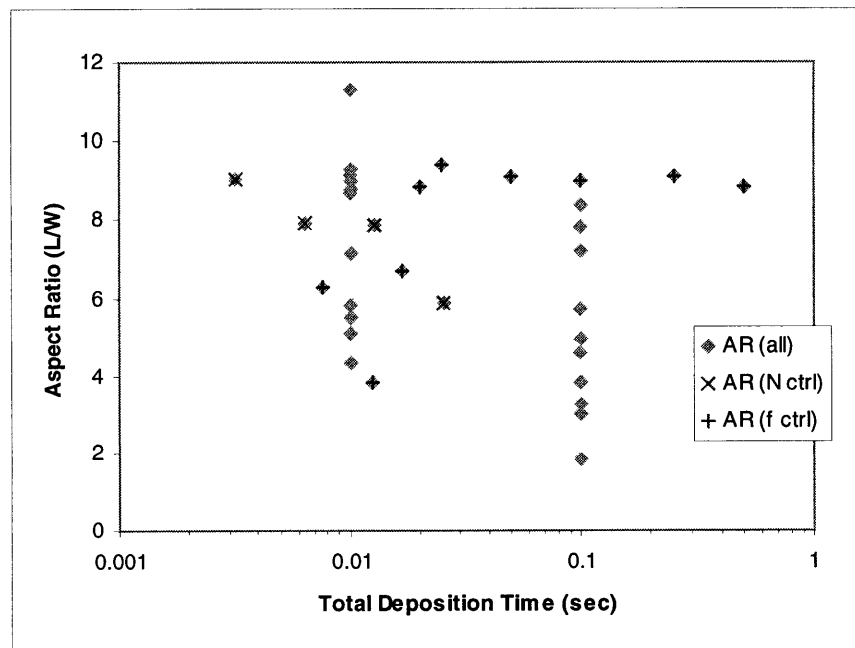


**Figure 6.2 Typical microcrystalline wax macrodrops deposited on patterned silicon.
Rectangle shown is 1/3 mm long.**

The aspect ratio, defined here as the length divided by the width of a macrodrop, does not seem to follow a clear trend. As shown in Figure 6.3, the data exhibit tremendous scatter when the aspect ratio is plotted against both (a) target temperature and (b) total deposition time. We expect that at lower temperatures, the aspect ratio decreases because the contact line freezes earlier. In general, our data bear this hypothesis out. However, the data exhibit tremendous scatter at any fixed temperature; for example, the aspect ratios at a target temperature of 80°C range from two to six. The data, in fact, seem to suggest that the mechanical features of the target affect the spreading of macrodrops even more than number of microdrops and deposition frequency..



(a)



(b)

Figure 6.3 Aspect ratio (length/width) of macrodrops versus (a) target temperature (in °C) and (b) total deposition time, N/f (in seconds). Microcrystalline wax (Reed 6882) on silicon.

One unusual effect of deposition on the grooved chip was the separation of components. Microcrystalline wax (Reed 6882) is an alloy of different materials. As shown in Figure 6.4, at least one

component of the wax, which presumably has a lower melting point, separates and spreads far ahead of the contact line prior to arrest. This component's spreading may be aided by the capillary effects related to the groove size.

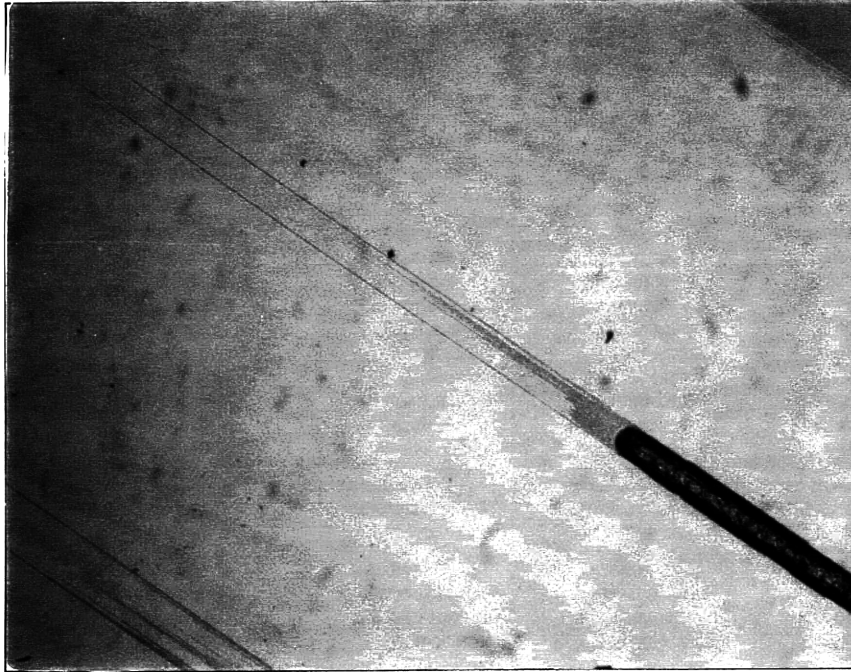


Figure 6.4 Close-up view of a macrodrop on a grooved chip, showing a component spreading ahead of the contact line. 16 drops at 5 kHz, target temperature of 85°C; microcrystalline wax (Reed 6882) on silicon.

CONCLUSIONS

A single obstacle would probably emulate the actual microsensor chips better than this series of regular grooves. Such an obstacle would better simulate the actual geometry of the chip. Although the tests revealed no general trends (e.g., aspect ratio versus target temperature or total deposition time), they showed that microstructures as low as 0.5 μm above a surface dominate the spreading of a macrodrop. Perhaps a larger macrodrop, or one that is formed by the pendant drop apparatus, would not exhibit such strongly anisotropic spreading. At a radius of 25 μm each, individual droplets are strongly influenced by micron-sized obstacles, while larger droplets may not be.

Chapter 7 ONE-DIMENSIONAL HEAT TRANSFER MODEL

Since silicon has different physical and thermal properties than the microcrystalline wax we used (Reed 6882), we wanted to model the heat transfer when depositing a melt on a target of different material. In the absence of conduction in the target along the interface with the molten wax, a one-dimensional solution is adequate. Silicon actually has a high thermal conductivity relative to wax, so this assumption breaks down in regions close to the moving contact line. However, far from the contact line, a one-dimensional model can predict the temperature history of the sensors.

Previous analyses (Gao (1994), Schiaffino (1996)) have assumed that microcrystalline wax has a distinct melting point, like a pure substance. Recent experiments by Torresola (1998) demonstrated that the wax actually releases latent heat when solidifying over a temperature range. This wax is a mixture of different materials, and so behaves more as an alloy, with the solid-liquid phase transition occurring over a range of temperatures. Torresola modeled this behavior as transient solidification in a semi-infinite material with a suddenly cooled boundary; the material has a variable specific heat in this melting range. The front's position relative to the cooled boundary is a function of material properties, initial temperatures (melt and target), the melting range temperatures, and the time after contact. In the present analysis, the specific heat is constant in the melting range, while Torresola models the specific heat as a linear function of temperature in the same range. The differences between the two models are shown in Figure 7.1. Note that the area contained underneath the curve in the melting range, which is the latent heat associated with the phase transition, is identical in both cases.

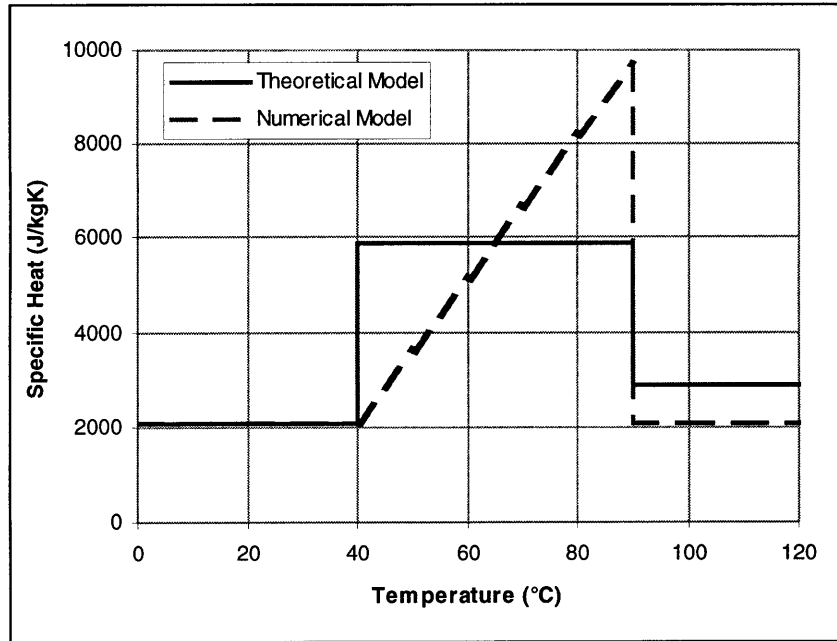


Figure 7.1 Alternative models of variable specific heat with melting range $\Delta T = 50^\circ\text{C}$.

Carslaw and Jaeger (1959) analyze several one-dimensional solidification processes. They solve the heat transfer between a melt and a target of different materials suddenly coming into contact with each other (§11.2-IV), but their melt is a pure substance, with a distinct melting point. Thus, we cannot directly use their solution. They do mention two additional phenomena encountered when modeling the solidification of impure materials: phase transition over a temperature range and density differences between solid and liquid states. Although they present solutions for each phenomenon, they do not integrate the effects.

ANALYSIS

The system being analyzed is shown in Figure 7.2. A molten liquid, initially at temperature T_{lo} , is brought into contact at $x=0$ with a target of a different material, initially at T_{to} . Solidification takes place over a range of temperatures, starting when the temperature reaches T_{f2} and finishing at T_{f1} (i.e. the melting range lies between T_{f1} at the low end and T_{f2} at the high). Each “zone” may have distinct thermal and physical properties. We will denote all zonal properties with a subscript corresponding to the first letter of each zone, e.g. ρ_l , k_l , c_l , and α_l are, respectively, the density, thermal conductivity, specific heat, and thermal diffusivity of the liquid zone, respectively.

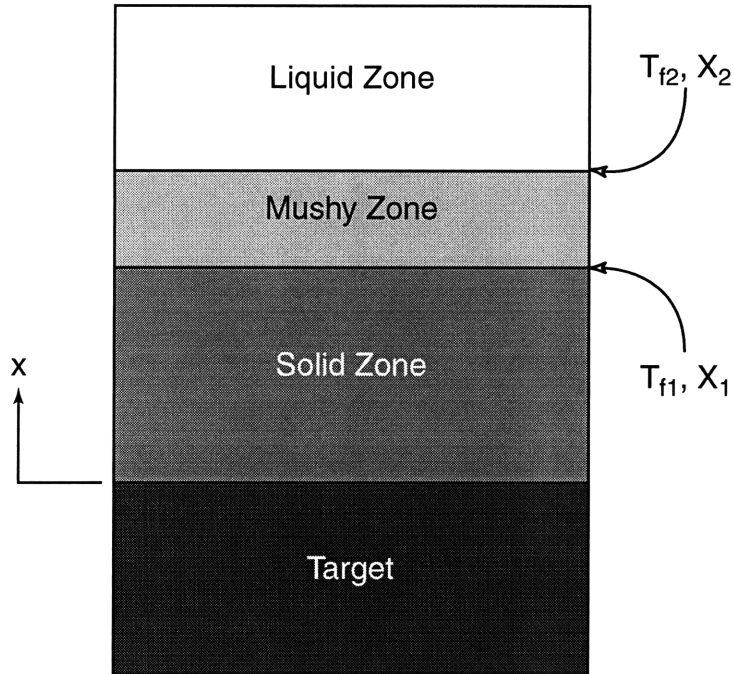


Figure 7.2 One-dimensional solidification of a material with a phase transition region on a target of a different material.

Carslaw and Jaeger recommend using an “enhanced” specific heat, c_e , in the phase transition temperature range (corresponding to our “mushy zone”). For a material with a phase transition beginning at T_{f1} and ending at T_{f2} , c_e is given by

$$c_e = c + \frac{L}{T_{f2} - T_{f1}} \quad \text{eqn. 7-1}$$

where L is the latent heat released in the phase change and c is the specific heat of the material before undergoing the phase transition (in the case of solidification, c is the specific heat of the molten material). In other words, c_e is our c_m .

When the density of the melt is not equal to the density of the solidified material, Carslaw and Jaeger demonstrate that an additional velocity, u_x , is imparted to the solidification interface. As shown in Figure 7.3, when the solidification front advances a distance dX , a mass of solid is formed from an equivalent mass of liquid:

$$\rho_{sol} \cdot dX = \rho_{liq} \cdot dh \quad \text{eqn. 7-2}$$

where the two distances, dh and dX , are not equal unless the two densities, ρ_{sol} and ρ_{liq} , are equal.

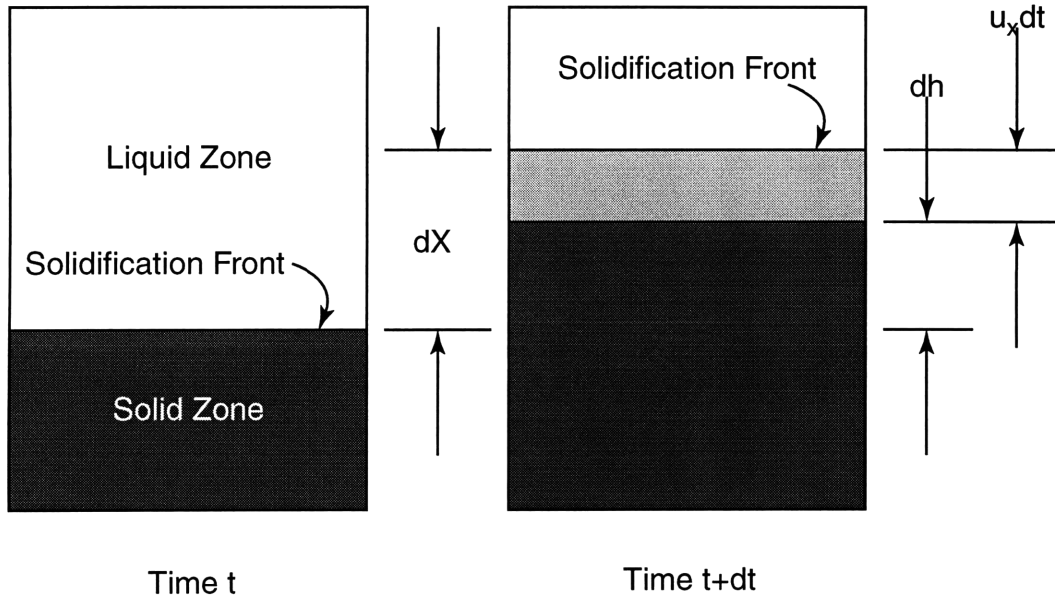


Figure 7.3 Motion of solidification front at temperature T_f (pure substance).

According to Figure 7.3, the disparity in densities imparts an additional velocity, u_x , to the solidification front, where

$$dh + u_x \cdot dt = dX \quad \text{eqn. 7-3}$$

Plugging eqn. 7-3 into eqn. 7-2 and solving for the velocity yields

$$u_x = \left(1 - \frac{\rho_{sol}}{\rho_{liq}} \right) \cdot \frac{dX}{dt} \quad \text{eqn. 7-4}$$

Referring back to Figure 7.2, the governing equations of heat transfer in each region, from target to liquid zone, are, respectively

$$\frac{\partial^2 T_l}{\partial x^2} - \frac{1}{\alpha_l} \cdot \frac{\partial T_l}{\partial t} = 0 \quad \text{eqn. 7-5}$$

$$\frac{\partial^2 T_s}{\partial x^2} - \frac{1}{\alpha_s} \cdot \frac{\partial T_s}{\partial t} = 0 \quad \text{eqn. 7-6}$$

$$\frac{\partial^2 T_m}{\partial x^2} - \frac{u_{x1}}{\alpha_m} \cdot \frac{\partial T_m}{\partial x} - \frac{1}{\alpha_m} \cdot \frac{\partial T_m}{\partial t} = 0 \quad \text{eqn. 7-7}$$

$$\frac{\partial^2 T_l}{\partial x^2} - \frac{u_{x2}}{\alpha_l} \cdot \frac{\partial T_l}{\partial x} - \frac{1}{\alpha_l} \cdot \frac{\partial T_l}{\partial t} = 0 \quad \text{eqn. 7-8}$$

Note that the governing equations for the liquid and mushy zones, eqn. 7-8 and eqn. 7-7, respectively, include convective terms based on density-change-induced velocities, defined in eqn. 7-4. The induced velocities for the mushy and liquid zones are, respectively,

$$u_{x1} = \left(1 - \frac{\rho_s}{\rho_m} \right) \cdot \frac{dX_1}{dt} \quad \text{eqn. 7-9}$$

$$u_{x2} = u_{x1} + \left(1 - \frac{\rho_m}{\rho_l} \right) \cdot \frac{dX_2}{dt} \quad \text{eqn. 7-10}$$

Assuming the mushy zone is incompressible, the induced velocity at the solid-mushy interface will be transmitted through the mushy zone, so u_{x2} includes u_{x1} .

The boundary conditions generally consist of temperature and heat flux matching at each zone interface. At the target-solid zone interface,

$$x = 0 \Rightarrow T_t = T_s \quad \text{eqn. 7-11}$$

$$x = 0 \Rightarrow k_t \cdot \frac{\partial T_t}{\partial x} = k_s \cdot \frac{\partial T_s}{\partial x} \quad \text{eqn. 7-12}$$

At the solid-mushy zone interface,

$$x = X_1 \Rightarrow T_s = T_m = T_{f1} \quad \text{eqn. 7-13}$$

$$x = X_1 \Rightarrow k_s \cdot \frac{\partial T_s}{\partial x} = k_m \cdot \frac{\partial T_m}{\partial x} \quad \text{eqn. 7-14}$$

Finally, at the mushy-liquid zone interface,

$$x = X_2 \Rightarrow T_m = T_l = T_{f2} \quad \text{eqn. 7-15}$$

$$x = X_2 \Rightarrow k_m \cdot \frac{\partial T_m}{\partial x} = k_l \cdot \frac{\partial T_l}{\partial x} \quad \text{eqn. 7-16}$$

Since this is a problem of two semi-infinite bodies brought into sudden contact, far from the interfaces, the temperatures remain constant, giving us our final two boundary conditions

$$x \rightarrow -\infty \Rightarrow T_l \rightarrow T_{lo} \quad \text{eqn. 7-17}$$

$$x \rightarrow +\infty \Rightarrow T_l \rightarrow T_{lo} \quad \text{eqn. 7-18}$$

The initial conditions ensure that temperatures are homogeneous in the melt and target and that no phase-change fronts have formed.

$$t = 0 \Rightarrow T_t = T \quad \text{eqn. 7-19}$$

$$t = 0 \Rightarrow T_t = T_{to} \quad \text{eqn. 7-20}$$

$$t = 0 \Rightarrow X_1 = 0 \quad \text{eqn. 7-21}$$

$$t = 0 \Rightarrow X_2 = 0 \quad \text{eqn. 7-22}$$

We reformulate the governing equations in terms of a similarity variable, η , which incorporates time and space

$$\eta_t = \frac{x}{2\sqrt{\alpha_t t}} \quad \text{eqn. 7-23}$$

$$\eta_s = \frac{x}{2\sqrt{\alpha_s t}} \quad \text{eqn. 7-24}$$

$$\eta_m = \frac{x}{2\sqrt{\alpha_m t}} \quad \text{eqn. 7-25}$$

$$\eta_l = \frac{x}{2\sqrt{\alpha_l t}} \quad \text{eqn. 7-26}$$

Once we make these substitutions, the governing equations (eqn. 7-5 through eqn. 7-8) transform from partial to ordinary differential equations in terms of the similarity variable.

$$\frac{d^2 T_t}{d\eta_t^2} + 2\eta_t \cdot \frac{dT_t}{d\eta_t} = 0 \quad \text{eqn. 7-27}$$

$$\frac{d^2 T_s}{d\eta_s^2} + 2\eta_s \cdot \frac{dT_s}{d\eta_s} = 0 \quad \text{eqn. 7-28}$$

$$\frac{d^2 T_m}{d\eta_m^2} + 2 \left(\eta_m - u_{x1} \sqrt{\frac{t}{\alpha_m}} \right) \cdot \frac{dT_m}{d\eta_m} = 0 \quad \text{eqn. 7-29}$$

$$\frac{d^2 T_l}{d\eta_l^2} + 2 \left(\eta_l - u_{x2} \sqrt{\frac{t}{\alpha_l}} \right) \cdot \frac{dT_l}{d\eta_l} = 0 \quad \text{eqn. 7-30}$$

Note that the far-field boundary conditions (eqn. 7-17 and eqn. 7-18) and the initial temperature conditions (eqn. 7-19 and eqn. 7-20) collapse onto each other with the similarity solution. However, both the liquid and mushy zones' governing equations (eqn. 7-29 and eqn. 7-30) still depend on the time and induced velocity. In order for these equations to be a true similarity solution, this would suggest that

$$2u_{x1} \sqrt{\frac{t}{\alpha_m}} = C_1 \quad \text{eqn. 7-31}$$

$$2u_{x2} \sqrt{\frac{t}{\alpha_l}} = C_2 \quad \text{eqn. 7-32}$$

where C_1 and C_2 are constants to be determined. Solving eqn. 7-31 for u_{x1} and substituting that result into eqn. 7-9 yields a simple differential equation for X_1 , which may be solved to yield

$$X_1 = \frac{C_1}{2} \cdot \left(1 - \frac{\rho_s}{\rho_m} \right) \cdot 2\sqrt{\alpha_m t} = 2\lambda_1 \sqrt{\alpha_m t} \quad \text{eqn. 7-33}$$

Similarly, it can be shown that the position of the second phase-change front is given by

$$X_2 = 2\lambda_2 \sqrt{\alpha_l t} \quad \text{eqn. 7-34}$$

In both equations, λ_1 and λ_2 are constants. When these expressions for X_1 and X_2 (eqn. 7-33 and eqn. 7-34) are inserted into the appropriate governing equations (eqn. 7-29 and eqn. 7-30), we obtain:

$$\frac{d^2 T_m}{d\eta_m^2} + 2 \left(\eta_m - \lambda_1 \left[1 - \frac{\rho_s}{\rho_m} \right] \right) \cdot \frac{dT_m}{d\eta_m} = 0 \quad \text{eqn. 7-35}$$

$$\frac{d^2 T_l}{d\eta_l^2} + 2 \left(\eta_l - \lambda_2 \left[1 - \frac{\rho_m}{\rho_l} \right] - \lambda_1 \left[1 - \frac{\rho_s}{\rho_m} \right] \sqrt{\frac{\alpha_m}{\alpha_l}} \right) \cdot \frac{dT_l}{d\eta_l} = 0 \quad \text{eqn. 7-36}$$

Once the governing equations (eqn. 7-27, eqn. 7-28, eqn. 7-35, and eqn. 7-36) have been solved, the far-field boundary/initial conditions (eqn. 7-17 through eqn. 7-22) may be applied and, with some algebraic manipulation, the solutions are

$$T_i = T_{i0} + A \cdot \left(1 + \operatorname{erf} \left[\frac{x}{2\sqrt{\alpha_i t}} \right] \right) \quad \text{eqn. 7-37}$$

$$T_s = C \cdot \operatorname{erf} \left(\frac{x}{2\sqrt{\alpha_s t}} \right) + D \quad \text{eqn. 7-38}$$

$$T_m = E \cdot \operatorname{erf} \left(\frac{x}{2\sqrt{\alpha_m t}} - \lambda_1 \left[1 - \frac{\rho_s}{\rho_m} \right] \right) + F \quad \text{eqn. 7-39}$$

$$T_l = T_{l0} - G \cdot \operatorname{erfc} \left(\frac{x}{2\sqrt{\alpha_l t}} - \lambda_2 \left[1 - \frac{\rho_m}{\rho_l} \right] - \lambda_1 \left[1 - \frac{\rho_s}{\rho_m} \right] \sqrt{\frac{\alpha_m}{\alpha_l}} \right) \quad \text{eqn. 7-40}$$

A , C , D , E , F and G are constants to be determined through the remaining boundary conditions (i.e. matching temperature and heat flux at each zone's interfaces). For algebraic convenience, we define

$$S_1 \equiv \left(\lambda_1 \frac{\rho_s}{\rho_m} \right)^2 \quad \text{eqn. 7-41}$$

$$S_2 \equiv \left(\lambda_2 \sqrt{\frac{\alpha_l}{\alpha_m}} - \lambda_1 \left[1 - \frac{\rho_s}{\rho_m} \right] \right)^2 \quad \text{eqn. 7-42}$$

$$S_3 \equiv \left(\lambda_1 \sqrt{\frac{\alpha_m}{\alpha_s}} \right)^2 \quad \text{eqn. 7-43}$$

$$S_4 \equiv \left(\lambda_2 \frac{\rho_m}{\rho_l} - \lambda_1 \left[1 - \frac{\rho_s}{\rho_m} \right] \sqrt{\frac{\alpha_m}{\alpha_l}} \right)^2 \quad \text{eqn. 7-44}$$

By applying the boundary conditions at the target-solid zone interface (eqn. 7-11 and eqn. 7-12) to the target and solid zone solutions (eqn. 7-37 and eqn. 7-38), we can solve for D and C in terms of A .

$$D = A + T_{to} \quad \text{eqn. 7-45}$$

$$C = A \cdot \frac{k_t}{k_s} \sqrt{\frac{\alpha_s}{\alpha_t}} \quad \text{eqn. 7-46}$$

Similarly, we can apply the boundary conditions at $x=X_1$ (eqn. 7-13 and eqn. 7-14) to the solid and mushy zone solutions (eqn. 7-38 and eqn. 7-39) to solve for E and F in terms of A , λ_1 , and λ_2 .

$$E = A \cdot \frac{k_t}{k_m} \sqrt{\frac{\alpha_m}{\alpha_t}} \cdot e^{S_1 - S_3} \quad \text{eqn. 7-47}$$

$$F = T_{f1} - A \cdot \frac{k_t}{k_m} \sqrt{\frac{\alpha_m}{\alpha_t}} \cdot e^{S_1 - S_3} \cdot \text{erf}(\sqrt{S_1}) \quad \text{eqn. 7-48}$$

Since the temperature at the mushy-liquid zone interface is fixed (by the boundary condition in eqn. 7-15), we can set eqn. 7-40 equal to T_{f2} at X_2 and solve for G in terms of λ_1 and λ_2 .

$$G = \frac{T_{lo} - T_{f2}}{\text{erfc}(\sqrt{S_4})} \quad \text{eqn. 7-49}$$

We can substitute eqn. 7-45 and eqn. 7-46 for D and C into eqn. 7-38 to find the solid zone temperature. After we set this expression equal to T_{f1} at X_1 (via the boundary condition at the solid-mushy zone interface, eqn. 7-13), we obtain an expression for A in terms of λ_1 .

$$A = \frac{T_{f1} - T_{to}}{1 + \frac{k_t}{k_s} \sqrt{\frac{\alpha_s}{\alpha_t}} \operatorname{erf}(\sqrt{S_3})} \quad \text{eqn. 7-50}$$

Similarly, we can substitute eqn. 7-47 and eqn. 7-48 for E and F into eqn. 7-39 to find the mushy zone temperature. By setting this expression equal to T_{f2} at X_2 , (again, using the appropriate boundary condition, eqn. 7-15), we obtain another expression for A, this time in terms of λ_1 and λ_2 .

$$A = \frac{T_{f2} - T_{f1}}{\frac{k_t}{k_m} \sqrt{\frac{\alpha_m}{\alpha_t}} \cdot (\operatorname{erf}[\sqrt{S_2}] - \operatorname{erf}[\sqrt{S_1}]) \cdot e^{S_1 - S_3}} \quad \text{eqn. 7-51}$$

Finally, we can substitute the expressions for E, F, and G (eqn. 7-47, eqn. 7-48, and eqn. 7-49) into the mushy and liquid zone solutions (eqn. 7-39 and eqn. 7-40). These solutions can be put into the heat-flux matching boundary condition (eqn. 7-15) at X_2 to get a third expression for A in terms of λ_1 and λ_2 .

$$A = \frac{T_{lo} - T_{f2}}{\frac{k_t}{k_l} \sqrt{\frac{\alpha_l}{\alpha_t}} \cdot \operatorname{erfc}(\sqrt{S_4}) \cdot e^{S_1 + S_4 - S_2 - S_3}} \quad \text{eqn. 7-52}$$

Since we now have three unique expressions for A in terms of λ_1 and λ_2 , we can form two independent equations to solve for λ_1 and λ_2 . The resulting system of equations may be solved numerically for λ_1 and λ_2 ; A, C, D, E, F, and G will follow from these constants, giving the temperature distribution in each zone.

LIMITATIONS

This analysis is limited to one-dimensional heat transfer of two semi-infinite bodies coming into sudden contact with each other. Thus, it is not valid near the contact line, when the melt has just passed over the sensor(s). It also has a limited time range. It is only applicable for as long as the media involved may be considered semi-infinite, or approximately t_{char} , as defined in eqn. 5-3. In addition, modeling the specific heat as constant through the transition zone does not follow the experimental curve measured by Torresola very well.

The solution to this analysis depends on the thermal and physical properties of the four zones as well as the initial temperatures and the values of the transition temperatures. Thus, we could run this model with the same conditions used by Torresola in his numerical model; we should get the nearly the same values for the position of the phase-change fronts. With some modifications, this analysis can be applied to

a material with two phase-transition points, such as octacosane ($C_{28}H_{58}$), a member of the alkane family. Instead of matching heat fluxes at the interfaces, we need to account for latent heat release. However, even if the phase transitions take place at sharp points, other properties are temperature-dependent (most notably density), so this analysis really does not adequately model these materials.

Chapter 8 SENSOR CALIBRATION

From the outset, we knew that the sensors' resistances change with temperature, but did not know which direction it would take. In general, though, most semiconductor thermistors exhibit a negative temperature coefficient (NTC), where resistance decreases as temperature rises. For most semiconductors, the increasing mobility of electrons in excited states offsets increased lattice vibrations (as shown in Chapter 2). Thus, we needed to determine the magnitude of the resistance change with temperature.

We also wanted to determine how predictable and repeatable our temperature measurements were. To these ends, we developed a program ("My Calibration AI", described in Chapter 4) to take a series of resistance measurements from each sensor, average them, and return the standard deviation and average of those readings. We can then fit an appropriate curve to the data.

RESISTANCE-TEMPERATURE CHARACTERISTIC

Semiconducting thermistors are characterized by their temperature coefficient of resistance (TCR), γ_{st} , which is defined as

$$\gamma_{st} \equiv \frac{1}{R} \cdot \frac{dR}{dT} \quad \text{eqn. 8-1}$$

Here, R is the resistance of the thermistor and T is the temperature. In general, most commercially-available macroscopic thermistors depend exponentially on the inverse of temperature; they are called NTC thermistors

$$R_{NTC} = A \cdot e^{\frac{B}{T}} \quad \text{eqn. 8-2}$$

Here, A and B are constants dependent on the specific thermistor material and construction. Sachse (1975) details this theory; briefly, the number of charge carriers excited into higher (more conductive) energy states is proportional to the thermal energy of the material. This in turn is determined statistically, which involves an exponential dependence on the inverse of the temperature. Occasionally, higher-ordered terms of $1/T$ are used in the exponential argument to fit the data better.

In contrast, Kuźma (1994) describes thermistors whose resistances directly depend exponentially on temperature:

$$R_{NTC_{exp}T} = A' \cdot e^{BT} \quad \text{eqn. 8-3}$$

Following his convention, these thermistors are known as NTCexpT thermistors, to differentiate them from regular NTC thermistors. Note that the temperature coefficient of resistance is constant for NTCexpT thermistors in the exponential regime, while NTC thermistors' TCR depends on the temperature. According to eqn. 8-1,

$$\gamma_{NTC} = -\frac{B}{T^2} \quad \text{eqn. 8-4}$$

$$\gamma_{NTC_{exp}T} = B' \quad \text{eqn. 8-5}$$

NTCexpT thermistors operate in this exponential behavior regime for a limited range of temperatures. According to Kuźma, this exponential behavior regime lasts until a solid phase-transition is reached in the thermistor. Our sensors operate in the NTCexpT regime for our range of interest (approximately 30-120°C).

The “Grab Save Analyze” program, from Chapter 4, can fit temperature-resistance calibration data to the NTC or NTCexpT curves. When the NTC correlation is selected, the next-to-last row (i.e. the row immediately after the third row of separator zeroes) contains *A* and the last row contains *B*, as defined in eqn. 8-2. Similarly, in the NTCexpT case, the next-to-last row contains *A'* and the last row contains *B'* as the terms are defined in eqn. 8-3.

Sensor resistances are plotted versus several temperatures in Figure 8.1. The data shown are from a single array. When the chip was brought up to a given temperature by a heater-and-controller system, fifty readings from each sensor were taken and averaged. In Figure 8.1, note that at each temperature, each sensor has a unique resistance. The spread between the maximum and minimum resistance among all sensors at any given temperature is larger at lower temperatures (close to 30°C) than at higher temperatures (above 100°C). This spread arises from manufacturing tolerances in both the sensor chip and the supporting circuitry box.

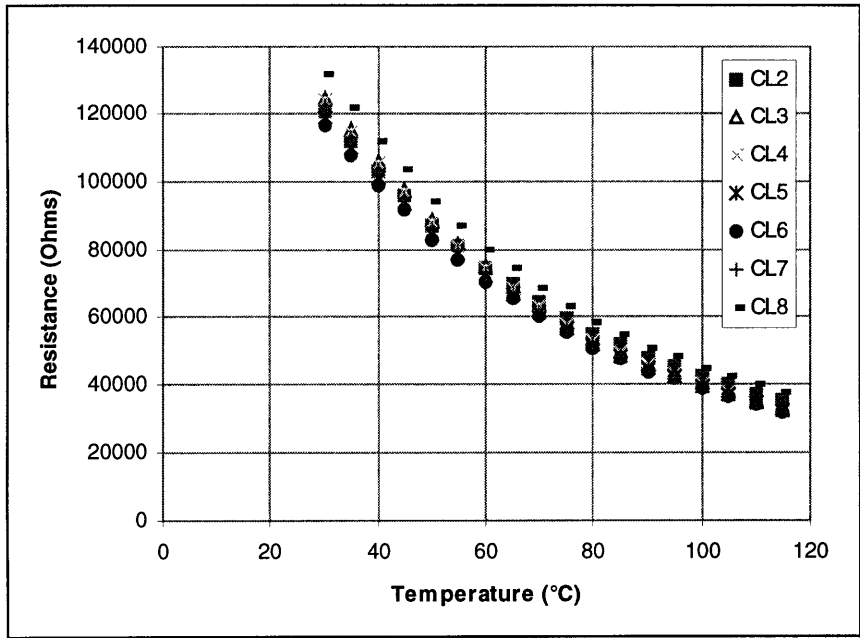


Figure 8.1 Sensor chip resistance versus temperature for chip number QU-11, coarse linear (CL) array, with NTC thermistor behavior illustrated.

For comparison, curves based on the NTC temperature response curve (eqn. 8-2) and that of the NTCexpT response (eqn. 8-3) are displayed on Figure 8.2, along with the actual data from coarse linear sensor number two (CL2). Both responses are fitted to the data with a least-squares algorithm. Clearly, our sensors behave as NTCexpT thermistors in this temperature regime. Our microsensors, made out of polycrystalline silicon, probably have a microstructure similar to that described by Kuźma.

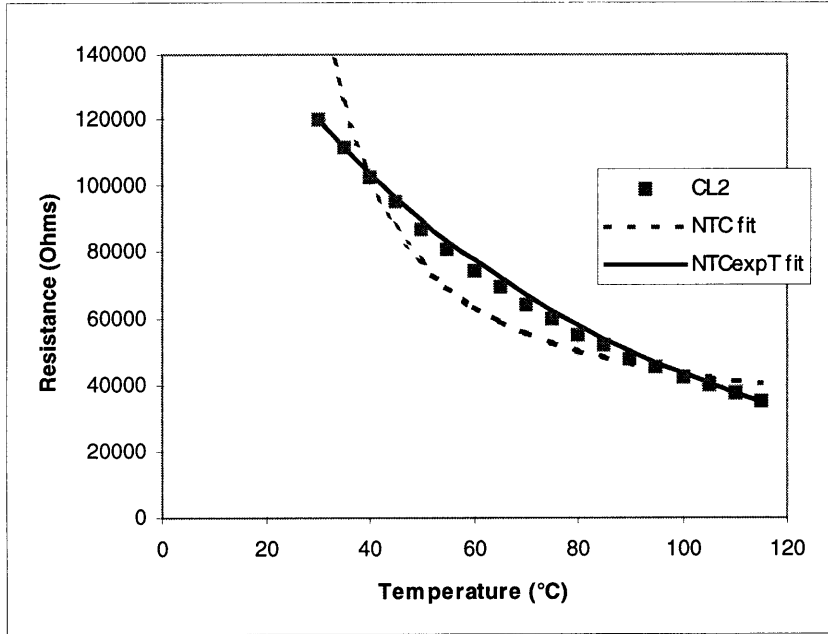


Figure 8.2 Temperature response of CL2 sensor on chip QU-11 versus exponential fits (“NTC fit” from eqn. 8-2, “NTCexpT fit” from eqn. 8-3).

Because the sensors’ behavior follows eqn. 8-3 quite well, the curve lends itself to normalization by shifting the first point to a value of (1,0) on a different scale. The most convenient way to do so is by rewriting the resistance and temperature in terms of the initial values.

$$\frac{R}{R_o} = e^{B(T-T_o)} \tag{eqn. 8-6}$$

Here, R_o and T_o are the resistance and temperature, respectively, of the first datum point. When each data series is recast in terms of the first point, as shown in Figure 8.3, the data fall on essentially the same curve. For the most accurate calibration, though, it is better to use the NTCexpT calibration for each sensor individually.

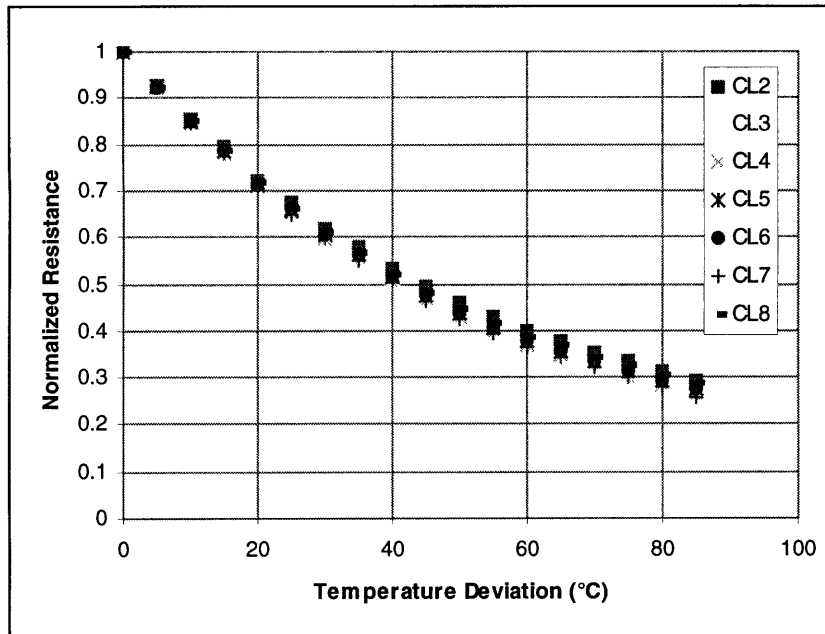


Figure 8.3 Normalized resistance versus temperature difference for CL array on QU-11 chip.

TEMPERATURE MEASUREMENT ISSUES

Our calibration curve relies on indirect measurement of sensor temperature. Rather than measuring the temperature directly off the chip’s surface, we measured from the package surface. This way, we avoided mechanically damage to the sensors during calibration. However, even when the chip and package were insulated from ambient conditions, they were not at the same temperature (conduction between chip and package creates a thermal gradient).

We discovered this problem while depositing octacosane drops on our chips. The drops began to solidify at an indicated temperature (from the package-mounted thermocouple) of 53°C; but the accepted melting point of octacosane is 61.4°C. When we sampled the temperature difference between the package and chip surfaces, we discovered that the difference between the two was not very significant – perhaps one or two degrees, at most. This confirmed that our controller’s thermocouple input was properly calibrated. However, by measuring the package surface, we did not take into account the temperature drop between the chip surface and the package. Therefore, to increase our temperature accuracy, we needed to simultaneously control the temperature of all the components in our system.

Thus, we placed the entire package holder in a laboratory oven and sampled the package and oven temperature at several points, to ensure spatial temperature homogeneity. The results for a single sensor (CL2) on one chip are shown in Figure 8.4. For reference, the temperature-resistance data obtained from using the package heaters alone are plotted on the same graph.

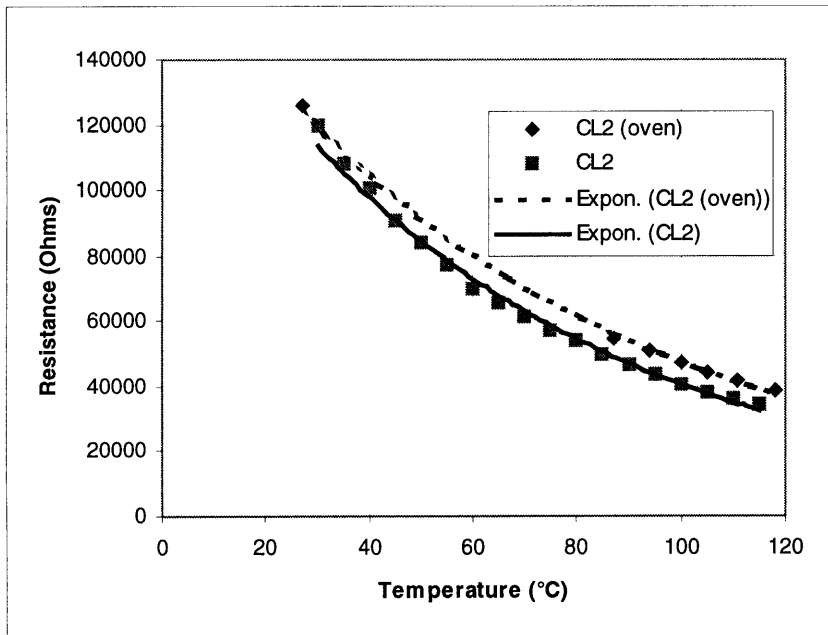


Figure 8.4 Resistance versus temperature for CL2 sensor on QU-11 chip, measured with package heaters only and oven heating.

Assuming that when the resistance of the oven-heated curve coincides with that of the package-heated, the oven-heated temperature is correct, we can correct the temperature measured on the surface of the package. Assuming that both the oven and package heated curves follow a NTCexpT thermistor curve, as defined in eqn. 8-3, then the package temperature in terms of the oven [actual] temperature is

$$T_i = \frac{B_a'}{B_i'} \cdot T_a + \frac{1}{B_i'} \cdot \ln\left(\frac{A_a'}{A_i'}\right) \quad \text{eqn. 8-7}$$

Here, the subscripts *a* and *i* refer to quantities for the actual (oven) and indicated (package) curves, respectively. In the illustrated case, fitting both the oven and package temperature data to eqn. 8-3 and plugging the curve-fitting values into eqn. 8-1 gives the behavior shown in Figure 8.2. Here, the actual temperature, namely the oven-heated temperature, is plotted against the temperature indicated from the package's surface. Although the data shown are from one sensor, the other sensors' behavior is essentially similar. In the ideal case, the indicated temperature would be the same as the actual temperature. Using eqn. 8-7, an indicated temperature of 55°C on the package surface corresponds to 61.6°C on the chip surface, which is slightly above the melting point of octacosane (61.4°C).

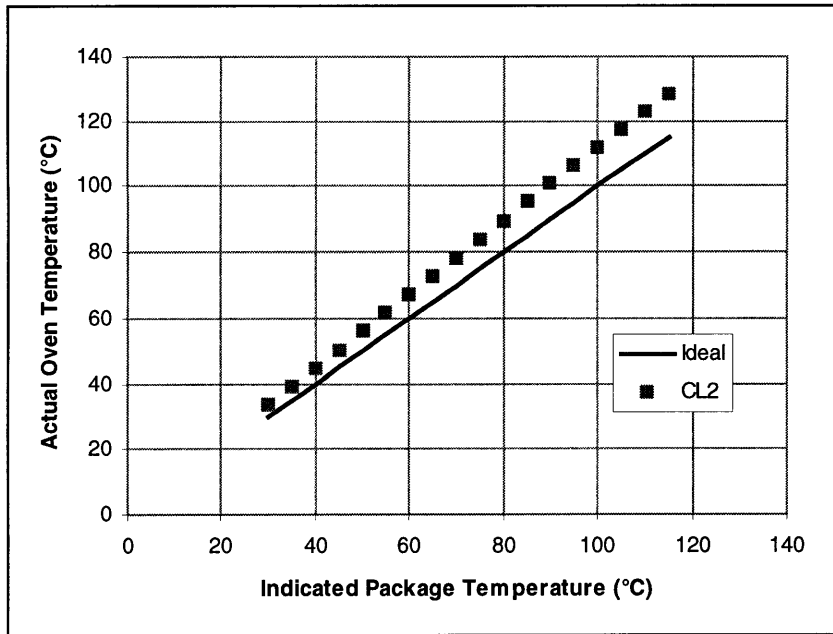


Figure 8.5 Actual (chip surface) temperature (in °C) versus indicated (package surface) temperature (in °C). CL2 sensor in QU-11 package.

Since the oven is slow to warm up and lacks low-power settings (the temperature at minimum heat is nearly 70°C), the package heaters are still more convenient to heat the chip for calibration. Using eqn. 8-7, we found a relation between indicated and actual temperatures. This way, we can set the temperature control in “My Calibration AI” to the usual sequence (30, 35, ..., 115°C), and set the indicated package temperature to a different sequence. Using the values obtained from one sensor with one sensor package, we obtain Table 8.1, which shows the relationship between the actual and indicated temperatures.

Actual (Chip) Temperature [°C]	Indicated (Heater Controller) Temp. [°C]
30	26
35	31
40	35
45	40
50	44
55	49
60	53
65	58
70	62
75	67

80	71
85	76
90	80
95	85
100	89
105	94
110	98
115	103

Table 8.1 Actual temperature versus indicated temperature for certain useful actual temperatures.

Although the relation given is specific to sensor CL2 of package QU-11, the sensors are consistent enough within a wafer that it can form a general guideline. The package should be well-insulated during the calibration.

CONCLUSIONS

Our microsensors' resistance depends exponentially on their temperature. Such behavior is characteristic of so-called NTCexpT thermistors. However, the temperature indicated from the package surface was lower than the actual chip surface temperature. For example, octacosane, with a melting point of 61°C, melted at an package-indicated temperature of 53°C. The entire apparatus was placed in a laboratory oven, and both package and chip reached a single temperature. Then the sensor resistances were sampled at different temperatures and fitted to a NTCexpT curve. This created a relation between the indicated and actual temperatures. Based on this relation, a new, more-accurate procedure for calibration was recommended.

Chapter 9 SENSOR RESPONSE IN DROP DEPOSITION

We finally measured the temperature history of several sensors while a contact line passed over them. While experimenting with the sensors, we discovered that our sensors acquired spurious temperature signals, probably caused by electromagnetic interference. Several sources of noise in our system were ferreted out and eliminated until the sensors returned useful data. Some sensor limitations were discovered when their performance was scrutinized.

NOISE ISSUES

Acquiring data with a chip at a temperature above the ambient revealed a problem with the heaters. They are powered by an alternating current (AC) temperature controller. To maintain the sensors at a steady temperature, the heaters are put through a duty cycle determined by the temperature controller. When the heaters cycle on, the sensors detect the 60 Hz AC voltage going through the heaters, as shown in Figure 9.1. The system also picks up some background noise at 60 Hz, shown in the temperature trace immediately before the heaters are turned on.

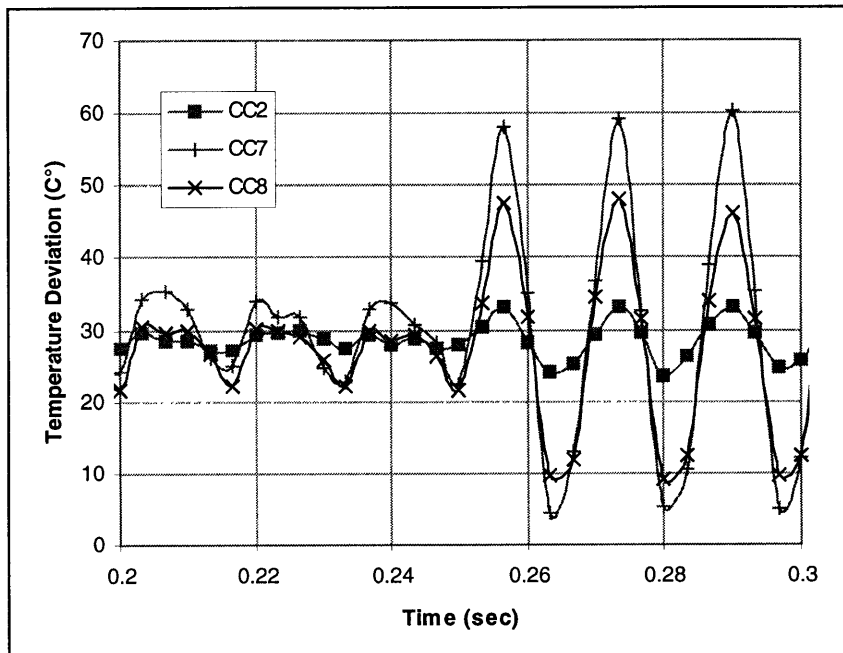


Figure 9.1 Indicated temperature (in °C, deviation from 30°C) versus time (in seconds) with unshielded heaters and cabling. CC array in QU-3 package; 300Hz sampling rate.

When the heaters and various unshielded cables in our system were wrapped in electrically-grounded aluminum foil, the measured temperature became virtually noise-free, as seen in Figure 9.2. The aluminum foil wrapping shields electromagnetic signals, acting as a Faraday cage.

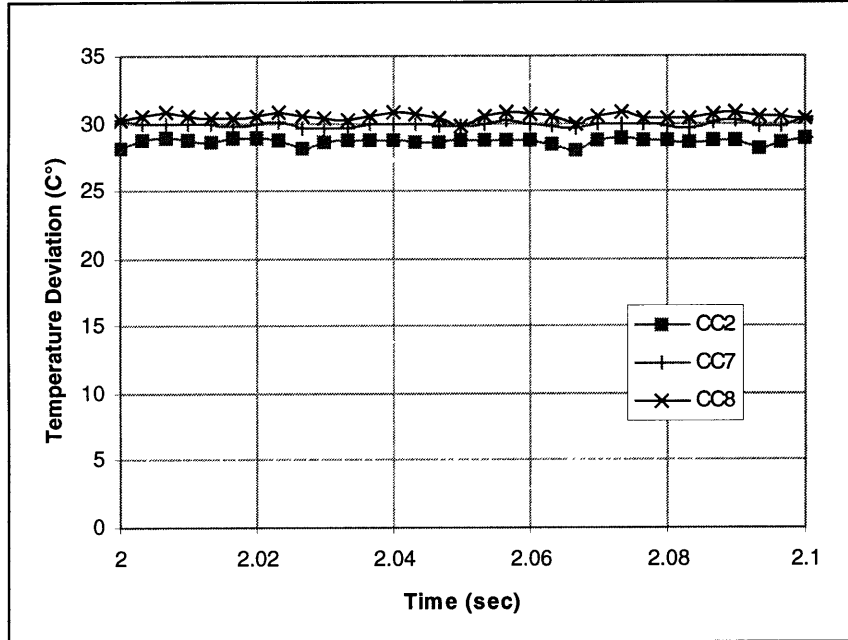


Figure 9.2 Indicated temperature (in °C, deviation from 30°C) versus time (in seconds) with shielded heaters and cabling. CC array in QU-3 package; 300Hz sampling rate.

Unfortunately, the piezoelectric element in the adapted thermal ink-jet print head also provided a significant source of noise. During a deposition experiment with this head, the only discernible signal was a burst of noise, illustrated in Figure 9.3. Since the length of the noise burst is the same as the total deposition time (N/f), the burst is probably a noise broadcast from the voltage pulses applied to the piezoelectric element in the print head. Although we could shield the print head with a Faraday cage, such a shield would be impractical. Because the front of the print head (facing the sensors) ejects the droplets, the shield can not cover the front.

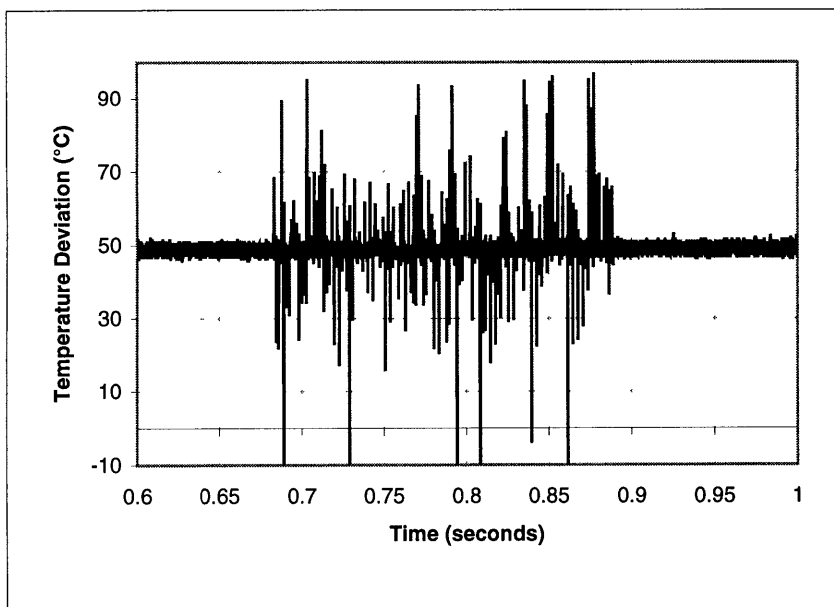


Figure 9.3 Indicated temperature (in °C, deviation from 30°C) versus time (in seconds), during a deposition experiment with the adapted thermal ink-jet print head. Microcrystalline wax (Reed 6882) on silicon dioxide; FL2 array in QU-3 package; 20kHz sampling rate.

Thus, we changed our deposition apparatus to the pendant drop dispenser built by Duthaler (1998). After another experiment, we discovered that our heater shielding was not completely effective. As illustrated in Figure 9.4, during deposition, the temperature appears to suddenly jump by 5°C and rapidly decay until it reaches its initial temperature approximately 2msec after the jump. By running several more temperature sampling experiments with different heaters connected to the controller, we discovered that the indicated “pulse” was more electromagnetic noise. This noise came from the initial surge of current going through the back heaters as their duty cycle began.

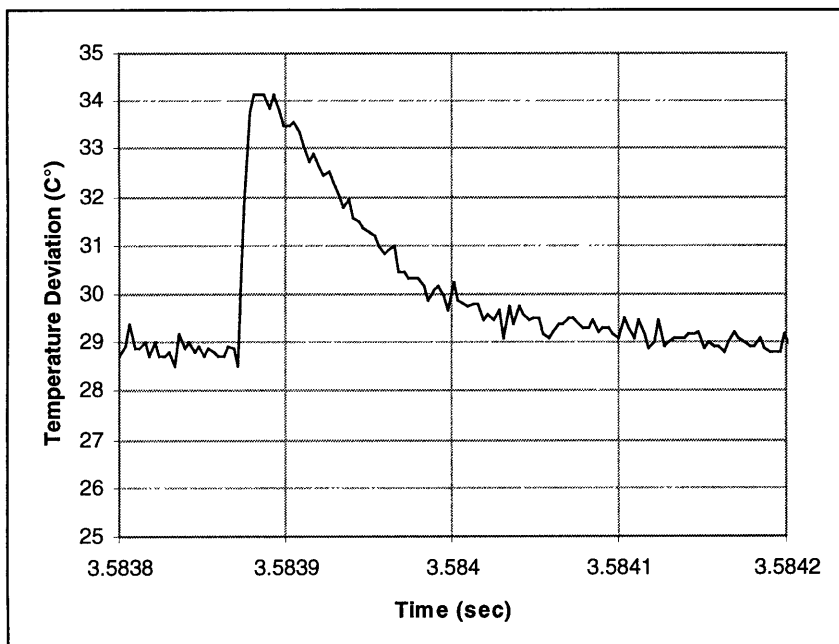


Figure 9.4 Indicated temperature (in °C, deviation from 30°C) versus time (in seconds), during a deposition experiment, showing spurious signal from back heaters. Octacosane on silicon dioxide; CL6 sensor in QU-7 package; 333kHz sampling rate.

Disconnecting the back heaters from the heater controller eliminated this noise source. However, without the back heaters, the maximum chip temperature is approximately 67°C (the back heaters allow for a chip temperature of up to ~ 157°C). Thus, we had to deposit molten octacosane, since it has a melting point of 61.4°C, and we wanted to experiment with small target subcooling. In any case, the material properties of octacosane, being a single-component material, are much better defined than the microcrystalline wax used previously (Reed 6882).

RESULTS

We acquired temperature data from sensors number 8, 6, and 3 in the coarse linear array (respectively: CL8, CL6, and CL3) of silicon dioxide chip number 11 (QU-11) at 111kHz per sensor. Based on the video acquired during the deposition, the melt appeared to spread over the eighth sensor before moving across the rest of the array, including the sixth and third sensors. The temperature history of these three sensors is shown in Figure 9.5. Since this experiment uses the NTCexpT calibration, the temperature is the actual value. The chip was held at an indicated value of 50°C; using the oven-derived correction, eqn. 8-7, we estimate the actual temperature to be 56°C. The pendant drop deposition nozzle's temperature fluctuated between 75 and 80°C. The droplet fell approximately 7mm from the tip of the nozzle to the surface of the chip.

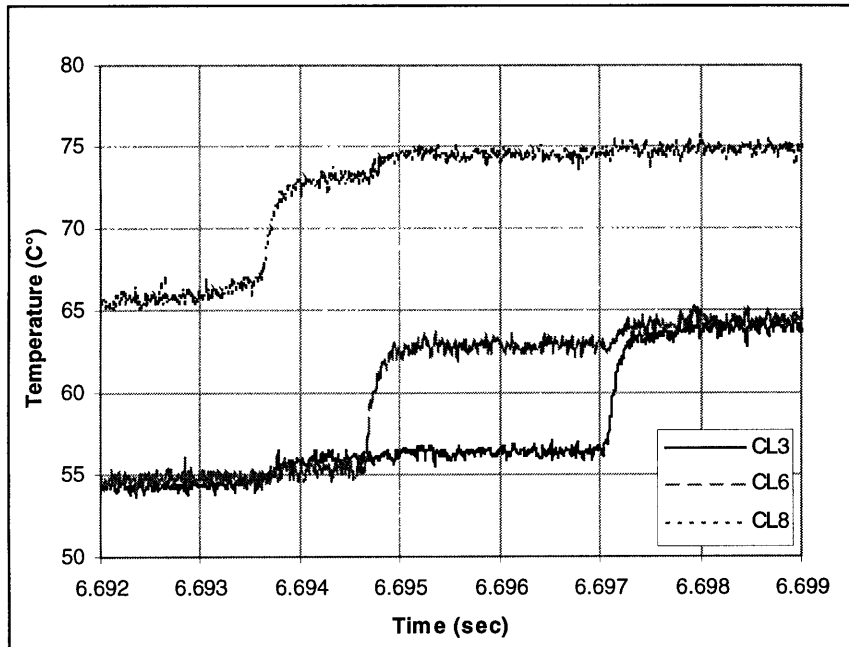


Figure 9.5 Temperature (in °C) versus time (in seconds) for three adjacent sensors. Octacosane on silicon dioxide; CL3, CL6, and CL8 sensors in QU-11 package; 111kHz sampling rate.

The temperature of CL8 lies ~ 10°C higher than the other two sensors, presumably due to miscalibration. Because the magnitude of CL8's temperature rise is the same as for CL6 and CL3, the data from CL8 appear to have some sort of DC offset.

Approximately 1.25msec separates the rise of sensors CL8 and CL6, which are spaced 400µm apart, while 2.5msec separates the rise of sensors CL6 and CL3, which are spaced 600µm apart. Thus, the speed of the contact line is approximately 0.32 m/s between CL8 and CL6; the speed slows to ~ 0.24 m/s between CL6 and CL3.

Note the cross-talk between sensors. The trace for CL8 shows a significant jump at approximately 6.69375 sec, with two minor jumps occurring at 6.695 and 6.6975 sec. Not coincidentally, these are the same times that CL6 and CL3, respectively, jump. In fact, each of the three sensors shows influence from the other two, rising ~ 2°C when another sensor was engulfed by the contact line. It is clearly not a thermal front propagating through the solid, as both CL8 and CL6 experience a small jump when the contact line engulfs CL3. Within a single array, each sensor shares a common lead; thus, the other sensors may feel the resistance changes of a single sensor.

The instantaneous rise in temperature is magnified for CL3 in Figure 9.6. The other sensors exhibit similar behavior. The actual rise occurs over approximately 0.25 msec, which is much longer than the spacing between samples (9 µsec), so we are confident that we captured the time scale accurately. Since a single coarse sensor has virtually no thermal inertia (defined as the product of mass and specific heat), this response is probably caused by heat transfer limitations from the melt to the sensor. Note that

because the silicon dioxide substrate has a characteristic thermal spreading time (defined in eqn. 5-3) of 4 msec, the rise takes place much faster than the thermal front propagates through the target. The DAQ board does not limit our system's temporal resolution. It has a maximum settling time (i.e. minimum time between successive samples) of 1 μ sec with an accuracy of $\pm 0.1\%$ per reading, according to the manufacturer's specifications.

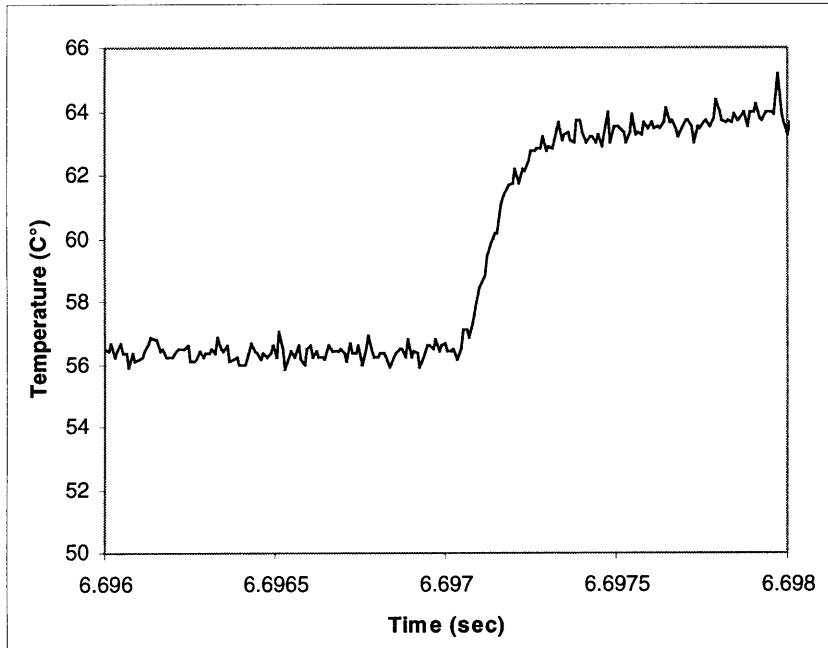


Figure 9.6 Temperature (in °C) versus time (in seconds) for one sensor, showing instantaneous rise as contact line passes. Octacosane on silicon dioxide; CL3 sensor in QU-11 package; 111kHz sampling rate.

When two semi-infinite solids are suddenly brought into contact, their interface will instantaneously assume a temperature compatible with the thermal properties of each material. By matching the heat fluxes across this interface, a simple expression may be obtained for this instantaneous interfacial temperature:

$$\frac{T_s - T_{1o}}{T_{2o} - T_s} = \sqrt{\frac{k_2 \cdot \rho_2 \cdot c_{p2}}{k_1 \cdot \rho_1 \cdot c_{p1}}} \quad \text{eqn. 9-1}$$

T_s is the interfacial temperature, while T_{1o} and T_{2o} are the initial (pre-contact) temperatures of materials 1 and 2, respectively. k_1 , ρ_1 , and c_{p1} are the thermal conductivity, density, and specific heat of material 1; material 2's properties are similarly labeled. The material properties for amorphous silicon dioxide and octacosane are substituted into eqn. 9-1, along with estimated initial material temperatures (56°C for the silicon dioxide target and 75-80°C for the octacosane melt). The expected interfacial temperature is

approximately 61°C, which translates into a jump of 5°C from the steady-state sensor temperature. In fact, we seem to measure a jump of ~ 8°C (discounting the effect of the cross-talk “jump”). Although this is the right order of magnitude, perhaps the semi-infinite assumption is not an adequate model for the two materials.

A more sophisticated model, similar to that presented in Chapter 7 (which takes into account different densities and released latent heat at one phase transition), yields essentially the same results. It can be shown that by (numerically) solving

$$\begin{aligned}
 & \frac{k_l}{k_t} \sqrt{\frac{\alpha_t}{\alpha_l}} \cdot \exp\left(\left[\lambda \frac{\rho_s}{\rho_l}\right]^2 - \left[\lambda \sqrt{\frac{\alpha_l}{\alpha_s}}\right]^2\right) \cdot \frac{T_{i0} - T_f}{\operatorname{erfc}\left[\lambda \frac{\rho_s}{\rho_l}\right]} \\
 & + \lambda L \rho_s \cdot \frac{\sqrt{\pi \rho_s \rho_l}}{k_t} \cdot \exp\left[\lambda \sqrt{\frac{\alpha_l}{\alpha_s}}\right]^2 \\
 & = \frac{T_f - T_{i0}}{\frac{k_t}{k_s} \sqrt{\frac{\alpha_s}{\alpha_t}} \cdot \operatorname{erf}\left(\lambda \sqrt{\frac{\alpha_l}{\alpha_s}}\right) + 1}
 \end{aligned} \tag{eqn. 9-2}$$

for λ , a proportionality constant, the temperature at the interface, T_s , is given by

$$T_s = \frac{T_f - T_{i0}}{\frac{k_t}{k_s} \sqrt{\frac{\alpha_s}{\alpha_t}} \cdot \operatorname{erf}\left(\lambda \sqrt{\frac{\alpha_l}{\alpha_s}}\right) + 1} + T_{i0} \tag{eqn. 9-3}$$

In the preceding equations, T_f is the fusion temperature, L is the latent heat released, and the other quantities are defined in Chapter 7.

Note that in the semi-infinite case, the temperature at the target-solidified melt interface remains independent of time. The decay of this interfacial temperature represents the breakdown of the semi-infinite model; in our case, the temperature of CL3 falls noticeably from 64°C to 62°C after 0.25 seconds. In comparison, the time scale for the thermal front to pass through the silicon dioxide substrate, l^2/α , is 4 msec.

CONCLUSIONS

After being processed and calibrated, the silicon-based microsensors were tested with spreading macrodrops. Testing revealed some unexpected sources of noise, including alternating current-powered

heaters, electrical equipment, and the adapted thermal ink-jet head. Once the sources of noise were removed or shielded, we proceeded to spread an octacosane drop across three sensors. The acquired data reveal the speed of the contact line, as well as the temperature history when the contact line passes over a sensor. The transient temperature rise is limited by the heat transfer between the molten octacosane and the sensor. The eventual magnitude of the temperature rise was modeled by two semi-infinite solids brought into sudden contact. This model predicted the temperature rise at the interface with reasonable accuracy.

Chapter 10 CONCLUSIONS AND FURTHER WORK

A complete system for acquiring data from micron-scale temperature sensors has been presented. We discussed the construction of these sensors has been discussed and the reasoning behind their design. The spreading of a molten material (a microcrystalline wax, Reed 6882) on a target of a different kind (monocrystalline silicon) was characterized through several preliminary tests. Various pieces of supporting hardware and software have been designed, built, and discussed. Finally, the sensors are characterized through their resistance change with temperature, which was used later during an actual molten droplet deposition test.

Clearly, these thin-film thermistors are vulnerable to electromagnetic interference. Although the entire system is sensitive to noise, the sensors are the most sensitive part, picking up AC line signals. According to Wolfenbuttel, et al (1996), silicon is also a photoelectric material. We did not test for this phenomenon, however. Some of our calibration tests were conducted in the oven, while other deposition experiments illuminated the chip for the CCD camera. The photoelectric effect could have added DC offsets to our signals from each sensor on the chip, which in turn would be translated into a higher temperatures by our software.

These sensors make liquid sample diagnostics possible. From eqn. 9-1, we can estimate a melt's thermal properties if we know the substrate properties, the temperatures involved, and two of the three melt thermal properties (i.e. two of k_l , ρ_l , c_{pl}). Since density and specific heat can be measured with simple tests, we can quickly estimate the thermal conductivity with these sensors. However, more accurate models and/or calibrations would be needed to back out more than an order-of-magnitude estimate of the thermal property.

The temporal resolution was quite good. In an earlier deposition test, not discussed here, we were able to sample a single coarse sensor at 3 μ sec intervals, or a frequency of 333 kHz. For reference, digital information streams from a compact disk audio system at a frequency of 44 kHz. The thermistors' small size and mass are directly responsible for this performance. In fact, the temporal resolution was more than we needed – since our temperature rise time was on the order of 10^2 μ sec, we could probably sample at a minimum of 10 kHz and retain much of the same information.

The sensors still cannot resolve molecular-scale heat transfer phenomena. They are approximately an order of magnitude larger than lower limit of the thermal cut-off length estimated by Schiaffino (1996), so it is most likely not possible to examine the heat transfer in the near-contact line region. However, they do offer the most spatially detailed investigation of the contact line currently possible. As of this writing, only the most advanced microprocessors on the market use a sub-micron feature size, so sub-micron thermistors are not feasible in the short term.

Trying to predict the spreading behavior of wax on silicon was inconclusive. In general, macrodrop contact angles increase with decreasing target temperatures, decreasing droplet frequency, or increasing the number of droplets. However, we discovered that surface features had the greatest effect on spreading. In addition, the target's thermal conductivity seemed to have little effect on the post-solidification equilibrium contact angle.

FURTHER WORK

It may be possible to further reduce the noise in the system. Increasing the excitation voltage in the system allows the data acquisition board to amplify the input signals less, so spurious signals will be of smaller magnitude than valid readings. The cross-talk between signals is difficult to eliminate without significant rewiring of our system. Although our cabling is shielded overall, the signal lines are not individually shielded. In addition, the internal circuit wiring may also contribute to the noise. Any possible photoelectric effect should also be investigated, although Kiewra and Wayner (1989) state that their silicon carbide thermistors do not exhibit any such effects.

The chips, as designed, are somewhat difficult to package. As stated in Chapter 2, the uneven number of pads make it difficult to connect all of the sensors in a standard 40-pin dual in-line chip package (DIP). Either using a different style of package (preferably one with at least 22 pads on one side of the well) or redesigning the layout of the chip would be helpful. Since a number of uncut wafers using the same chip style are currently stored at the MTL, it would probably be easier to change the package style. In addition, changing the chip layout requires making new photolithography masks, which is an expensive and time-consuming process.

A mathematical model of heat flux close to the contact line is needed first. With such a model, we could determine the heat flux from the indicated temperature distribution.

The sensors can be used to perform the liquid diagnostics mentioned above. Liquids with known properties should be used first, to characterize the sensors further. Other molten materials, such as microcrystalline wax, may be deposited on the chip both to confirm the octacosane results and to confirm the wax's thermal properties. However, the heaters on the package holder must be upgraded so that they can heat the chip closer to the melting point of wax, 91°C.

Although the concept of thermal microsensors is not new, the ones described in this thesis are unusually flexible because of their size and speed. Because of their cost and time involved in construction, though, they are not likely to replace conventional temperature sensors, such as thermocouples, for general measurements. Thus, these sensors are best suited for extremely high-resolution measurements or when their construction – a small sensor on a relatively massive substrate – proves useful, such as in liquid diagnostics.

NOMENCLATURE AND ABBREVIATIONS

$1RFR_1$	resistance of the first fixed resistor in the reference divider circuit of the fine linear array circuit box (literally, “number 1 Reference Fixed Resistor 1”); for the coarse array circuit box, see entry below for $yRFR_1$
$2RFR_1$	resistance of the second fixed resistor in the reference divider circuit of the fine linear array circuit box (literally, “number 2 Reference Fixed Resistor 1”)
A	constant of integration or coefficient used in NTC calibration
A'	coefficient used in NTCexpT calibration
A_a'	coefficient of NTCexpT calibration, using actual chip temperature
A_i'	coefficient of NTCexpT calibration, using indicated package temperature
B	argument coefficient used in NTC calibration
B'	argument coefficient used in NTCexpT calibration
B_a'	argument coefficient of NTCexpT calibration, using actual chip temperature
B_i'	argument coefficient of NTCexpT calibration, using indicated package temperature
C	constant of integration
$C1$	Capacitor 1
c_1	specific heat of semi-infinite body number 1
c_2	specific heat of semi-infinite body number 2
c_e	enhanced specific heat for mushy material
c_l	specific heat of liquid (melt) material
c_m	specific heat of mushy (from melt) material
c_s	specific heat of solidified (from melt) material
c_t	specific heat of target material
D	constant of integration
DV	Divider Voltage, when using fine linear array circuit box or Differential Voltage, when using coarse array (either) circuit box
E	constant of integration
EV	Excitation Voltage applied across the circuit
F	constant of integration
f	microdrop deposition frequency to form a macrodrop
G	constant of integration
k_1	thermal conductivity of semi-infinite body number 1
k_2	thermal conductivity of semi-infinite body number 2
k_l	thermal conductivity of liquid (melt) material
k_m	thermal conductivity of mushy (from melt) material
k_s	thermal conductivity of solidified (from melt) material
k_t	thermal conductivity of target material
L	latent heat of fusion
l	characteristic length (generally, wafer thickness = 0.6mm)
N	total number of microdrops deposited in a single macrodrop
N^*	threshold value of number of microdrops, relating to post-solidification contact angle
R	thermistor resistance
R_c	radius of curvature of a macrodrop
R_{NTC}	resistance of a thermistor exponentially dependent on the inverse of temperature
R_o	resistance of the first datum point on a calibration curve (i.e. at lowest temperature)
r_b	contact radius of a solidified macrodrop
S	Stefan number [$c_p(T_f - T_i)/L$]
S_1	constant depending on material properties and λ_1, λ_2
S_2	constant depending on material properties and λ_1, λ_2
S_3	constant depending on material properties and λ_1, λ_2

S_4	constant depending on material properties and λ_1, λ_2
$SRCx_y$	resistance of coarse sensor array (either linear or cross) sensor number y (literally, “Sensor Resistance Coarse x Array sensor number y ”)
$SRFL_y$	resistance of fine linear sensor array sensor number y (literally, “Sensor Resistance Fine Linear Array sensor number y ”)
T	temperature
T_{1o}	initial temperature of semi-infinite body number 1
T_{2o}	initial temperature of semi-infinite body number 2
T_a	actual chip temperature
T_{f1}	lower temperature of phase transition zone (solid-mushy transition temperature)
T_{f2}	higher temperature of phase transition zone (mushy-liquid transition temperature)
T_i	indicated package temperature
T_{lo}	initial liquid (melt) temperature
T_o	temperature at the first datum point on a calibration curve (i.e. at lowest temperature)
T_s	interfacial temperature
T_t	target temperature
T_{to}	initial target temperature
t	time
t_{char}	characteristic diffusion time
t_d	total deposition time
u_{x1}	density-change-induced velocity imparted to lower phase transition front (solid-mushy)
u_{x2}	density-change-induced velocity imparted to higher phase transition front (mushy-liquid)
X_1	position of lower phase transition front (solid-mushy)
X_2	position of higher phase transition front (mushy-liquid)
$yDFR_1$	resistance of the fixed resistor in divider circuit number y of the fine linear array circuit box (literally, “number y Divider Fixed Resistor 1”)
$yLFR_1$	resistance of the first fixed resistor in the left half of sensor circuit number y of the coarse array circuit box (literally, “number y Left Fixed Resistor 1”)
$yLFR_2$	resistance of the second fixed resistor in the left half of sensor circuit number y of the coarse array circuit box (literally, “number y Left Fixed Resistor 2”)
$yRFR_1$	resistance of the fixed resistor in the right half of sensor circuit number y of the coarse array circuit box (literally, “number y Right Fixed Resistor 1”) – there exist exceptions for “1RFR ₁ ” and “2RFR ₁ ”, listed above)

GREEK SYMBOLS

α_l	thermal diffusivity of liquid (melt) material
α_m	thermal diffusivity of mushy (from melt) material
α_s	thermal diffusivity of solidified (from melt) material
α_t	thermal diffusivity of target material
γ_{NTC}	temperature coefficient of resistance of a thermistor exponentially dependent on the inverse of temperature
$\gamma_{NTCexpT}$	temperature coefficient of resistance of a thermistor exponentially dependent on the temperature
γ_{rt}	temperature coefficient of resistance
δ_w	wafer thickness
η_l	similarity variable for liquid (melt) material
η_m	similarity variable for mushy (from melt) material
η_s	similarity variable for solidified (from melt) material
η_t	similarity variable for target material
λ_1	proportionality constant related to lower phase transition front position (solid-mushy)
λ_2	proportionality constant related to higher phase transition front position (mushy-liquid)
θ	apparent contact angle
θ_∞	apparent non-equilibrium post-solidification contact angle

θ_s	apparent constant non-equilibrium post-solidification contact angle
ρ_l	density of liquid (melt) material
ρ_m	density of mushy (from melt) material
ρ_s	density of solidified (from melt) material
ρ_t	density of target material

ABBREVIATIONS

AC	Alternating Current
ACHy	Analog Input Channel number y
AIGND	Analog Input Ground
AISENSE	Analog Input Sense (reference voltage for single-ended input mode)
AMC	Auto/Manual Channel (selector in MCAF)
ASli	Array Slicer LabVIEW program, for data reduction
ASub	Array Subsetter LabVIEW program, for data reduction
CC	Coarse Cross sensor array
CCy	Coarse Cross sensor number y
CL	Coarse Linear sensor array
CLy	Coarse Linear sensor number y
COM	Common line
Cx	Coarse sensor array (either cross or linear)
Cxy	Coarse sensor array (either) sensor number y
DAQ	Data Acquisition
DIP	Dual In-Line Package for a silicon chip
DVy	fine linear sensor array circuit tap number y (literally, “Divider Voltage tap number y”)
EV	Excitation Voltage (control in MCAF, MCAI, and MDAF)
FL	Fine Linear sensor array
FLy	Fine Linear sensor number y
GROUND	Electrical Ground
GSA	Grab Save Analyze (cal) LabVIEW program, for calibration
IC	Integrated Circuit
ISA	Industry Standard Architecture personal computer expansion bus
LVy	coarse sensor array (either) circuit’s left-half tap number y (literally, “Left Voltage tap number y”)
MCAF	My Cont Acq to File (binary) LabVIEW program, for continuous sensing
MCAI	My Calibration AI LabVIEW program, for calibration
MDAF	My Disp Acq’d File (binary) LabVIEW program, for continuous sensing
MTL	Microsystems Technology Laboratory, building 39
N/C	Not Connected
NTC	Negative Temperature Coefficient (exponential dependence on inverse temperature)
NTCexpT	Negative Temperature Coefficient with exponential dependence on Temperature
n-doped	negative-ion-doped semiconductor (phosphorous-doped)
p-doped	positive-ion-doped semiconductor (boron-doped)
poly-Si	polycrystalline silicon
RTD	Resistance Temperature Detector
RV	fine linear array reference circuit’s tap (literally, “Reference Voltage tap”)
RVy	coarse sensor array (either) circuit’s right-half tap number y (literally, “Right Voltage tap number y”)
SAP	Sliced Array Plotter LabVIEW program, for data display
SCxPy	Coarse Array (either) Sensor Pin number y
SFLPy	Fine Linear Array Sensor Pin number y
TCR	Temperature Coefficient of Resistance, characteristic of thermistors

REFERENCES

- Baltes, H. 1993. "Microsensors between Physics and Technology". *Physica Scripta T*. **T49B**. pp. 449-453.
- Bordoni, F. and D'Amico, A. 1990. "Noise in Sensors". *Sens Actuators A*. **21-23**. pp. 17-24.
- Carslaw, H.S. and Jaeger, J.C. 1959. *Conduction of Heat in Solids*. Oxford. New York.
- Duthaler, G.M. 1998. *Molten Drop Deposition and the Dynamics of the Molten Contact Line*. Ph.D. Thesis. Department of Mechanical Engineering, MIT. Cambridge, MA.
- Gao, F. 1994. *Molten Microdrop Deposition and Solidification Processes*. Ph.D. Thesis. Department of Mechanical Engineering, MIT. Cambridge, MA.
- Gao, F. and Sonin, A.A. 1994. "Precise Deposition of Molten Microdrops: the Physics of Digital Microfabrication". *Proc Roy Soc London A*. **444**. 533-554.
- van Herwaarden, A.W. and Sarro, P.M. 1986. "Thermal Sensors Based on the Seebeck Effect". *Sens Actuators*. **10**. pp. 321-346.
- Incropera, F.P. and DeWitt, D.P. 1990. *Fundamentals of Heat and Mass Transfer*. Wiley. New York.
- Kiewra, E.W. and Wayner, P.C. 1989. "The Development of a Thin-Film Silicon Carbide Thermistor Array for Determining Temperature Profiles in an Evaporating Liquid Film". *J Electrochem Soc*. **136**. pp. 740-744.
- Korites, B.J. 1986. *Microsensors*. Kern International. Rockland, MA.
- Kuźma, E. 1994. "Thermistors with Exponential Resistance-Temperature Dependence". *Electron Technology (Warsaw)*. **26**. pp. 75-79.
- J. Lipton, A. Garcia, and W. Heinemann. 1982. "An Analytical Solution of Directional Solidification with Mushy Zone". *Archiv für das Eisenhüttenwesen*. **53**. pp. 469-473.
- Qiu, T.Q. 1996. *Development of Microsensors for High-Resolution Characterization of Contact-Line Dynamics*. Internal MIT document.
- Sachse, H. 1975. *Semiconducting Temperature Sensors and their Applications*. Wiley. New York.
- Schiaffino, S. 1996. *The Fundamentals of Molten Microdrop Deposition and Solidification*. Ph.D. Thesis. Department of Mechanical Engineering, MIT. Cambridge, MA.
- Schiaffino, S. and Sonin, A.A. 1997a. "Formation and Stability of Liquid and Molten Bead on a Solid Surface". *J. Fluid Mech*. **343**. pp. 95-110.
- Schiaffino, S. and Sonin, A.A. 1997b. "Motion and Arrest of Molten Contact Line on a Cold Surface: an Experimental Study". *Phys. Fluids*. **9**. pp. 2217-2226.
- Schiaffino, S. and Sonin, A.A. 1997c. "On the Theory for the Arrest of an Advancing Molten Contact Line on a Cold Solid of the Same Material". *Phys. Fluids*. **9**. pp. 2227-2233.

- Schiaffino, S. and Sonin, A.A. 1997d. "Molten Droplet Deposition and Solidification at Low Weber Numbers". *Phys Fluids*. **9**. pp. 3172-3187.
- Schwarz, S.E. and Oldham, W.G. 1993. *Electrical Engineering: an Introduction*. Saunders. Fort Worth, TX.
- Torresola, J. 1998. *Solidification Properties of Certain Waxes and Paraffins*. S.M. Thesis. Department of Mechanical Engineering, MIT. Cambridge, MA.
- R.F. Wolffenbuttel (ed.) with J. Bryzek, P.J. French, H. Kaneko, T. Kita, T. Mihara, K. Najafi, G. Smith, and M.J. Vellekoop. 1996. *Silicon Sensors and Circuits: On-chip Compatibility*. Chapman & Hall. London.

APPENDIX A: THE MTL AND ITS MACHINES

The Microsystems Technology Laboratory (MTL, building 39) is an on-campus facility dedicated to the microfabrication of both electronic and mechanical devices. Its technical staff and faculty train people who wish to use the specialized silicon wafer and chip processing equipment. We use the packaging equipment, rather than the wafer fabrication equipment. Regardless of the equipment used, to become a member/user of the MTL, one must: undergo safety training, obtain a lab account, and receive specific machine training.

Generally, the safety training is a one-day presentation held towards the beginning of the semester; contact Celia Mokalled (celiam@mtl.mit.edu, x3-8186, room 39-221), on the second floor, to determine the specific time. Alternatively, the same material is available in printed form for individual study. After learning the specific safety instructions for the MTL, one takes a short written test; passing this test allows one to obtain a user account at the MTL.

The user account tracks machine usage at the MTL. The standard fee is ten dollars per month; equipment use costs are calculated on a usage-time basis. Machine usage is tracked through a voluntary machine log. The swipe card is included in the ten-dollar monthly fee; it allows the central computer to track which room you have entered. The voluntary log is accessed through a custom program (Computer Aided Fabrication Environment, CAFE). MTL users must first reserve a machine for use through CAFE before going to the MTL to use it. They also need to create lots and wafersets before operating the machine. Complete information on CAFE is presented in the safety training session. All proposals for accounts must be submitted in writing and approved by the director of the MTL, Dr. Vicky Diadiuk (diadiuk@mtl.mit.edu, x3-0731, room 39-219).

Finally, the user must be trained to use a specific machine before he/she is allowed to operate it. During machine training, the regular operator and trainee run a sample together through the machine. The regular operator demonstrates and explains the instructions, and the trainee is expected to demonstrate a basic grasp of the operation. All of the packaging machines' training is handled by Dan Adams (dan@mtl.mit.edu, x3-6239, room 39-204A), Kurt Broderick (kurt@mtl.mit.edu, x3-5241, room 39-204A), or Joe Walsh (walsh@mtl.mit.edu, x3-6897, room 39-215).

PACKAGING EQUIPMENT USAGE

The first machine used in packaging chips is the diesaw. The diesaw separates each wafer into individual chips; it combines a high-speed circular aluminum blade with precise positioning to cut with micron-scale location accuracy. A split-image microscope is used to line up wafer features, which ensures that cuts track straight across a wafer. Separate images are taken approximately two inches apart on the wafer; these images form the left and right halves of the microscope's field-of-view. The cut is aligned

when the two images line up. A vacuum system holds the wafer tightly to the platen as it is passed under the blade. While cutting, two water jets, with adjustable flowrate, cool the blade.

The diesaw startup/shutdown procedure and operation are best explained by the training operator. However, several guidelines may be useful for our particular wafers. First, completed sensor wafers are available through Bernard Alamariu (bernard@mtl.mit.edu, x3-8811, room 39-213). Be sure to specify which substrate material is needed; plain silicon wafers are opaque and tinted dark purple, while quartz wafers are translucent orange. Because each wafer requires a large number of cuts (thirty-two), getting air bubbles out is imperative. When applying the blue flashbreaker tape to the wafer's back, try to minimize the amount air trapped between the wafer and tape. To get rid of these air pockets, turn the wafer face down on a soft cloth and, with a fingernail, gently work the bubble out towards the edge of the wafer. If these bubbles remain, the cooling water jets will force the chip off the tape when the blade passes over them. For silicon wafers, the water jets can be set to a low flow rate; however, quartz wafers are harder and correspondingly require more cooling water. Because the blade is so thin, it breaks easily; when it does, ask Joe Walsh to fix it – do not attempt to repair it.

Next, individual chips are glued into packages with a conductive epoxy. Chips may be separated from the tape by gently prying them off with a blunt pair of tweezers. One should remove the small bits of extra wafer as needed to avoid chipping the chip edges. The epoxy is available from Joe Walsh, and consists of two separate silver-colored pastes: the resin and the hardener. After mixing an equal amount of both, put a tiny amount on the back of the chip and seat the chip in the package well. This epoxy cures after fifteen minutes at 150°C. If too much epoxy is placed on the chip, it will spread (possibly over the chip and/or package well pads) during the curing process. Small cotton swabs are excellent for mixing and applying the epoxy (using the wooden end), as well as seating the chip properly in the well (using the cotton end). To apply the correct amount of epoxy, hold the chip with tweezers and touch it to the end of the mixing stick.

The gold-ball wirebonder connects the chip pads with the package leads via ten-micron diameter gold wires. It has a stereo microscope for depth perception and a puck-controlled stage for precise movement of the part. The bonding programs can be tailored to individual chips and packages.

Again, the general procedure of using the wirebonder is best explained by the training operator. The wirebonder is a very finicky machine; its precision parts are delicate. The nozzle tip clogs quite easily; again, ask Joseph Walsh to fix it. Occasionally, the paddle that severs the wire following the second bond will be tweaked out of shape; gently adjust it back so that its middle strikes through the wire. Sometimes the wire will come out of the nozzle. Release the clamp, feed the wire back into the nozzle with tweezers, pull the loose end through the tip of the nozzle, and snap off about six inches of wire, leaving a small amount hanging through the nozzle. Then use the electronic flame-off to sever the end, engage the clamp, and reset the bonding program, if necessary.

Always bond from the chip to the package. It is easier to bond in one direction (e.g. bottom to top) and rotate the package as needed than to bond in four different directions – one can consistently judge

direction and distance. Perhaps half the time, no matter how well the practice bonding goes, bonds will not adhere to the real chip and package. First, try blowing dust off the part (there is a small compressed air nozzle near the diesaw power switch). Adjusting the program settings (time, force, search, etc.) may or may not help; on different days, the same settings will result in varied bond success. Perhaps the ambient humidity oxidizes the contacts too much for adequate bonding. The zoom setting on the stereo microscope is a personal judgement, but it is useful to be able to see the entire array at once while bonding, in order to determine which pads have already been connected. It is a good idea to reserve enough time on the bonding machine to finish bonding all of the wires on all of the packages in one session.

APPENDIX B: MATERIAL PROPERTIES

	Thermal Conductivity	Density	Specific Heat	Thermal Diffusivity
	(k)	(ρ)	(c_p)	(α)
	[W/m K]	[kg/m ³]	[J/kg K]	[m ² /s]
plain silicon (Si) [1]	148	2 330	712	8.92e-5
fused silica (amorphous SiO₂) [1]	1.38	2 220	745	8.34e-7
microcrystalline wax (Reed 6882) [2]	0.073	780 (l)	2900 (l)	3.23e-8 (l)
		930 (s)	2000 (s)	3.93e-8 (s)
octacosane (C₂₈H₅₈) [3]	0.15	774 (l)	2378	8.15e-8 (l)
		804 (s)		7.85e-8 (s)

	Melting Point	Solid Trans. Pt.	Latent Heat of Fusion	Heat of Trans. Pt.
	[°C]	[°C]	[kJ/kg]	[kJ/kg]
microcrystalline wax (Reed 6882) [3]	90	n/a	190 (from 30 to 90°C)	n/a
octacosane (C₂₈H₅₈) [3]	61.4	58.1	163.6 (@61.4°C)	89.8 (@58.1°C)

Sources:

[1] Incropera (1990)

[2] Torresola (1997)

[3] Torresola (1998)

APPENDIX C: DATA FOR SELECTED FIGURES

T_t (°C)	S (Stefan #)	f (Hz)	N (#)	θ_∞ (deg)
74	0.244211	1000	125	105.0318
76	0.213684	1000	125	106.2877
78	0.183158	1000	125	101.228
80	0.152632	1000	125	92.20116
82	0.122105	1000	125	N/A
84	0.091579	1000	125	74.22739
86	0.061053	1000	125	45.71659
88	0.030526	1000	125	21.58156
90	0	1000	125	17.97495
92	-0.03053	1000	125	14.98809
94	-0.06105	1000	125	16.20144
74	0.244211	10000	125	56.28948
76	0.213684	10000	125	53.21152
78	0.183158	10000	125	45.71659
80	0.152632	10000	125	39.63084
82	0.122105	10000	125	39.2564
84	0.091579	10000	125	N/A
86	0.061053	10000	125	30.77392
88	0.030526	10000	125	26.14292
90	0	10000	125	19.19095
92	-0.03053	10000	125	15.22111
94	-0.06105	10000	125	15.22111
74	0.244211	5000	125	71.13991
76	0.213684	5000	125	60.05793
78	0.183158	5000	125	50.75694
80	0.152632	5000	125	N/A
82	0.122105	5000	125	34.72442
84	0.091579	5000	125	31.34641
86	0.061053	5000	125	26.85334
88	0.030526	5000	125	21.58156
90	0	5000	125	17.97495
92	-0.03053	5000	125	12.79966
94	-0.06105	5000	125	13.47992

Table C.1 Data from Figure 5.2 (a).

T _t (°C)	S (Stefan #)	f (Hz)	N (#)	θ _∞ (deg)
78	0.183158	5000	2	39.30929
78	0.183158	5000	4	33.56489
78	0.183158	5000	8	38.33703
78	0.183158	5000	16	32.02467
78	0.183158	5000	25	33.36395
78	0.183158	5000	50	34.07599
78	0.183158	5000	100	39.11453
78	0.183158	5000	250	62.49159
78	0.183158	5000	500	N/A
82	0.122105	5000	2	33.84803
82	0.122105	5000	4	25.91576
82	0.122105	5000	8	7.923439
82	0.122105	5000	16	21.70356
82	0.122105	5000	25	29.87073
82	0.122105	5000	50	28.95497
82	0.122105	5000	100	32.92625
82	0.122105	5000	250	37.01573
82	0.122105	5000	500	50.67778
86	0.061053	5000	2	16.9768
86	0.061053	5000	4	16.11541
86	0.061053	5000	8	21.76636
86	0.061053	5000	16	20.6361
86	0.061053	5000	25	22.05751
86	0.061053	5000	50	24.14194
86	0.061053	5000	100	24.80411
86	0.061053	5000	250	25.34725
86	0.061053	5000	500	30.57316
90	0	5000	2	17.52551
90	0	5000	4	16.5209
90	0	5000	8	14.81636
90	0	5000	16	14.76413
90	0	5000	25	14.75575
90	0	5000	50	16.43828
90	0	5000	100	18.02808
90	0	5000	250	20.77456
90	0	5000	500	20.28604

Table C.2 Data from Figure 5.2 (b).

S (Stefan #)	θ_s (deg)
0	17
0.061	22
0.122	28
0.183	35

Table C.3 Data from Figure 5.3.

T_1 (°C)	f (Hz)	N (#)	t_d (sec)	θ_s (deg)
78	500	125	0.25	100.5893
78	1000	125	0.125	79.27459
78	2500	125	0.05	67.51939
78	5000	125	0.025	35.05158
78	10000	125	0.0125	42.36005
78	15000	125	0.008333	38.88574
78	20000	125	0.00625	44.85326
78	25000	125	0.005	33.4499
78	5000	2	0.0004	39.30929
78	5000	4	0.0008	33.56489
78	5000	8	0.0016	38.33703
78	5000	16	0.0032	32.02467
78	5000	25	0.005	33.36395
78	5000	50	0.01	34.07599
78	5000	100	0.02	39.11453
78	5000	250	0.05	62.49159
78	5000	500	0.1	N/A

Table C.4 Data from Figure 5.4.

Ind. Temp (°C)	CL1 (ohms)	CL2 (ohms)	CL3 (ohms)	CL4 (ohms)	CL5 (ohms)	CL6 (ohms)	CL7 (ohms)	CL8 (ohms)
30	16367721	119911.09	124439.85	123864.57	118517.54	115903.31	121755.01	131235.53
35	11466460	107975.63	111475.28	110795.2	106223.51	103902.45	108828.45	117891.53
40	17787886	100763.85	103366.41	102757.07	98675.633	96724.742	101065.06	109488.91
45	12444323	91140.25	92977.992	92314.258	89003.188	87124.867	90709.742	98843.875
50	14837545	84186.688	85417.844	84849.133	81775.258	80240.813	83167.328	90935.063
55	16793988	77320.57	77981.414	77405.586	74735.547	73417.422	75826.625	83294.852
60	17900860	70116.078	69981.031	69502.141	67338.234	66184.203	68020.766	75252.375
65	17402518	65725.25	65473.902	64971.195	62983.856	61917.293	63556.5	70556.063
70	25225604	61636.145	61050.879	60546.617	58851.09	57851.563	59197	66036.828
75	77680976	57205.82	56213.371	55705.512	54283.691	53364.859	54412.453	61064.559
80	114165272	53771.375	52575.867	52001.434	50771.141	50047.063	50795.688	57271.152
85	-15232644	49591.961	48087.66	47588.555	46598.867	45970.398	46418.297	52799.016
90	46048792	46639.309	44995.383	44523.242	43662.793	43082.598	43372.289	49687.547
95	31058520	43306.617	41527.656	41056.258	40378.52	39860.066	39967.309	46157.813
100	168761488	40634.336	38807.426	38339.254	37787.93	37298.375	37310.918	43304.922
105	33824752	37828.621	35905.559	35515.961	35068.633	34605.965	34473.129	40502.602
110	84200864	36266.445	34183.438	33742.195	33404.285	33027.211	32747.619	38738.731
115	111622240	34265.539	32171.408	31734.125	31504.529	31145.809	30773.703	36717.664
A'	NaN	176513.08	189982.13	189597.63	178970.02	174400.41	187502.44	193454.81
B'	NaN	-0.0147	-0.0159	-0.016	-0.0156	-0.0154	-0.0162	-0.015

Table C.5 Data from Figure 8.1, with NTCexpT fit coefficients.

Ind Temp (°C)	CL2 Oven Temp (°C)
30	33.5928899
35	39.1865596
40	44.7802293
45	50.373899
50	55.9675687
55	61.5612384
60	67.1549081
65	72.7485778
70	78.3422475
75	83.9359172
80	89.5295869
85	95.1232566
90	100.7169263
95	106.310596
100	111.9042657
105	117.4979354
110	123.0916051
115	128.6852748

Table C.6 Data from Figure 8.5.